Development of Graphite Based Nanomaterials for Green Chemistry Applications

A Thesis Presented to

The Faculty of Graduate Studies, Department of Chemistry

Lakehead University, Thunder Bay, Ontario

By

Antony Raj Thiruppathi

In partial fulfillment of the requirements for the degree of

Master of Science

December 2016

Abstract

Development of Graphite Based Nanomaterials for Green Chemistry Applications

Antony Raj Thiruppathi   **Advisor: Dr. Aicheng Chen**
Lakehead University
December 2016

   Graphite is a valuable natural resource and useful carbon allotrope that has been explored for various applications. Graphene is a two-dimensional (2D) transparent material, which is the strongest, thinnest, and most conductive substance known. Graphene-based materials are strategic nanomaterials that have been investigated for various applications, encompassing water contaminant remediation, energy conversion and storage, and electrochemical biosensors, and graphite is its primary source. This MSc thesis focuses mainly on: (a) the characterization of graphite and the study of its properties, both of which influence the quality of graphene based materials; (b) the development of a novel and simple strategy toward the generation of high quality graphenoids; and (c) the exploration of green chemistry applications such as environmental contaminant remediation and energy conversion and storage.

   Initially, four different graphite samples were characterized to determine their properties, and the surface morphology was imaged using SEM. The specific surface areas of the graphite samples were determined using BET analysis and their thermal stability was examined through TGA and DSC techniques. Subsequently, crystallographic data was gleaned from XRD patterns and further structural information was obtained via Raman spectra. The compositions of the graphite samples were determined through EDX analysis and XPS spectra. The electrochemical characteristics of the graphite, including electrochemical activity, specific capacitance, and potential window were gauged by employing cyclic voltammetry and galvanostatic charging/discharging techniques. This extensive study yielded a detailed comparison of the physiochemical and electrochemical characteristics of the four graphite samples.

Secondly, the same graphite samples were used for the synthesis of graphene oxide (GO), where its properties were extensively investigated. This work generated valuable data toward comparing the capabilities of the various graphite samples in the preparation of graphene oxide. It was found that the properties of a particular graphite sample strongly influenced the quality of the produced graphene oxide. The results indicated that graphite with a high surface area, small crystallite size, moderate defect density, and high oxygen content generated fewer layered graphene oxide with high specific capacitance.

ZEN 915 graphite was selected based on the aforementioned results for the one-pot synthesis of fluorine-doped graphene oxide (FGO). The fluorine content achieved was ~1.0 at%, which showed semi-ionic bonding based on XPS analysis. The morphological characteristics of the graphene were investigated using SEM, TEM, and AFM techniques, where both GO and FGO were similar. Spectroscopic studies were conducted using XRD, Raman, FTIR, and UV-Visible techniques, which revealed that FGO had a high defect density and functional group intensity in contrast to GO. Electrochemical studies revealed that FGO possessed a higher specific capacitance than did GO. Further, FGO demonstrated heavy metal ion detection activity, which was briefly investigated.

I dedicate this effort to my loving mother Raja Sulochana,

whose affection, love, encouragement, sacrifices and prayers define
who I am today.

Acknowledgments

"A journey of a thousand miles begins with a small step, but we must keep on stepping". The successful completion of this thesis is a result of invaluable contributions from a number of individuals along every single step of the way. To say "thank you" is not enough to express my gratitude.

All praise goes to Almighty. Firstly, I thank my Lord and Savior Jesus Christ for bestowing upon me His abundant grace and mercies during the course of my Masters study and indeed, throughout my life.

I express my utmost gratitude to my advisor Dr. Aicheng Chen for his scholarly advice, invaluable suggestions and sustained encouragement throughout the course of my Masters. I am greatly thankful to him for providing me an excellent atmosphere for conducting my research. I would also like to thank my committee members, Dr. MacKinnon and Dr. Thamara Laredo, for their feedback on my thesis. I also wish to extend my gratitude to my Graduate coordinator Dr.Robert Mawhinney for his support.

I give my overwhelming gratitude to Dr. Boopathi Sidhureddy, a post-doctoral fellow in our group, for steady guidance throughout my project. I gratefully acknowledge former and present members of our lab for their cooperation, friendship and helpful suggestions, particularly Dr.Sapan, Dr.Zhongang Liu, Nur, Jesse, and Suresh.

Additionally, I would like to extend my gratitude to the staff of the Lakehead Instrumentation Lab for their constant support, especially Dr. Guosheng Wu, Jiali Wen, Michael Sorokopud, and Martin Griffith. I also wish to thank Dr. Werden Keeler, Professor Emeritus, at Physics department for assisting with Raman spectroscopy studies. I also wish to thank the staff in the Chemistry Department store, Debbie Puumala, and Karen Campbell.

I am extremely grateful to my Mom for her love, prayers, care, and ceaseless support and for the numerous sacrifices she has made in consideration of my wellbeing. I also thank my brother Arul, sister Jeeva, and cousin Periadurai for their constant support and prayers.

I convey my heartfelt thanks to my friend Karen Battigelli (Public Health Nurse, Thunder Bay), for helping me at various stages, and for making me stay peaceful, far from home here at Lakehead. My special thanks goes to Adriel Jebin, Josiah, and Prabhakaran for being a constant source of support, inspiration, and encouragement.

I would like to acknowledge the funding from NSERC and Zenyatta ventures Ltd. and the support of the faculty and staff of the Chemistry Department at Lakehead University. I also greatly appreciate Mr. Peter C Wood (VP Exploration), Dr. Bharat Chahar (VP Market Development) at Zenyatta ventures Ltd. for their valuable feedback and suggestions during the project.

Antony

iv

Development of Graphite Based Nanomaterials for Green Chemistry Applications

Figures

Tables

Abbreviations and symbols

2D – Two dimensional

AACVD- Aerosolassisted chemical vapor deposition

AFM – Atomic force microscope

AG – Artificial graphite

at.% - Atomic percent

BET – Brunauer-Emmett-Teller

BR – Brodie

cm – centimeter

CV – Cyclic voltammetry

CVD – Chemical vapor deposition

DSC - Differential scanning calorimetry

DSSC – Dye sensitized solar cells

EDX – Energy dispersive X-ray spectroscopy

EG – Exfoliated graphite

EIS – Electrochemical impedance spectroscopy

FeCN – Ferri cyanide

FG – Flake graphite

FGO – Fluorinated graphene oxide

FTIR – Fourier transform infrared

FWHM – Full width half maximum

g - Gram

GCE – Glassy carbon electrode

GF - Graphite felt

GIC – Graphite intercalation compounds

GNB – Graphite nanoball

GNP – Graphite nano-platelet

GO – Graphene oxide

HET – Heterogeneous electron transfer

HO – Hofmann

HOPG - Highly ordered pyrolytic graphite

HU – Hummers

Hz - Hertz

ICSD - Inorganic crystal structure database

IR – Infrared

KG – Kish graphite

LOD – Lowest detection limit

LSV – Linear sweep voltammetry

M – Molar

mA – Mili Ampere

mAh – Milli Ampere hour

MCT – Mercury cadmium telluride detector

Mtpy – Million tons per year

mV – Millivolt

MWCNT – Multi walled carbon nanotubes

MΩ - Mega Ohm

nA – Nano Ampere

NADH – Nicotinamide adenine dinucleotide – hydrogen

NFG – Natural flake graphite

nM – Nano moles

OCP - Open circuit potential

PAN – Poly acrylonitrile

PEM fuel cell – Polymer electrolyte membrane fuel cell

PMMA – Polymethyl methacrylate

ppm – Parts per million

PTFE – Poly tetra fluoro ethylene

RFB – Redox flow batteries

RFGO – Reduced fluorinated graphene oxide

RGO – Reduced graphene oxide

RPM – Rotations per minute

SAED – Selected area electron diffraction

SEI – Solid electrolyte interface

SEM – Scanning electron microscope

ST – Staudenmaier

SWASV – Square wave anodic stripping voltammetry

SWV – Square wave voltammetry

TEM – Transmission electron microscope

TETA – Tetraethylene tetramine

TGA – Thermo gravimetric analysis

TO - Tours

UV – Ultra Violet

XPS – X-ray photoelectron spectroscopy

XRD – X- ray diffraction

μL – Micro liters

μM – Micro Moles

Chapter I

Graphite and graphene oxide based nanomaterials for electrochemical applications

1.1 Graphite

Graphite is a conductive allotrope of carbon, where carbons are covalently bonded in planar six membered rings, and are present in layers that are vertically linked by Van der Waals forces. The structure of graphite is shown in Figure-1.1(A), is a 3D hexagonal layered arrangement of sp^2 hybridized carbon. It is the only element mineral that inherently exhibits a perpendicularly aligned hexagonal layer structure. The peculiar structure of graphite gives rise to anisotropic attributes, which means that properties of the material vary with respect to the measured direction (ab direction or c direction). Graphite is a good electrical conductor in the ab direction; however, it behaves as an electrical insulator in the c direction due to the bonding in the ab direction, whereas c direction planes are connected by weak forces. Further, chemical reactivities and reaction rates are higher at edges and defective sites in contrast to the crystalline and basal planes [1]. Furthermore, larger particle sizes and less porous graphite exhibits less reactivity compared to porous structured and smaller particle sized graphite.
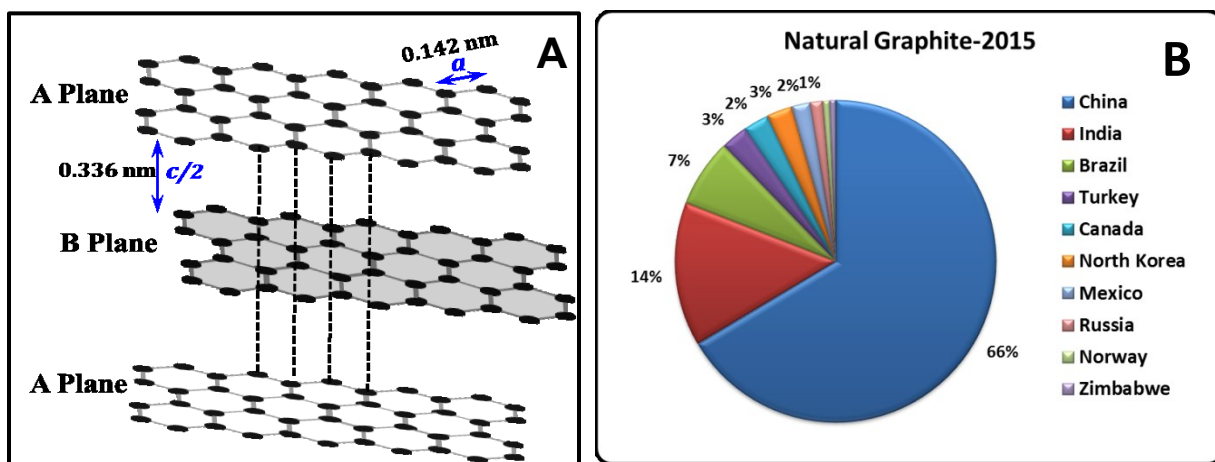
Figure 1.1 (A) Crystal structure of graphite; (B) Graphite producing countries worldwide [2].

Major graphite producing countries include China, India, Brazil, Turkey and Canada. Figure 1.1(B) shows the contribution percentage of different countries in the global market. Graphite demand is continuously growing as it is being developed for a variety of applications and its usage is increasing. The market for graphite exceeds one million tonnes per year ("Mtpy") of which 60% is amorphous and 40% is flake [2,3]. The requirement for graphite is expanding in energy storage, steel production, and other applications. Further, novel materials are being developed from graphite and new applications explored, including environmental remediation and solar applications.

1.2   Classification and properties of graphite

```
                          ┌──────────┐
                          │ Graphite │
                          └──────────┘
        ┌─────────────────────┼─────────────────────┐
   ┌──────────┐         ┌──────────┐          ┌──────────────┐
   │ Natural  │         │Synthetic │          │   Graphite   │
   │          │         │          │          │     based    │
   └──────────┘         └──────────┘          │  materials   │
                                              └──────────────┘
   ┌──────────┐         ┌──────────┐          ┌──────────────┐
   │Amorphous │         │ Pyrolytic│          │  Expanded/   │
   │          │         │          │          │  Exfoliated  │
   └──────────┘         └──────────┘          └──────────────┘
   ┌──────────┐         ┌──────────┐          ┌──────────────┐
   │  Flake   │         │   Kish   │          │   Graphite   │
   │          │         │          │          │ intercalation│
   └──────────┘         └──────────┘          │  compounds   │
                                              └──────────────┘
   ┌──────────┐         ┌──────────┐          ┌──────────────┐
   │   Vein   │         │  Porous  │          │   Graphite   │
   │          │         │          │          │  composites  │
   └──────────┘         └──────────┘          └──────────────┘
                        ┌──────────┐          ┌──────────────┐
                        │ Felt/Foam│          │ Functionalized│
                        │          │          │   graphite   │
                        └──────────┘          └──────────────┘
                        ┌──────────┐          ┌──────────────┐
                        │   Nano   │          │   Graphite   │
                        │          │          │    oxide     │
                        └──────────┘          └──────────────┘
```
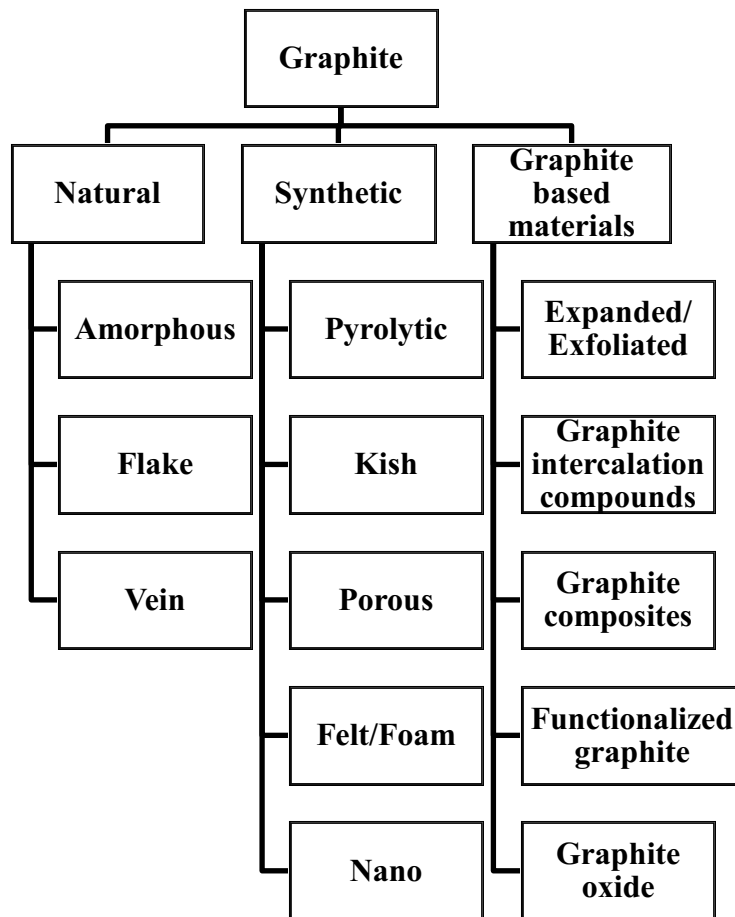
Figure 1.2 Classification of Graphite

The classifications of graphite are shown in Figure 1.2

1.2.1 Natural graphite

Natural graphite can also be called as crystalline ore of carbon which is present in nature in different forms. Natural graphite formed as a result of metamorphism of carbonaceous material. Metamorphism can be defined as change in structure and composition by heat, pressure and weathering. Natural graphite present with other materials as deposits in rocks and it requires processing after mining to separate graphite. Some minerals which contain graphite deposits are quartz, calcite, micas, iron, meteorites and tourmalines. Graphite (cliftonite) has also been found in iron meteorites (e.g. Campo de Cielo and Canyon Diablo meteorites) [4,5]. Geological origin, formation process affects the quality of graphite present. It can be classified in to three different types on the basis of crystallinity and structure.

1.2.1.1   Amorphous graphite

Crystalline form of carbon is graphite, but this type is less crystalline compared to other types. Most abundant among other types, and carries the capacity of 60% of total natural graphite market. It found in meso-morphic rocks namely coal, slate or shale as deposits. Amorphous or micro crystalline graphite formation occurs through aging and metamorphism of carbonaceous material. This occurs in two steps namely carbonization and graphitization. During carbonization organic material converted into carbon residue and by products. Followed by carbon residue undergo deep burial will cause high temperature and pressure leads to graphitization. Graphite content in ore is 30% to 95%, it depends on the geological condition and the location. Amorphous graphite separated through milling and screening. Though it is low in purity, crystallinity and conductivity, it is mainly used as lubricants additive and other applications where crystallinity and purity not needed [4,5].

1.2.1.2 Crystalline flake

Flake graphite is crystalline, soft material, with layered structure. It is present in metamorphic rocks like marble, paragnesiss, iron formation, quartzite, pegmatite and syenite. Graphite content in the ore is varying from 5 to 40%. Though it can be obtained from many places, this is less abundant compared to amorphous graphite. Crystalline flake graphite ore is found in open pits, which is subjected to milling, floatation to obtain graphite. Crystalline flake and vein graphite altogether covers 40% of the overall natural graphite market. Carbon content in flake graphite is about 80-98%. Flake graphite possess more oxidation resistance compared to granular graphite. It is used as anode material for different battery technologies, mainly lithium ion batteries and vanadium redox flow battery, and electrode materials for fuel cells [4,5].

1.2.1.3 Vein Graphite

Lump or Vein graphite is naturally existing crystalline graphite. It is rarest type of graphite, is commercially mined only in Sri Lanka. It is formed from carbonaceous precursor deposited from geological fluid at high temperature and high pressure i.e hydrothermal process. Vein graphite deposits found in igneous rocks. Vein graphite mined from deeper than 600 meters. It possesses highest carbon content 90-99% and is the purest type of graphite. Graphite valued based on its crystallinity and particle size, vein graphite is most expensive compared to other types. Although vein graphite can be used for all the applications of flake graphite, it is chosen only for high technology applications where pure and crystalline graphite is needed, due to its limited availability. It also used for advanced thermal and friction applications such as refractories, car brakes and clutches [4–6].

1.2.2 Synthetic graphite

Synthetic graphite is an accidental invention during late 1800's from unintentional product in the experiment to manufacture silicon carbide by Edward Goodrich Acheson. Currently graphite is been prepared graphite using various carbon precursors. Carbon precursors are divided, based on their graphitizing ability. Soft carbon materials (carbon obtained from coal tar pitch) are readily graphitizable, whereas hard carbon materials are not. Hard carbon materials (carbon obtained from sugar) do not undergo structural changes during the graphitization process. Carbon precursors must undergo phase changes in order to attain the graphite structure. A phase change during the process is required for the movement and rearrangement of atoms which demands high temperatures 3000°C. The starting materials for graphitization contain a combination of fillers, binders, and additives. Coal tar pitch, petroleum derived coke are some precursor (filler) materials. Binder material influences the fluidization of precursor; pitch carbon used as binder. Additives are used in small amount for improve the quality of graphite. Each of these elements influences the resultant structure and properties of the graphite. There are different types of synthetic graphite, associated with precursor, process, morphology, structure, properties, and applications [1,7,8]. Synthetic graphite preparation is energy intensive process which requires harsh process conditions, purification procedures and long time.

1.2.2.1 Pyrolytic graphite

Pyrolytic graphite is prepared from a gaseous precursor which involves the direct deposition of carbonaceous gas by a pyrolysis process [1]. This high temperature operation deposits carbon atoms onto a substrate from a precursor hydrocarbon gas, such as acetylene, methane, etc. Chemical vapour deposition is a desirable process for the preparation of pyrolytic graphite. The structure and properties of the formed graphite is contingent on process parameters, such as gas

pressure, temperature, and gas composition. Pyrolytic graphite exhibits high anisotropy and lower porosity [9,10].

1.2.2.2 Kish graphite

Graphite material that is prepared from skimmed waste steel melts (kish) is called kish graphite. The procedure of kish graphite preparation is depicted in Figure 1.3. In this process a carbonized precursor is entrapped within the interstitial sites of molten steel (kish), which leads to graphitization. The resultant graphite is obtained by leaching out the dissolved carbon from the steel blocks. The temperature range of the steel melt ranges from 1400-2000°C, whereas other processes require temperatures of above 3000°C for graphitization. Carbonized polymeric

Figure 1.3 Procedure for preparation of kish graphite from plastic waste. Adapted from ref [12]. Copyright 2016 Elsevier.

wastes yield high quality kish graphite which is employed as an anode material for lithium ion batteries. The charge retaining performance of kish graphite is higher than other graphite types (between 300 and 600 mAh/g), where the theoretical charge holding capacity of graphite is 372mAh/g [11, 12].

1.2.2.3   *Nano-graphite*

Nanographite encompasses various forms based on the morphology of the graphite structure, including nanofibers [13], nanoplatelets [14], nanosheets [14], nanoparticles [15] and more. The chief specific property of nanographite is its electrochemical activity which is higher at nanoscale due to a more extensive surface area and reduced particle size. Nanographite is electrochemically active, thus it is preferred for various electrochemical applications [16]. Nanographite may be prepared from various precursors including ethanol [17], methane [18], polymeric precursors [19], natural graphite [16] etc. The preparation method and precursor influence the characteristics of the nanographite and guide its applications. Mechanical milling methods [15] may be used to modify graphite to nanographite through the introduction of defects, and by reducing the size and shape of particulates. Using another technique, graphite nanosheets may be fabricated in three steps, namely acid intercalation, to prepare graphite intercalation compounds (GIC), followed by microwave irradiation to initiate exfoliation and ultrasonic exfoliation in organic solvents to obtain nanosheets. Interestingly, the yields of the nanosheets are influenced by the solvent viscosity rather than the surface tension [20]. The precursor, preparation methods, and applications of the various forms of nanographite are shown in Table - 1.1.

Table 1.1 Nano-graphite: methods of preparation, precursor and application

Type	Method	Precursor	Application	Ref
Nanographite film	Chemical vapour deposition	Methane-hydrogen	Cathode material in electron gun for space application	[18]
Graphite nanofibers	Chemical vapour deposition	Acetylene		[13]
Nanographite	Heat treatment and graphitization	Hydrolysis lignin	Prepare GIC, expandable graphite	[21]
Graphite nanofibers	Stablization, carbonization, graphitization	Poly acrylonitrile (PAN)	Improved electrical conductivity	[19]
Nanoflake graphite	Chemical oxidation and ultrasonication	Natural graphite	Phenol degradation	[16]
Graphite nanosheets	Ultrasonic powdering	Natural graphite	-	[22]
Graphite with onion-like carbon hollow nanostructure	Hot pressing sintering	Natural graphite	Anode-lithium ion batteries	[23]
Nanocrystalline graphite	Aerosol assisted chemical vapour deposition (AACVD)	Toluene	Photovoltaic application, magnetotransport properties	[24]
Plate like graphite nanoparticles	Mechano-chemical milling	Graphite microparticles	Environmentally compatible method	[15]
Graphite nanosheets	Detonation technique	Natural graphite	Surface area increased 8 times, convenient and effective method	[25]
Graphite Nanoparticles	Mechanical milling	Coarse graphite particles	Strain free graphite, economical method for preparation of nanoparticles	[26]
Graphite nanosheets	Low energy pure shear milling	Graphite powder	-	[27]
Graphite nanoplatelets	Chemical exfoliation (formic acid)	Natural graphite	Graphene production	[14]
Graphite nanosheets	Low current plasma discharge	Ethanol	precursor for producing few layer graphene	[17]
Graphite nanohillocks	Plasma etching	Highly oriented pyrolytic graphite	-	[28]

1.2.2.4 *Porous Graphite*

Porous graphite is classified based on its morphology, which is porous in nature. Porous

graphite may be classified based on its pore dimensions by microporous (up to 2 nm pore size)

and mesoporous (2 to 50 nm pore size) graphite. Porous graphite has low density and a high surface area.

Nanoporous graphitic carbon is produced from a non-graphitizing polymeric precursor, such as polyfurfuryl alcohol [29]. Wang et al. reported on a carbon-carbon co-assembly in the preparation of mesoporous graphitic carbon from resol (formaldehyde and phenol reacted with sodium hydroxide). It possessed a mesoporous structure and demonstrated improved performance in the selective oxidation of benzyl alcohol to benzaldehyde [30]. Sadekar et.al reported on the preparation of porous graphitic aerogels from acrylonitrile. The acrylonitrile was subjected to gelation to prepare polyacrylonitrile (PAN) aerogels, which were then aromatized in ambient air and subsequently carbonized and graphitized to obtain porous graphite aerogels. Figure 1.4 shows the SEM image of the as-prepared porous graphite aerogels [31].
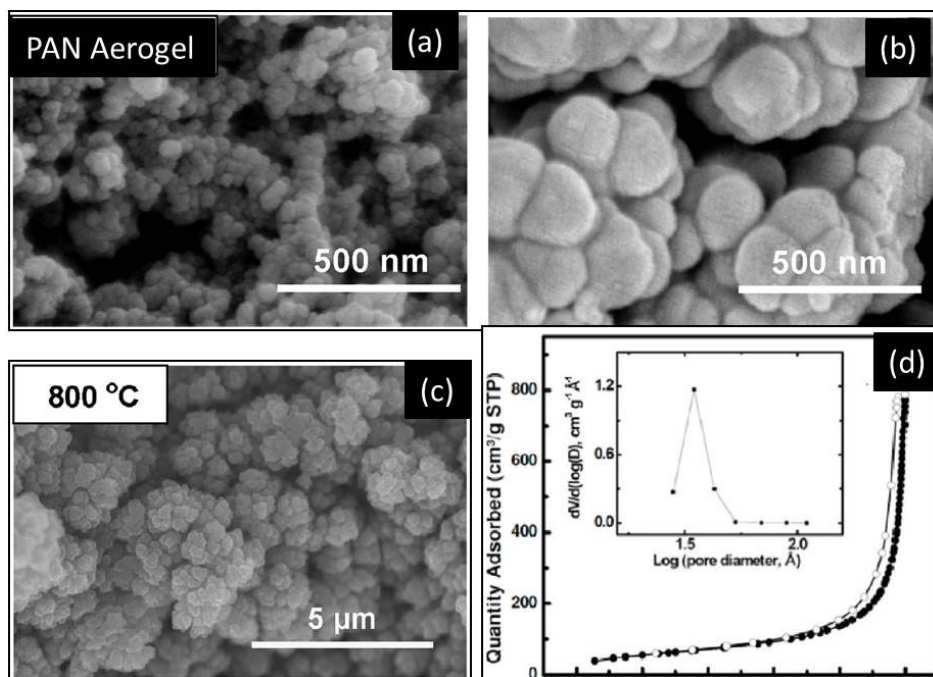
Figure 1.4 Porous graphite prepared from acrylonitrile. Representative SEM images of (a) gelated acrylonitrile (PAN), (b) after the aromatization of PAN and (c) following graphitization of aromatized PAN at 800 °C. (d) Nitrogen absorption of graphite aerogel. Adapted from ref [31]. Copyright 2012 American Chemical Society.

Several studies have discussed the modification of graphite to porous graphitic materials. Pyrolytic graphite was electrochemically etched in a HF (49%) and ethanol solution with a platinum counter electrode, and etching instigated the generation of microspores within the graphite [32]. In another work, graphite was modified to porous graphite by an acid treatment; whereafter metal nanoparticles were introduced to form a nanocomposite. The as-prepared nanocomposite demonstrated an excellent capacity for hydrogen storage [33].

1.2.2.5 *Graphite felt and foam*

Graphite felt received its name due to its morphology which is similar to felt fabric material. This type of graphite has a low thermal conductivity, high surface area, is lightweight, flexible, and is a moderate electrical conductor. Graphite felts (GFs) have been explored as an electrode material for redox flow batteries (RFBs) due to their liquid permeability and surface area; however wettability is concern because of its hydrophobic property [34]. The wettability of the graphite felt was enhanced by surface activation via KOH through the introduction of an oxygen related functional group. SEM images of the graphite felt, prior to and following this treatment, are shown in Figure 1.5A, where the surface became roughened in contrast to before the treatment [35]. Microwave treatment introduces hydrophilic hydroxyl groups within the graphite felt, which improves its performance as the cathode in a vanadium redox flow battery [36].

Graphite foam is another class of graphite with a different morphology similar to a foam-like structure. Its specific properties are a porous structure, low density, high thermal conductivity, and high specific surface area. The preparation of graphite foam involves three primary steps: foaming, carbonizing, and graphitization. The foaming pressure influences the pore size and the foam thickness. Graphite foam has been prepared by different methods, such as the blowing

method, using a polymer template, and the compression of graphite. Figure 1.5(C) illustrates the blowing method for the preparation of graphite foam from pitch carbon. Pitch carbon is placed along with a blowing additive in a pressure vessel, and subjected to a high temperature treatment [37]. The applications of graphite foam are fire-resistant materials, catalyst supports, and specific thermal conductivity in microelectronics and aeronautics industries [38].
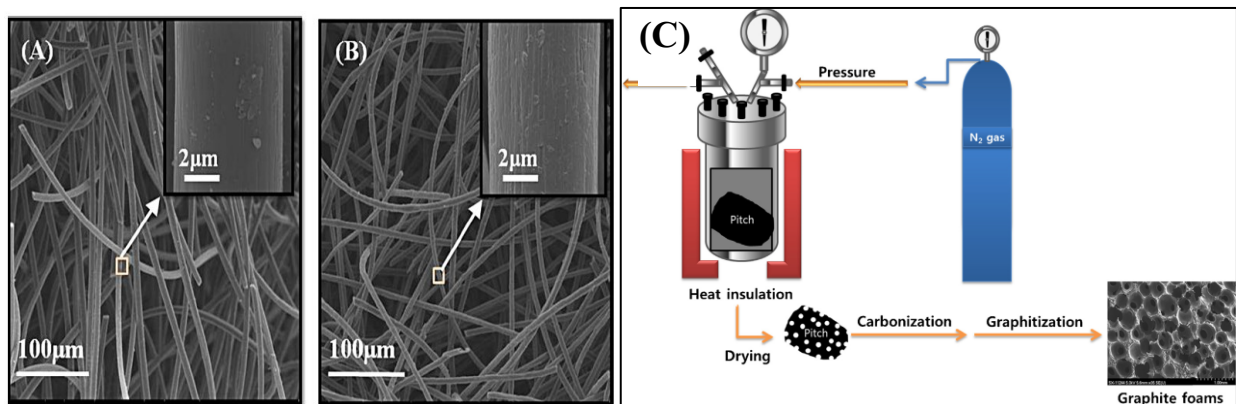
Figure 1.5 SEM images of (A) Raw graphite felt and (B)KOH treated graphite felt. Adapted from ref [35]. Copy right 2015 Elsevier. ; (C) Graphite foam preparation by the blowing method. Adapted from ref [37]. Copyright 2015 Elsevier.

1.3   Graphite based nanomaterials

Graphite may be modified using various methods encompassing thermal, mechanical, chemical, electrochemical, and intercalation. The structures get their different names based on the modification technique.

1.3.1 Expanded and exfoliated graphite

Expanding the interlayer distance of graphite by various means produces expanded graphite, which exhibits an increase in volume based on the extent of expansion. A comparison of the various methods that are used to expand the graphite and a SEM image of the expanded graphite is shown in Figure 1.6(A) and (B), where the volume change varies with respect to the expansion technique. Expanded graphite is prepared through graphite intercalation compounds or

the oxidation of graphite[39,40]. Expanded graphite exhibits the specific properties of thermal stability, elasticity, low density, and high volume. It is used primarily as an additive in the formulation of composites for fire retardant applications [16].
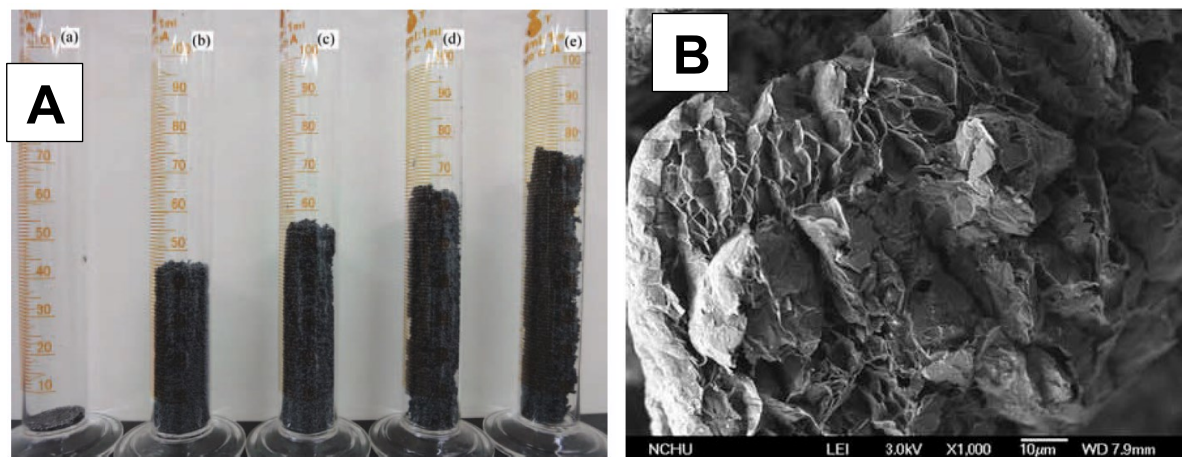
Figure 1.6 (A) a- Natural graphite; b- conventional liquid phase expanded graphite; c-ultrasound irradiation expanded graphite; d-hydrothermal expanded graphite, e-H_2O_2 assisted hydrothermal method, and (B) SEM image of H_2O_2 assisted hydrothermal expanded graphite. Adapted from ref [39]. Copyright 2012 John Wiley and Sons.

Exfoliated graphite is a graphite phase that is obtained through the application of an external force to a graphite intercalation compound. During exfoliation the intercalant is evaporated, which causes the high pressure to overcome the Van der Waals forces between the layers, these layers are subsequently separated due to the pressure generated, which reduces the density. Exfoliated graphite exhibits high lubricity and thermal stability. Graphite or graphite intercalation compounds have been exfoliated by heating. Different modes of heating have been attempted to facilitate the exfoliation process, including furnace, plasma, laser heating, and microwave [41]. Exfoliated graphite has been used as adsorbent, in gaskets, as a filler, thermal insulator, an as an element in fire resistant composites [42]. Exfoliated graphite degrades more readily in contrast to graphite.

1.3.2 *Graphite intercalation compounds*

The insertion of a guest molecule or atom between the layers of graphite forms a graphite intercalation compound (GIC), where the inserted material alters the property of GIC. GIC is a good conductor; however, its physical properties include high anisotropy. GIC is an intermediate in the preparation of expanded graphite and in the exfoliation of graphite, and depending on the intercalant and the method employed, the intercalation intensity may vary. Intercalation may be explained by stages; for example stage-2 means that there are two layers between the intercalant layers; hence stage-1 obviously contains more intercalants compared to others. The stage structure of $FeCl_3$ intercalated graphite is illustrated in Figure-1.7 [43]. GIC may be categorized in to two types based on the nature of the intercalant (e.g., acceptor GIC and donor GIC). Some acceptor intercalants are HSO_4^- or NO_3^-, and donor intercalants are Li^+ and K^+ [44]. GIC can be
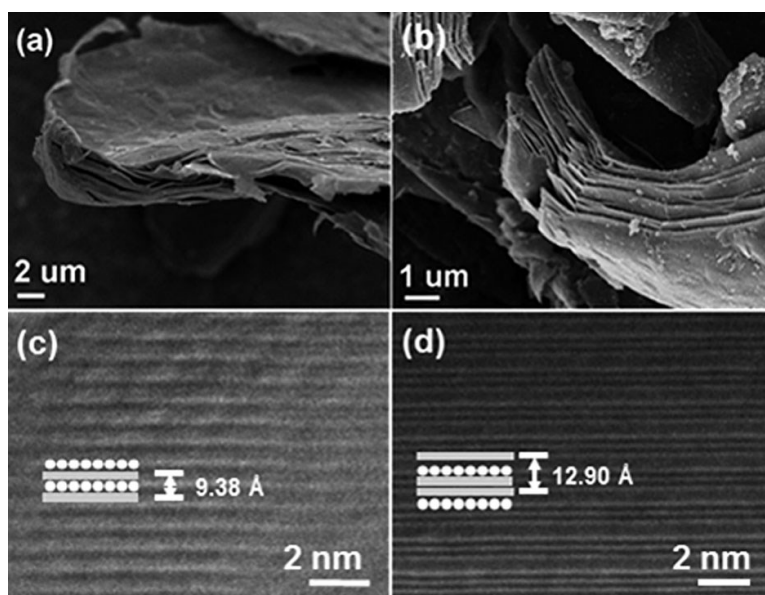
Figure 1.7 SEM images of (a) stage 1 $FeCl_3$–GICs and (b) stage 2 $FeCl_3$–GICs; High resolution transmission electron microscope (HRTEM) images of (c) stage 1 $FeCl_3$–GICs and (d) stage 2 $FeCl_3$–GICs. The round symbols represent the layers of ferric chloride, and the bars represent the layers of graphite. Adapted from ref [43]. Copyright 2014 John Wiley and Sons.

prepared utilizing physical, chemical, and electrochemical methods [45-48]. GIC is employed in various applications, encompassing energy storage (lithiated graphite) [49], adsorbents (for wastewater treatment) [48], intermediate in the preparation of graphene related materials [50], and other applications (e.g., hydrogen storage) [51].

1.3.3 Graphite composites

Graphite that contains metal nanoparticles (Ag) [52], metal oxides (SnO_2) [53], metalloids (Si) [54], non-metals (P) [55], or polymers (polyurethane) [56] are referred to as graphite composites. Graphite composites are attractive modifications that have been developed for variety of applications, such as Li ion batteries [55], electrocatalysis [57], fuel cells [58], electroanalysis [59,60], photocatalysis [61], lubricating materials [62], thermal energy storage [63], etc. The rationale for using graphite relates to its attractive properties, surface area, conductivity, and earth abundance. Graphite assists with enhancing the performance of materials, such as being an additive for thermal or lubricating materials. Graphite may also serve as a host for the storage of catalytic species, such as metal nanoparticles, to augment the surface area and conductivity. Metal/metal oxide nanomaterials may be combined with graphite to enhance performance, for example, the addition of phosphorus enhances the working voltage of graphite in lithium ion battery applications [55].

A grown SnO_2 nanorod/graphite nanocomposite was prepared via a hydrothermal method [53]. The preparation method had three steps, with the scheme shown in Figure 1.8. Initially, graphite was activated by treatment in nitric acid and hydrochloric acid followed by treatment with $SnCl_4.5H_2O$ and NaOH to form SnO_2 seeds on the graphite surface. The third step was to control the growth and dimensions of SnO_2 nanorods on graphite through a hydrothermal

process. . The controllable diameter of the SnO_2 nanorods improved the cyclic stability of the composite material for reversible storage of lithium.
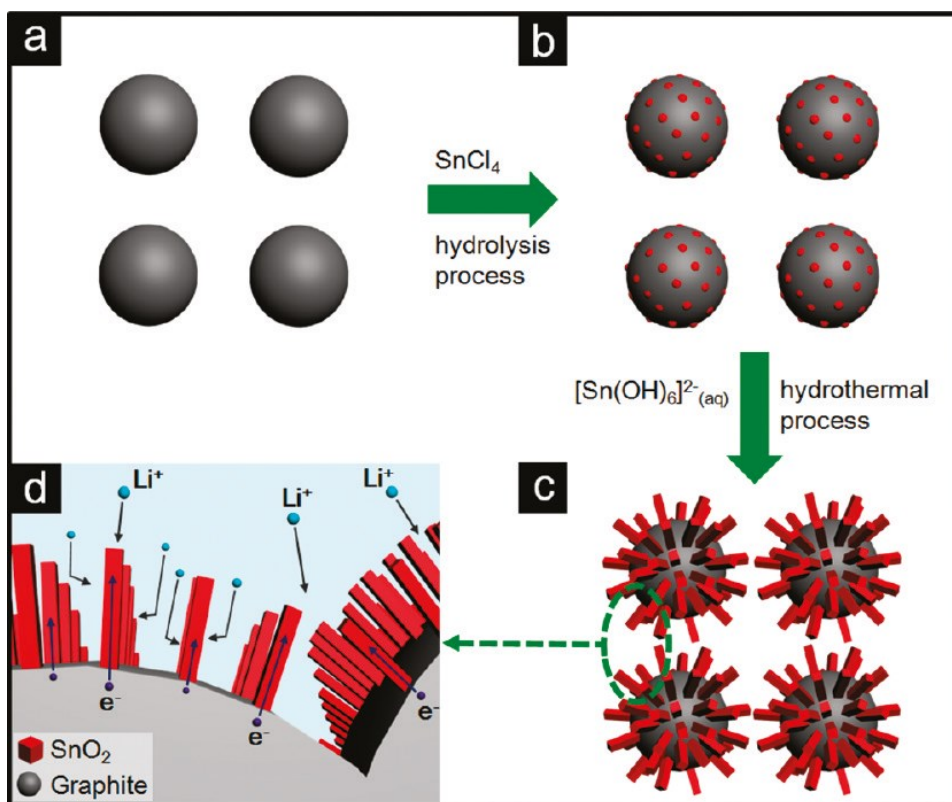
Figure 1.8 Scheme for SnO_2 nanorods growth on graphite. Adapted from ref [53]. Copyright 2011 American Chemical Society.

Graphite is primarily composited with polymer to improve both electrical and thermal conductivity [64]. Some recently reported graphite composites for various applications are shown in Table -1.2 which compares different composites, preparation methods, and applications.

Table 1.2 Graphite composites: applications and preparation methods.

Materials	Applications	Preparation Methods	Ref
Graphite/phosphorus	Li ion battery - anode	Thermal vapour deposition	[55]
Lead dioxide/graphite polymer composite (poly-methyl methacrylate (PMMA)	Electrochemical chlorine generation-anode	Wet chemical synthesis	[65]
Silicon carbide reinforced graphite composite	Lubricating materials	Hot-pressing process	[62]
Graphite-Polyurethane	Sensor for tetracyclines in bovine urine	By mixing in mortar, and extrude in form of electrode	[56]
Exfoliated graphite-phenolic resin	Bipolar plate - PEM fuel cell	Compression molding	[64]
Expanded graphite-nitrates and eutectic nitrate mixtures	Phase change material	-	[66]
Graphite-Ag nanoparticle	Supercapacitor	Wetting-thermal decomposition	[52]
Graphite-polyethylene	Electromagnatic shielding	Mechanical mixing plus hot compaction	[67]
RuO_2 decorated graphite nanoplatelets-multi-walled carbon nanotube	Supercapacitor	Graphite nano-platelet and MWCNT mixing in acid medium to prepare hybrid structure RuO_2 chemically reduced onto GNP/MWCNT	[68]
Graphite-supported ultra-small copper nanoparticles	Catalysis - Meerwein arylation of pyrroles	Cu nanoparticles reduced from copper acetate on to the graphite in presence of hydrogen at 25°C	[57]
Expanded graphite/phenolic resin	Adsorbent – CO_2	Expanded graphite mixed with phenolic resin, then carbonized and activated with CO_2	[69]
Graphite–Au nanoparticles	Electroanalytical – glucose, H_2O_2 determination	Graphite mixed with citrate encapsulated Au nanoparticle solution reaction carried out at room temperature for 15 min.	[60]
Eutectic chloride/expanded graphite	Thermal energy storage	Physical blending of liquid salts with expanded graphite	[63]
SnO_2 nanorod-planted graphite	Li-ion batteries	Hydrothermal method	[53]

1.3.4 Functionalized graphite

Functionalization simply refers to the introduction of a specific functional group onto graphite in order to enable a specific property, such as catalytic activity, strength, conductivity and dispersibility [70–72]. Functionalization may be accomplished using various methods including wet chemical, physiochemical, electrochemical, photochemical, plasma treatment, etc [70,72–75]. The interaction of functional groups with graphite may differ depending on whether the functional groups are integrated through covalent or non-covalent means [71,76]. Functionalized graphite is useful as effective filler additive for polymer nanocomposites as it improves the dispersibility and interfacial interactions[71]. Thus graphite may be utilized as excellent platform for functionalization with different moieties. This type of modifying graphite is tunable to control the properties and performance of the resultant material.

1.3.5 Graphite oxide

Graphite oxide is produced through the treatment of graphite using chemical or electrochemical oxidation, as pristine graphite does not possess functional groups. Graphite oxide retains a layered structure, the interlayer distance is increased due to the addition of oxygen functionalities, lower conductivity and thermal stability. Graphite oxide is prepared using the chemical oxidation of graphite through the methods of Brodie [77], Staudenmaier [78], Hummers' [79], Tour [80], and modifications thereof. The Lerf-Klinowski model proposes hydroxyl and epoxyl functional groups on the basal planes, and carbonyl and carboxyl groups near the graphene edge planes [81]. The Staudenmaier and Brodie methods use perchlorate as oxidizer, whereas Hummers' and Tour's methods use a $KMnO_4$ oxidizer. The addition of oxygen to graphite introduces sp^3 hybridization, which reduces the conductivity. Thus graphite oxide acts as a semiconductor, where conductivity decreases as the oxygen content increases [82].

Important properties of graphite oxide are layered structure and negatively charged surface [83]. Graphite oxide is hydrophilic in nature, and thus, it may be easily dispersed in water/solvent. Upon sonication/agitation graphite oxide is transformed to graphene oxide. An exfoliated monolayer (bi/few layered graphite oxide) is called graphene oxide. Graphite oxide and graphene oxide both exhibit similar chemical properties due to functional groups. Graphite oxide, as such, is employed as an effective adsorbent for cationic dyes (e.g., methylene blue), where the negatively charged surface of graphite oxide attracts the dye molecules. The maximum adsorption capacity of graphite oxide is 751.9 mg/g (methylene blue), and it has been observed that a degree of oxidation increases the adsorption capacity, whereas it decreases when exfoliated to graphene oxide [84]. Graphite oxide is a promising precursor in the preparation of graphene derivatives.

1.4 Graphene oxide derivatives

1.4.1 Graphene

Graphene comprises a one atom thick two-dimensional material, or single layer of graphite. It was successfully isolated via a micromechanical method in 2004, and its use in various applications exploded due to a myriad of attractive properties. Various technologies are under development toward the generation of applications for graphene, as it has been demonstrated that graphene is the strongest, lightest and thinnest material known. Additionally it is transparent, conductive, and flexible [85,86]. There are currently numerous publications that describe the preparation of graphene using various methods.

Graphene preparation may be classified under two strategies, namely, top down and bottom up approaches. The bottom up approach involves the growth of graphene on a substrate using various techniques, such as chemical vapour deposition (CVD), epitaxial growth, and others [87].

In this approach experimental conditions demand sophisticated instruments for producing high temperatures, ultrahigh vacuum, and require ultrapure reagents and substrates. Bottom-up approaches may produce ultrathin, transparent graphene; however, scaling up is challenging due to cost. Another limitation is that although CVD can produce large area graphene, it is only in the form of thin films. The advantages of these methods are that they can produce monolayer graphene and flexible electrodes, under controllable processes [88,89].

An alternate approach is top-down, where graphene is prepared from a graphite source, and graphite is exfoliated into a few or single layers of graphene. Although the preparation of graphene began from the micromechanical cleavage of graphite [90], it evolved to include chemical methods, such as reducing graphene oxide [91], physical methods, such as solvent exfoliation [92], electrochemical exfoliation [93] and other solvo-thermal techniques [94], etc. Based on these different methods, the nature and properties of graphene is altered, and its quality is assessed through the number of layers, process duration and complexity, yields and process scalability.

1.4.2 Graphene oxide

Graphene oxide is single layer graphite oxide, and is a 2D graphene platform decorated with oxygen-functionalities. Due to the presence of polar oxygen functional groups it may be easily dispersed in water or organic solvents via sonication. With respect to the sonication power and duration, the extent of exfoliation may be controlled. The species and quantities of functional groups that are present in graphene oxide are difficult to precisely quantify; hence, its exact structure is difficult to define. The properties of graphene oxide are distinct from graphene due to the presence of functional groups. Chemical oxidation introduces defects, and functional groups can initiate the reduction of electrical conductivity [95]. Graphene is produced from graphite

oxide/graphene oxide through reduction. The reduction of GO improves its conductivity; thus it is also used to prepare other graphene derivatives. There are different processes employed to reduce graphene oxide, namely thermal, microwave, chemical, and electrochemical methods [96–99]. Each type of reduction technique yields different classes of graphene / reduced graphene oxide with respect to defects, functionalities, and performance.

Novel methods have been explored in the synthesis of graphene oxide, with the view to reduce the duration of the process, improve yields, as well as to control defects and oxygen content. Potassium ferrate is utilized as an oxidizer to synthesize graphene oxide within an hour. This is made possible by the in-situ generation of atomic oxygen; in addition, the recycling of excess sulfuric acid makes the process economical. Further, it exhibited a high C/O (2.2) ratio and improved dispersion [100]. Graphene oxide from expanded graphite is synthesized via a rapid method with the assistance of ultrasonication. In addition, this strategy is greener compared to conventional methods [101]. The oxo-functionalization of graphite by conducting the oxidation below 10°C reduces the defects within the carbon lattice. It demonstrates high charge carrier mobility and may produce high quality graphene [102]. The oxygen content in graphene oxide may be tailored for particular applications. By adjusting the quantity of oxidizer and reductant the desired oxygen content can be achieved. It has been determined that a 20-40% oxygen content is optimal for imparting excellent performance in capacitors, catalyst supports, and biosensors [103]. Controlling the temperature of synthesis influences the graphene oxide size and C/O ratio. When the temperature is increased, the carbon content is higher and size of the sheets decrease [104], and the dispersing ability of GO facilitates further processing. Graphene oxide's properties may be tuned through modification with different materials. Functionalized GO has been explored for various electrochemical applications [105].

1.4.3 Halogenated graphene oxide

Halogen functionalization onto graphene oxide is an attractive modification as it can tune the electronic configuration and electrochemical properties of graphene oxide. The incorporation of chlorine reduces the bandgap to 0.9 eV, and iodine will still reduce to 0.0 eV [108]. In contrast, fluorine doping increases the bandgap. F-graphene exhibits faster electron transfer compared to other classes of graphene. The order of electron transfer is F-Graphene > Cl-Graphene > Br-Graphene [105]. Different approaches have been explored for the halogenation of GO, namely the hydrothermal method, direct gas halogenation, electrochemical methods, and chemical methods [106–109]. Halogenated graphene derivative applications have been reported as a supercapacitor electrode material, electrocatalysts for hydrogen evolution, oxygen reduction reactions, and electrochemical sensors [109,110].

1.4.4 Heteroatom doped graphene oxide

Heteroatom-doped graphene oxide is another well explored graphene oxide functionalization, where nitrogen, boron, phosphorus, and sulphur are covalently or semi-ionically doped within graphene oxide. In addition to the co-doping of two heteroatoms, heteroatom-halogen has also been studied for catalytic applications [111]. The introduction of heteroatoms into the graphene platform can initiate catalytic activity, improve conductivity, and instigate changes in its electronic structure [112]. N-doped graphene is well recognized for oxygen reduction catalysis. N-doping enhances the electron density of graphene which facilitates the electron donating ability of N-doped graphene [113]. Preparation methods of graphene-heteroatom composites include thermal annealing, electrochemical, and hydrothermal methods [114–116]. N-Graphene oxide has also been reported for supercapacitor and sensing applications [117,118].

1.4.5 Metal nanoparticle/metal oxide - graphene oxide

Graphene oxide decorated with metal nanoparticles, metal oxides, are useful structures for various applications. Metal nanoparticles and metal oxide are combined onto graphene oxide in the preparation of hybrid structures. Metal nanoparticles/metal oxides act as spacers to maintain the interlayer spacing of the graphene sheets, and in addition, they incorporate catalytic activity to the composite. The role of metal oxide dopant is to stabilize the growth of metal nanoparticles, as well as to minimize electrode poisoning [119]. Preparation methods include hydro/solvo thermal, photodeposition, microwave irradiation, electrochemical, and chemical methods, etc. [120–123]. Metal nanoparticle-GO composites are employed for catalytic applications, namely, alcohol oxidation, oxygen reduction, and water splitting reactions [119,123]. Graphene/metal oxide composites have also been explored as energy storage materials for lithium ion batteries and electrochemical capacitors. Graphene platform improves conductivity while providing anchoring sites for metal oxides [124].

1.5 Applications of graphite derived nanomaterials

Graphite based nanomaterials have numerous applications in various fields such as energy storage and conversion, catalysis, sensors, and photovoltaics, etc. The roles and benefits of graphite and its derivatives are briefly described in this section.

1.5.1 Batteries

Graphite is a commercial anode material for lithium ion batteries. In order to improve its performance and to meet growing demands, various modified versions of graphite have been reported. Graphite has been modified to various forms such as graphite with coatings, surface etching, and composites for lithium ion battery applications. The modification of graphite has been investigated to improve performance attributes, including long cycle life, increased

reversibility, and rate capabilities [125, 126]. In addition, graphite-based materials are used in redox flow batteries as anode materials to improve their stability.

The surface modification of graphite may be accomplished by mixing it into a 7M KOH solution under stirring for 12 hours, with subsequent filtering using a PTFE membrane and drying in vacuum [125]. Following the treatment, KOH crystals are attached to the surface of the graphite. The scheme of the KOH etching of graphite is shown in Figure-1.9(A). KOH etching modifies the graphite surface and creates additional sites for Li ion intercalation and de-intercalation. It also reduces the distance required for Li ion transport; hence, the fast diffusion of ions will enhance the speed of charging. This surface treatment also increases the coulombic efficiency, rate capability, and cyclic stability (Figure-1.9(B)), and this structural modification of graphite is called multichannel graphite [125]. Similarly, NaOH treated graphite prevents solvent co-intercalation through the modification of SEI which initiates an increase in first cycle reversible capacity [126].
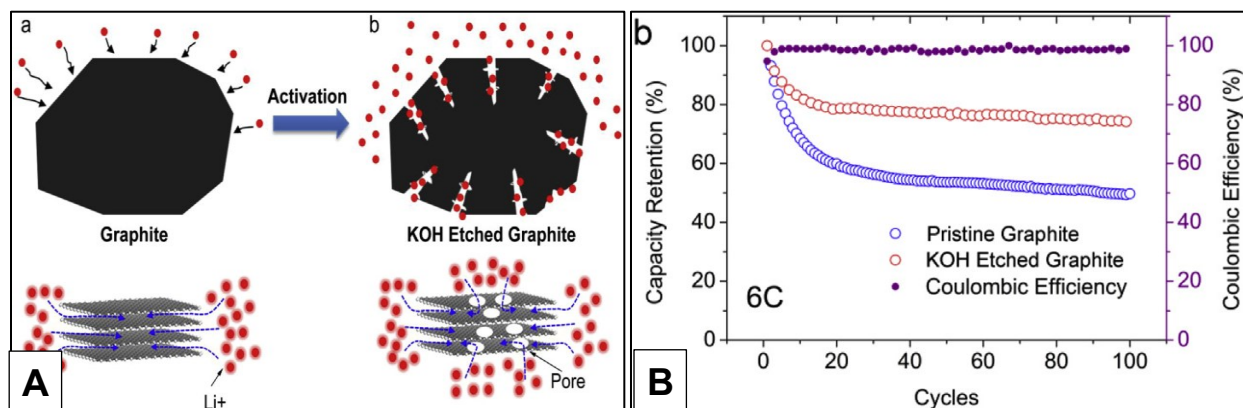
Figure 1.9 (A) Scheme of KOH etched graphite; (B) Cycle life performance at 6C of KOH etched graphite. Adapted from ref [124]. Copyright 2015 Elsevier.

A graphite/Si/amorphous carbon composite was assembled using a pyrolysis method, where composite self-assembly was accomplished by exploiting attractive electrostatic forces [127]. Graphite was oxidized to form a negatively charged surface, and Si was functionalized to form a

positively charged surface. This composite exhibited high performance capacity and stable coulombic efficiency over 20 cycles. Compositing with graphite acts as a buffer to overcome volume changes, and provides a stable structure to maintain a reversible capacity [127].

Graphite based materials are used as negative electrode material in redox flow batteries. The desired characteristics of graphite toward improving the electrochemical performance of the battery are the presence of trace amounts of oxygen functional groups [128-130]. The presence of these functional groups improves the wettability and reactivity of the electrode. In addition, graphite is typically selected due to its wide operating potential, stability, and reversibility. Various graphite materials including graphite felt and HNO_3 treated graphite have been reported to improve the performance of vanadium redox flow batteries [128–130].

1.5.2 Electrochemical capacitors

Graphite composites with metal, metal oxide, graphite intercalation compounds, and surface treated graphite have been reported as capacitor electrode materials [52, 131, 133, 134] . The addition of other materials with graphite improves the capacitance and energy density of capacitors.

A thermal wetting decomposition method was employed to incorporate Ag metal into graphite. This composite exhibited a 10 times higher capacitance, in contrast to bare graphite [52]. Noble metals are incorporated to mediate electrochemical reactions as catalysts in order to increase the energy storage capability and power density of capacitors. The basis of the performance is the addition of pseudocapacitance from the Ag and its catalytic effect. Pseudocapacitance derives from lithium intercalation and is consistent with CV and EIS results, where the increased capacitance resulted in high energy and power outputs [52].

A ruthenium oxide decorated multiwall carbon nanotube (MWNT)/graphite nanoplatelet (GNP) nanocomposite was shown to have electrochemical capacitance properties [131]. The hybrid nanostructured MWNT served as spacer to minimize the restacking of the graphite nanoplatelets. The higher capacitance was attributed to dual charge storage, namely, the double layer capacitance of GNP/MWNT, and the faradaic capacitance from RuO_2; RuO2-GNP/MWNT exhibiting 125 F/g capacitance, which was 7 fold higher than the GNP/MWNT composite [131].

Graphite intercalation compounds have also been reported for capacitor applications, with a notable material being pre-lithiated graphite, which has undergone intensive investigations [133]. Natural graphite was treated with H_2O_2 using different ultrasonic energies which yielded surface modified graphite, reduced particle size, and increased surface area in contrast to pristine graphite. Modified graphite showed improved capacitance retention compared to its unmodified counterpart, and a carbonyl functional group within its structure, which was confirmed by FTIR. In addition it also increased the first cycle coulombic efficiency by effectively modifying the SEI [134]. Graphite-based materials possess various advantages, namely, an improvement in capacitance, increased power output, and durability of the material in capacitor applications.

1.5.3 Electrocatalyst

Graphite nanocomposites with metal nanoparticles have primarily been reported for catalytic applications [136]. Graphite nanofibers and graphite nanoplatelets were reported to be involved with the preparation of catalysts [135]. Graphite acts as a catalyst support for the mounting of catalytic nanoparticles, and in addition, it enhanced the activity and stability of material. Thus, high surface area, good conductivity, and chemical stability are desirable characteristics of graphite when used as catalyst support. Oxygen reduction and methanol oxidation are catalyzed using graphite nanocomposites for fuel cell applications [135, 136].

Nanoscale graphite was employed as a catalyst support for a polymer electrolyte membrane fuel cell for the oxygen reduction reaction, and demonstrated improved activity and stability over a commercial Pt/carbon black catalyst. The stability of catalyst was examined by accelerated destructive test cycles, where the graphite/Pt catalyst exhibited higher corrosion resistance than the commercial catalyst [135].

A. Döner et al. reported on nickel promoted Cd coated graphite as a catalyst for methanol oxidation in direct methanol fuel cells [136]. C.M. Park et.al investigated how the surface treatment of graphite nanofibers influenced catalytic activity. It was shown that the presence of oxygen functionality improves catalytic activity due to an increased capacity for the loading of metal nanoparticles [134].

A molybdenum phosphide-graphite composite was prepared using mechanical milling, which had good activity for the generation of hydrogen from water [132]. Its activity for the electrocatalytic production of hydrogen was the result of superior conductivity and a high surface area. Graphite provides a conductive support, which is another reason behind its improved activity. The performance of this material compared with bare MoP and G-Mo-P under various milling times and different compositions using LSV is depicted in Figure-1.10.
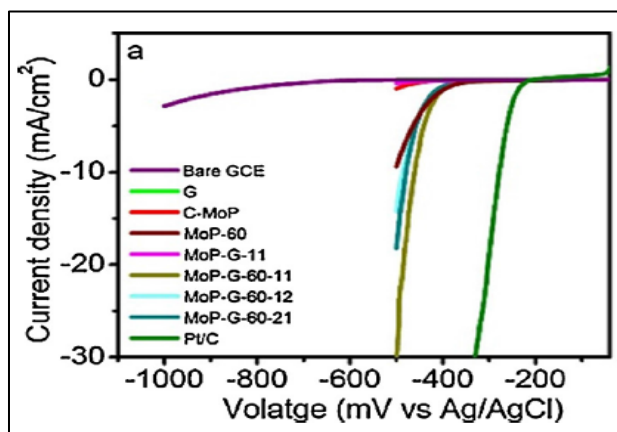
Figure 1.10 Linear sweep voltammograms of MoP-G compounds compared with that of bare GCE, graphite, and Pt/C. Adapted from ref [132]. Copyright 2015 Elsevier.

1.5.4 Electrochemical sensors

Graphite based materials have been reported for various sensing applications. Different roles of graphite include support for the sensing moiety, substrate, etc [137-139]. Structural defects and functional groups that are present in graphite assist with improving the electrochemical activity of the sensing platform. Different classes of graphite have been reported for sensing applications, such as pyrolytic graphite, graphite felt, exfoliated graphite, graphite composites, and pencil graphite. Graphite assists primarily with improving the stability and long term usability of the sensor, as it is chemically inert [138-140].

A single wall carbon nanotube-modified pyrolytic graphite electrode was reported for the simultaneous detection of adenine and adenosine monophosphate [137]. Exfoliated graphite comprises an electrochemically active low density natural graphite material that may be compressed easily for fabrication. It is prepared by intercalation followed by thermal shock and has been demonstrated to detect the phenolic pollutant bisphenol A [138].

Graphite felt, modified by Prussian blue, and platinum nanoparticles have been reported for the sensing of hydrogen peroxide. This sensor exhibited a low detection limit of 1.2 nM with a high sensitivity of 40.9 A/cm^2/mol. Graphite felt was used as substrate with high conductivity, high surface area and chemical stability [139]. An unmodified edge-plane pyrolytic graphite electrode was reported as a pH sensor, where a quinone functional group present in the graphite structure's reduction potential varied with respect to the pH of the medium [140].

Electrochemically modified pencil graphite was demonstrated as a free chlorine sensor [141]. Pencil graphite is easily available, and simple electrochemical oxidation was performed in phosphate buffer and ammonium carbamate to introduce amine radicals into the graphite structure. An increased chlorine concentration in test media was indicated by an increase in the

cathodic current. The scheme of the fabrication and operation of pencil graphite as a chlorine sensor is shown in Figure 1.11.
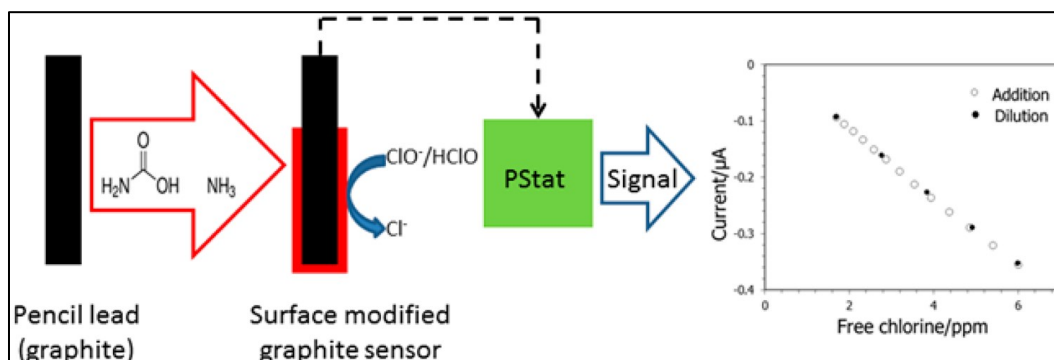
Figure 1.11 Scheme of fabrication and operating mechanism of surface-modified pencil graphite chlorine sensor. Adapted from ref [141]. Copyright 2015 American Chemical Society.

A gold nanoparticle and phthalocyanine-modified graphite paste electrode was reported for the detection of cysteine, which exhibited improved sensitivity compared to bare graphite, due to low electron transfer resistance [142]. Several examples of graphite based sensors with data to convey their capabilities are listed in Table 1.3.

Table 1. 3 Graphite based electrochemical biosensors.

Material	Analyte	Sensitivity	Detection Limit	Benefits	Ref.
Graphite nanosheets	NADH (Nicotinamide Adenine Dinucleotide – Hydrogen)	535.0 mAM^{-1} cm^{-2}	2μM to 4.69mM	Oxidative peak potential decreased to 0.32V	[143]
Modified pyrolytic graphite	Adenine and adenosine monophosphate	677 and 476nAnM−1	5–100nM for adenine and 10–100nM for AMP	High stability and reproducibility	[137]
Exfoliated graphite	Bisphenol A	-	1.56 μM–50 μM	Reproducibility of sensor is good.	[138]
Graphite felt/prussion blue/Pt nanoparticle	Hydrogen peroxide	40.9 A cm-^{2}M-1	1.2 nM	Graphite felt enhance stability, surface area and reduce cost of	[139]

				sensor	
Screen printed carbon electrode/graphite/Au nanoparticles	Hydrazine	0.54 ± 0.08 µA/µM/cm2	0.57 ± 0.03 nM	Good sensitivity and stability.	[144]
Electrochemically modified graphite/screen printed carbon electrode	Nitrite	0.126 µA /µM/cm2	38 nM	Reproducibility and stability	[145]
Graphite/ polyurethane	Tetracycline's	0.02 µA /µM/ L	2.6µM	Low toxicity over wide potential window, low cost and reproducible.	[56]
Graphite paste electrode/phthalocyanine/gold nanoparticles	Cysteine	57.2 mA/mM/cm^2	50–1000 µM	Reduced charge transfer resistance improved sensitivity	[142]
Graphite-supported Pd nanoparticles	Nitrite	0.29 µA/µM/cm^2	71nM	Enhanced electrocatalytic behaviour for nitrite	[146]
Electrochemically treated pencil graphite	Chlorine	0.302 µA ppm^{-1} cm^{-2}	-	Low cost, easy to fabricate sensor	[141]

1.5.5 Hydrogen storage

Hydrogen storage constitutes an additional application of graphite-based materials. Hydrogen is a clean and green fuel, as it is pollution free. There is an urgent need to develop promising hydrogen storage methods and materials to enable the use of hydrogen as a replacement for fossil fuels. Different types of materials have been investigated for hydrogen storage, including metals, alloys, carbon nanostructures, etc. Requirements are safety, reversibility, and storage capacity. Porous graphite, expanded graphite, and graphite composites have been reported as effective hydrogen storage materials [33, 147].

Graphite may be modified to porous graphite by an acid treatment with the subsequent introduction of metal nanoparticles to form a nanocomposite [33]. As-prepared nanocomposites

showed excellent hydrogen storage behaviour, and could store 4.48 wt% of hydrogen, because of the enhanced interlayer distance of graphite that was induced by the acid treatment. The hydrogen storage capacity of the nanocomposites and porous graphite is illustrated in Figure 1.12.
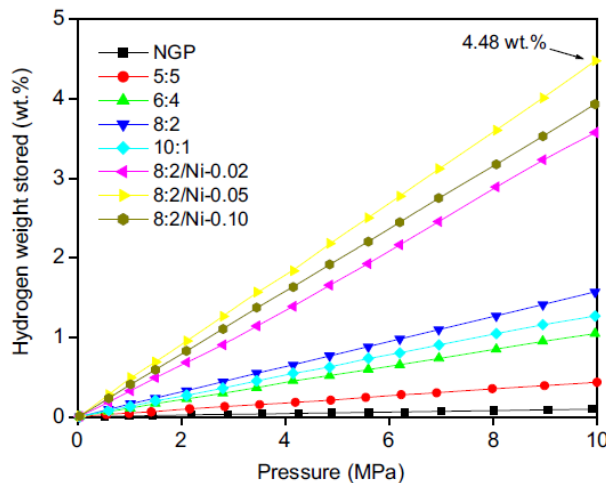
Figure 1.12 Hydrogen storage (in wt%) of porous graphite with varying Ni content. Adapted from ref [33]. Copyright 2011Elsevier.

Expanded graphite is synthesized via a two-step process, and acid intercalation is followed by thermal shock, after which it is decorated with TiO_2 nanoparticles to prepare the nanocomposite. This nanocomposite was observed to improve the electrochemical hydrogen storage behaviour. This material exhibited a 373.5 mAh/g discharge capacity which was attributed to the enhanced electrochemical activity of the expanded graphite by the TiO_2 nanoparticles [147]. Graphite-based materials have been studied for their capacity to store hydrogen by various methods, such as physisorption, electrochemical, etc.

1.5.6 Photoelectrochemical

Graphite-based materials have also been reported for photoelectrochemical applications such as pollutant treatment, dye-sensitized solar cells, photocatalysts, etc [59, 149-150]. Graphite's role is to enhance the activity and stability of the photoactive material, and it has been composited with light sensitive metal oxides such as TiO_2 [148]. Graphite facilitates charge

carrier separation and reduces recombination due to its high conductivity. An expanded graphite-TiO_2 nanocomposite, prepared by a sol-gel method, was reported for the photoelectrochemical degradation of nitrophenol (pollutant). It demonstrated more rapid and efficacious degradation compared to TiO_2 alone, and the degradation efficiency was improved from 29% to 96.3%.

T. Ndlovu et al. reported on an exfoliated graphite-TiO_2 nanocomposite for the degradation of the eosin yellow dye. The absorption and photodegradation of the dye on an exfoliated graphite-TiO_2 composite was compared with exfoliated graphite and commercial TiO_2 in Figure 1.13. This enhanced photoactivity was attributed to the capacity of graphite to receive and conduct photogenerated electrons [59].
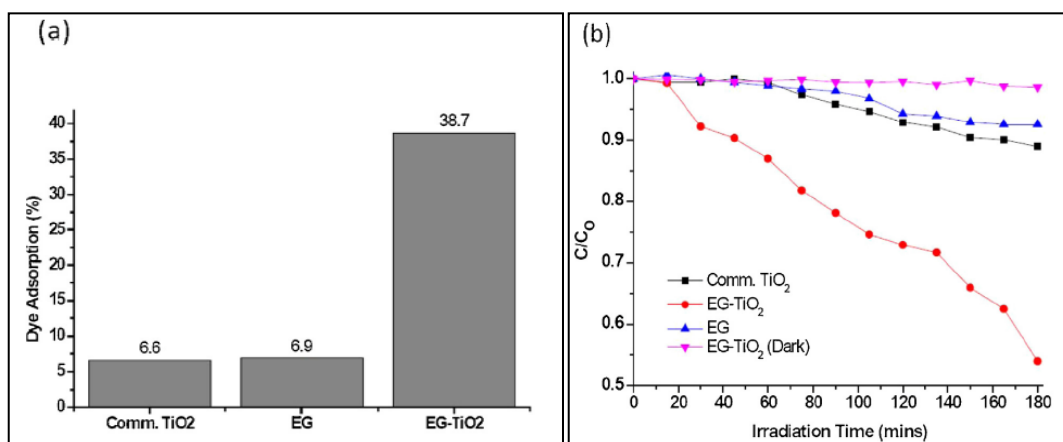
Figure 1.13 Comparison of exfoliated graphite (EG), commercial TiO_2 and EG-TiO_2 composite for (a) Eosin yellow dye adsorption %, and (b) Photodegradation of eosin yellow. Adapted from ref [59]. Copyright 2014 Elsevier.

Further, graphite was employed as an additive in an active material for a photoanode in a dye-sensitized solar cell. A graphite-TiO_2 composite was prepared by ultrasound mixing method, which showed that the addition of only 0.01% graphite enhanced the photocurrent and conversion efficiency of DSSC [149].

Y.Y. Li et al. investigated different graphite morphology as a counter electrode in dye-sensitized solar cells. Graphite nanofibers, graphite nanosheets, and graphite nanoballs comprised the three different structures that were compared. It was discovered that the graphite nanoball counter electrode improved the conversion efficiency of DSSC in contrast to the other two materials. The improved performance was attributed to the presence of additional defects and hydroxyl functionalities, which served to enhance the active sites. In addition, the performance of GNB was close to the commercial Pt counter electrode [150]. Graphite based materials were employed to develop composites for use in various photoelectrochemical applications, such as the photodegradation of pollutants, photocatalysts, and counter electrodes in dye-sensitized solar cells.

1.6   Scope of thesis

Graphite has numerous applications and scope for the development of novel advanced materials for electrochemical applications. The preparation of graphene from graphite is undergoing rapid and intense growth, and graphene oxide is a branch of graphene based materials. Graphene oxide derivatives are potential intermediates for the preparation of bulk graphene, and the functionalization of graphene oxide is an interesting modification for various electrochemical applications and the facile tuning of the properties of graphene oxide.

The scope of this thesis is to understand the properties of graphite provided by Zenyatta Ventures Ltd. and commercially available graphites. To analyze its influence on the preparation of graphene based materials. Firstly, graphite samples were characterized using various techniques, in order to understand properties such as morphology, crystallinity, thermal stability, surface area, defect density, oxygen content, etc. In the next project we prepared graphene oxide from four graphite samples and compared their characterization results. These results assisted with elucidating the abilities of the graphite. We then advanced to fluorine doping in graphene

oxide through a simple one-pot synthesis technique. An as-prepared fluorine doped graphene oxide was characterized to understand its properties and studied for two applications, namely, as an electrochemical capacitor and for heavy metal ion detection. As a whole, this thesis will be a model for systematic study to understand the properties of graphite toward the development of graphene based materials.

References

[1]   H.O. Pierson, Handbook of Carbon, Graphite, Diamond and Fullerenes, *Noyes Publications* **1993**.

[2]   D.W. Olson, Graphite (Natural), *US Geological Survey, Mineral Commodity Summaries* (**2015**) 68–69.

[3]   G.E. Bacon, Atomic Structure of Graphite and Graphitization, *Nature* 191 (**1961**) 27–28.

[4]   R. E. Kirk and D. F. Othmer, GRAPHITE , NATURAL, *Kirk-Othmer Encyclopedia of Chemical Technology* 5th Editio (**2004**) 771–799.

[5]   G.J. Simandl, S. Paradis, C. Akam, Graphite deposit types , their origin , and economic significance, *British Columbia Geological Survey Paper* 3 (**2015**) 163–171.

[6]   F.J. Luque, J.-M. Huizenga, E. Crespo-Feo, H. Wada, L. Ortega, J.F. Barrenechea, Vein graphite deposits: geological settings, origin, and economic significance, *Mineralium Deposita* 49 (**2014**) 261–277.

[7]   R. E. Kirk and D. F. Othmer, Graphite , Artificial, *Kirk-Othmer Encyclopedia of Chemical Technology* 5th Editio (**2004**) 713–771.

[8]   A. V Tamashausky, An Introduction to Synthetic Graphite, *Asbury Graphite* (**2006**) 1–12.

[9]   J. Pappis and S.L. Blum, Properties of Pyrolytic Graphite, *Journal of the American Ceramic Society* 474 (**1961**) 592–597.

[10]   J. L. F. Coffin, Structure- Property Relations for Pyrolytic Graphite, *Journal of the American Ceramic Society* 47 (**1964**) 473–478.

[11]   S. Liu, C.R. Loper, The formation of kish graphite, *Carbon* 29 (**1991**) 547–555.

[12]   T. Sri Devi Kumari, A.J.J. Jebaraj, T.A. Raj, D. Jeyakumar, T.P. Kumar, A kish graphitic lithium-insertion anode material obtained from non-biodegradable plastic waste, *Energy* 95 (**2016**) 483–493.

[13]   X.H. Chen, J.X. Wang, H.S. Yang, G.T. Wu, X.B. Zhang, W.Z. Li, Preparation, morphology and microstructure of segmented graphite nanofibers, *Diamond and Related Materials* 10 (**2001**) 2057–2062.

[14] Y. Geng, S.J. Wang, J.K. Kim, Preparation of graphite nanoplatelets and graphene sheets, *Journal of Colloid and Interface Science* 336 (**2009**) 592–598.

[15] S. Motozuka, M. Tagaya, N. Ogawa, K. Fukui, M. Nishikawa, K. Shiba, T. Uehara, T. Kobayashi, Effective preparation of graphite nanoparticles using mechanochemical solid-state reactions, *Solid State Communications* 190 (**2014**) 28–32.

[16] X. Yu, Preparation for Graphite Materials and Study on Electrochemical Degradation of Phenol by Graphite Cathodes, *Advances in Materials Physics and Chemistry* 2 (**2012**) 63–68.

[17] S. Kim, R. Sergiienko, E. Shibata, Y. Hayasaka, T. Nakamura, Production of Graphite Nanosheets by Low-Current Plasma Discharge in Liquid Ethanol, *Materials Transactions* 51 (**2010**) 1455–1459.

[18] V.I. Kleshch, E. a. Smolnikova, A.S. Orekhov, T. Kalvas, O. Tarvainen, J. Kauppinen, A. Nuottajärvi, H. Koivisto, P. Janhunen, A.N. Obraztsov, Nano-graphite cold cathodes for electric solar wind sail, *Carbon* 81 (**2015**) 132–136.

[19] T.H. Ko, S.C. Liau, M.F. Lin, Preparation of graphite fibres from a modified PAN precursor, *Journal of Materials Science* 27 (**1992**) 6071–6078.

[20] J.H. Kim, J. Lee, Processing Research Preparation of graphite nanosheets by combining microwave irradiation and liquid-phase exfoliation, *Journal of Ceramic Processing Research* 15 (**2014**) 341–346.

[21] O. V. Popova, M.Y. Serbinovskii, Graphite from hydrolysis lignin: Preparation procedure, structure, properties, and application, *Russian Journal of Applied Chemistry* 87 (**2014**) 818–823.

[22] G. Chen, W. Weng, D. Wu, C. Wu, J. Lu, P. Wang, X. Chen, Preparation and characterization of graphite nanosheets from ultrasonic powdering technique, *Carbon* 42 (**2004**) 753–759.

[23] C. Ma, Y. Zhao, J. Li, Y. Song, J. Shi, Q. Guo, L. Liu, Synthesis and electrochemical properties of artificial graphite as an anode for high-performance lithium-ion batteries, *Carbon* 64 (**2013**) 553–556.

[24] J.L. Cholula-Díaz, J. Barzola-Quiquia, H. Krautscheid, U. Teschner, P. Esquinazi, Synthesis and magnetotransport properties of nanocrystalline graphite prepared by aerosol assisted chemical vapor deposition, *Carbon* 67 (**2014**) 10–16.

[25] G. Sun, X. Li, Y. Qu, X. Wang, H. Yan, Y. Zhang, Preparation and characterization of graphite nanosheets from detonation technique, *Materials Letters* 62 (**2008**) 703–706.

[26] H. Panjiar, R.P. Gakkhar, B.S.S. Daniel, Strain-free graphite nanoparticle synthesis by mechanical milling, *Powder Technology* 275 (**2015**) 25–29.

[27] M.V. Antisari, a. Montone, N. Jovic, E. Piscopiello, C. Alvani, L. Pilloni, Low energy pure shear milling: A method for the preparation of graphite nano-sheets, *Scripta Materialia* 55 (**2006**) 1047–1050.

[28] X. Glad, L. De Poucques, J. a. Jaszczak, M. Belmahi, J. Ghanbaja, J. Bougdira, Plasma synthesis of hexagonal-pyramidal graphite hillocks, *Carbon* 76 (**2014**) 330–340.

[29] H.C.F. Burket, Christopher L, Rajagolapan, Ramakrishnan, Novel synthesis of nanoporous graphite, in: International Conference on Carbon, **2007**: pp. 1–4.

[30] A. Wang, J. Ren, B. Shi, G. Lu, Y. Wang, A facile one-pot synthesis of mesoporous graphite-like carbon through the organic-organic co-assembly, *Microporous and Mesoporous Materials* 151 (**2012**) 287–292.

[31] A.G. Sadekar, S.S. Mahadik, A.N. Bang, Z.J. Larimore, C. a. Wisner, M.F. Bertino, a. K. Kalkan, J.T. Mang, C. Sotiriou-Leventis, N. Leventis, From "Green" aerogels to porous graphite by emulsion gelation of acrylonitrile, *Chemistry of Materials* 24 (**2012**) 26–47.

[32] V.A. Karavanskii, N.N. Mel'nik, T.N. Zavaritskaya, Preparation and study of the optical properties of porous graphite, *Journal of Experimental and Theoretical Physics Letters* 74 (**2001**) 186–189.

[33] B.-J. Kim, S.-J. Park, Optimization of the pore structure of nickel/graphite hybrid materials for hydrogen storage, *International Journal of Hydrogen Energy* 36 (**2011**) 648–653.

[34] R.E.G. Smith, T.J. Davies, N.D.B. Baynes, R.J. Nichols, The electrochemical characterisation of graphite felts, *Journal of Electroanalytical Chemistry* 747 (**2015**) 29–38.

[35] Y. Wang, Y. Liu, K. Wang, S. Song, P. Tsiakaras, H. Liu, Preparation and characterization of a novel KOH activated graphite felt cathode for the electro-Fenton process, *Applied Catalysis B: Environmental* 165 (**2015**) 360–368.

[36] X. Wu, H. Xu, P. Xu, Y. Shen, L. Lu, J. Shi, J. Fu, H. Zhao, Microwave-treated graphite felt as the positive electrode for all-vanadium redox flow battery, *Journal of Power Sources* 263 (**2014**) 104–109.

[37] J.-H. Kim, E. Jeong, Y.-S. Lee, Preparation and characterization of graphite foams, *Journal of Industrial and Engineering Chemistry* 32 (**2015**) 21–33.

[38] L.I. Juan, W. Can, Z. Liang, Q. Wen-ming, L. Xiao-yi, L. Li-cheng, Preparation and performance of mesophase pitch based graphite foam, *Journal of Materials Science and Engineering* 2 (**2008**) 13–18.

[39] C.-F. Kuan, K.-C. Tsai, C.-H. Chen, H.-C. Kuan, T.-Y. Liu, C.-L. Chiang, Preparation of expandable graphite via H2O2-hydrothermal process and its effect on properties of high-density polyethylene composites, *Polymer Composites* 33 (**2012**) 872–880.

[40] Y.P. Chen, S.Y. Li, R.Y. Luo, X.M. Lu, X.J. Wang, Optimization of initial redox potential in the preparation of expandable graphite by chemical oxidation, *Xinxing Tan Cailiao/New Carbon Materials* 28 (**2013**) 435–441.

[41] N. Sykam, K.K. Kar, Rapid synthesis of exfoliated graphite by microwave irradiation and oil sorption studies, *Materials Letters* 117 (**2014**) 150–152.

[42] D.D.. Chung, Review Exfoliation of graphite, *Journal of Material Science* 22 (**1987**) 4190–4198.

[43] L. Wang, Y. Zhu, C. Guo, X. Zhu, J. Liang, Y. Qian, Ferric chloride-Graphite Intercalation Compounds as Anode Materials for Li-ion Batteries, *ChemSusChem* 7 (**2014**) 87–91.

[44] M.S. Dresselhaus, G. Dresselhaus, Intercalation compounds of graphite, *Advances in Physics* 51 (**2002**) 1–186.

[45] H. Park, M. Kim, F. Xu, C. Jung, S.M. Hong, C.M. Koo, In situ synchrotron wide-angle X-ray scattering study on rapid lithiation of graphite anode via direct contact method for Li-ion capacitors, *Journal of Power Sources* 283 (**2015**) 68–73.

[46] H. Fujimoto, A. Tressaud, Long-term stability of fluorine–graphite intercalation compound prepared under high pressure of fluorine, *Carbon* 82 (**2015**) 176–183.

[47] N.I. Kovtyukhova, Y. Wang, A. Berkdemir, R. Cruz-Silva, M. Terrones, V.H. Crespi, T.E. Mallouk, Non-oxidative intercalation and exfoliation of graphite by Brønsted acids., *Nature Chemistry* 6 (**2014**) 957–63.

[48] H.M.A. Asghar, S.N. Hussain, H. Sattar, N.W. Brown, E.P.L. Roberts, Electrochemically synthesized GIC-based adsorbents for water treatment through adsorption and electrochemical regeneration, *Journal of Industrial and Engineering Chemistry* 20 (**2013**) 2200–2207.

[49] S.R. Sivakkumar, A.G. Pandolfo, Evaluation of lithium-ion capacitors assembled with pre-lithiated graphite anode and activated carbon cathode, *Electrochimica Acta* 65 (**2012**) 280–287.

[50] J.-C. An, H.J. Kim, I. Hong, Preparation of Kish graphite-based graphene nanoplatelets by GIC (graphite intercalation compound) via process, *Journal of Industrial and Engineering Chemistry* 26 (**2015**) 55–60.

[51] J.M. Skowroński, T. Rozmanowski, P. Krawczyk, Enhancement of electrochemical hydrogen storage in NiCl2- FeCl3-PdCl2-graphite intercalation compound effected by chemical exfoliation, *Applied Surface Science* 275 (**2013**) 282–288.

[52] X. He, D. Hubble, R. Calzada, A. Ashtamkar, D. Bhatia, S. Cartagena, P. Mukherjee, H. Liang, A silver-nanoparticle-catalyzed graphite composite for electrochemical energy storage, *Journal of Power Sources* 275 (**2015**) 688–693.

[53] J.G. Kim, S.H. Nam, S.H. Lee, S.M. Choi, W.B. Kim, SnO(2) nanorod-planted graphite: an effective nanostructure configuration for reversible lithium ion storage., *ACS Applied Materials & Interfaces* 3 (**2011**) 828–835.

[54] W. Sun, R. Hu, H. Liu, M. Zeng, L. Yang, H. Wang, M. Zhu, Embedding nano-silicon in graphene nanosheets by plasma assisted milling for high capacity anode materials in lithium ion batteries, *Journal of Power Sources* 268 (**2014**) 610–618.

[55] A. Bai, L. Wang, J. Li, X. He, J. Wang, J. Wang, Composite of graphite/phosphorus as

anode for lithium-ion batteries, *Journal of Power Sources* 289 (**2015**) 100–104.

[56] C.M.F. Calixto, É.T.G. Cavalheiro, Determination of Tetracyclines in Bovine and Human Urine using a Graphite-Polyurethane Composite Electrode, *Analytical Letters* 48 (**2015**) 1454–1464.

[57] M. d'Halluin, T. Mabit, N. Fairley, V. Fernandez, M.B. Gawande, E. Le Grognec, F.-X. Felpin, Graphite-supported ultra-small copper nanoparticles – Preparation, characterization and catalysis applications, *Carbon* 93 (**2015**) 974–983.

[58] C. Du, P. Ming, M. Hou, J. Fu, Q. Shen, D. Liang, Y. Fu, X. Luo, Z. Shao, B. Yi, Preparation and properties of thin epoxy/compressed expanded graphite composite bipolar plates for proton exchange membrane fuel cells, *Journal of Power Sources* 195 (**2010**) 794–800.

[59] T. Ndlovu, A.T. Kuvarega, O. a. Arotiba, S. Sampath, R.W. Krause, B.B. Mamba, Exfoliated graphite/titanium dioxide nanocomposites for photodegradation of eosin yellow, *Applied Surface Science* 300 (**2014**) 159–164.

[60] J.R. Crespo-Rosa, C. Zanardi, M. Elkaoutit, F. Terzi, R. Seeber, I. Naranjo-Rodriguez, Electroanalytical applications of a graphite-Au nanoparticles composite included in a sonogel matrix, *Electrochimica Acta* 122 (**2014**) 310–315.

[61] J. Wang, E. Ou, J. Li, X. Yang, W. Wang, Z. Yan, C. Li, Synthesis of mesoporous titania-graphite composite templated by hypocrellins for visible-light photocatalytic degradation of acetaldehyde, *Materials Science in Semiconductor Processing* 31 (**2015**) 397–404.

[62] Y. Han, Q. Yan, X. Li, A simple way to prepare silicon carbide reinforced graphite composite lubricating materials, *Journal of Wuhan University of Technology-Mater Sci Ed* 30 (**2015**) 288–291.

[63] H. Tian, W. Wang, J. Ding, X. Wei, M. Song, J. Yang, Thermal conductivities and characteristics of ternary eutectic chloride/expanded graphite thermal energy storage composites, *Applied Energy* 148 (**2015**) 87–92.

[64] N. Sykam, R.K. Gautam, K.K. Kar, Electrical, mechanical, and thermal properties of exfoliated graphite/phenolic resin composite bipolar plate for polymer electrolyte membrane fuel cell, *Polymer Engineering & Science* 55 (**2015**) 917–923.

[65] N. Gedam, N.R. Neti, M. Kormunda, J. Subrt, S. Bakardjieva, Novel lead dioxide-graphite-polymer composite anode for electrochemical chlorine generation, *Electrochimica Acta* 169 (**2015**) 109–116.

[66] X. Xiao, P. Zhang, Z.-N. Meng, M. Li, Thermal Conductivity of Eutectic Nitrates and Nitrates/Expanded Graphite Composite as Phase Change Materials, *Journal of Nanoscience and Nanotechnology* 15 (**2015**) 3135–3142.

[67] X. Jiang, D.-X. Yan, Y. Bao, H. Pang, X. Ji, Z.-M. Li, Facile, green and affordable strategy for structuring natural graphite/polymer composite with efficient electromagnetic interference shielding, *RSC Advances* 5 (**2015**) 22587–22592.

[68]   A.K. Mishra, S. Ramaprabhu, Graphite Nanoplatelets/Multiwalled Carbon Nanotubes Hybrid Nanostructure for Electrochemical Capacitor, *Journal of Nanoscience and Nanotechnology* 12 (**2012**) 6658–6664.

[69]   Y. Jin, C.P. Huynh, S.C. Hawkins, S. Su, Expanded graphite/phenolic resin-based carbon composite adsorbents for post-combustion CO 2 capture, *RSC Advances* 5 (**2015**) 62604–62610.

[70]   P. Ramesh, S. Sampath, Electrochemical and spectroscopic characterization of quinone functionalized exfoliated graphite., *The Analyst* 126 (**2001**) 1872–1877.

[71]   S.G. Miller, J.L. Bauer, M.J. Maryanski, P.J. Heimann, J.P. Barlow, J.M. Gosau, R.E. Allred, Characterization of epoxy functionalized graphite nanoparticles and the physical properties of epoxy matrix nanocomposites, *Composites Science and Technology* 70 (**2010**) 1120–1125.

[72]   Y. Geng, J. Li, S.J. Wang, J.K. Kim, Amino Functionalization of Graphite Nanoplatelet, *Journal of Nanoscience and Nanotechnology* 8 (**2008**) 6238–6246.

[73]   Y.L. Zhong, T.M. Swager, Enhanced electrochemical expansion of graphite for in situ electrochemical functionalization, *Journal of the American Chemical Society* 134 (**2012**) 17896–17899.

[74]   P.L. Girard-Lauriault, R. Illgen, J.C. Ruiz, M.R. Wertheimer, W.E.S. Unger, Surface functionalization of graphite and carbon nanotubes by vacuum-ultraviolet photochemical reactions, *Applied Surface Science* 258 (**2012**) 8448–8454.

[75]   M. Collaud Coen, B. Keller, P. Groening, L. Schlapbach, Functionalization of graphite, glassy carbon, and polymer surfaces with highly oxidized sulfur species by plasma treatments, *Journal of Applied Physics* 92 (**2002**) 5077.

[76]   A. Carrillo, J. a. Swartz, J.M. Gamba, R.S. Kane, N. Chakrapani, B. Wei, P.M. Ajayan, Noncovalent Functionalization of Graphite and Carbon Nanotubes with Polymer Multilayers and Gold Nanoparticles, *Nano Letters* 3 (**2003**) 1437–1440.

[77]   B.C. Brodie, On the Atomic Weight of Graphite, *Philosophical Transactions of the Royal Society of London* 149 (**1859**) 249–259.

[78]   L. Staudenmaier, Verfahren zur Darstellung der Graphitsäure, *Berichte Der Deutschen Chemischen Gesellschaft* 31 (**1898**) 1481–1487.

[79]   J. William S. Hummers, R.E. Offeman, Preparation of Graphitic Oxide, *Journal of the American Chemical Society* 80 (**1958**) 1339.

[80]   D.C. Marcano, D. V. Kosynkin, J.M. Berlin, A. Sinitskii, Z. Sun, A. Slesarev, L.B. Alemany, W. Lu, J.M. Tour, Improved Synthesis of Graphene Oxide, *ACS Nano* 4 (**2010**) 4806–4814.

[81]   A. Lerf, H. He, M. Forster, J. Klinowski, Structure of Graphite Oxide Revisited, *Journal of Physical Chemistry B* 102 (**1998**) 4477–4482.

[82] N. Morimoto, T. Kubo, Y. Nishina, Tailoring the Oxygen Content of Graphite and Reduced Graphene Oxide for Specific Applications, *Scientific Reports* 6 (**2016**) 21715.

[83] M. Seredych, T.J. Bandosz, Removal of ammonia by graphite oxide via its intercalation and reactive adsorption, *Carbon* 45 (**2007**) 2130–2132.

[84] G. He, J. Zhang, Y. Zhang, H. Chen, X. Wang, Fast and Efficient Removal of Cationic Dye Using Graphite Oxide, Adsorption, and Kinetics Studies, *Journal of Dispersion Science and Technology* 34 (**2013**) 1223–1229.

[85] A.K. Geim, K.S. Novoselov, The rise of graphene., *Nature Materials* 6 (**2007**) 183–191.

[86] A.K. Geim, Graphene: Status and Prospects, *Science* 324 (**2009**) 1530–1534.

[87] K. Coleman, R.S. Edwards, Graphene synthesis: Relationship to applications, *Nanoscale* (**2012**) 38–51.

[88] S. Park, R.S. Ruoff, Chemical methods for the production of graphenes., *Nature Nanotechnology* 4 (**2009**) 217–224.

[89] K.E. Whitener, P.E. Sheehan, Graphene synthesis, *Diamond and Related Materials* 46 (**2014**) 25–34.

[90] K.S. Novoselov, Nobel Lecture: Graphene: Materials in the Flatland, *Reviews of Modern Physics* 83 (**2011**) 837–849.

[91] W. Gao, L.B. Alemany, L. Ci, P.M. Ajayan, New insights into the structure and reduction of graphite oxide., *Nature Chemistry* 1 (**2009**) 403–408.

[92] A. Ciesielski, P. Samorì, Graphene via sonication assisted liquid-phase exfoliation., *Chemical Society Reviews* 43 (**2014**) 381–98.

[93] A.M. Abdelkader, A.J. Cooper, R.A.W. Dryfe, I.A. Kinloch, How to get between the sheets: a review of recent works on the electrochemical exfoliation of graphene materials from bulk graphite, *Nanoscale* 7 (**2015**) 6944–6956.

[94] D.K. Dang, E.J. Kim, Solvothermal-assisted liquid-phase exfoliation of graphite in a mixed solvent of toluene and oleylamine, *Nanoscale Research Letters* 10 (**2015**) 4–11.

[95] D. Chen, H. Feng, J. Li, Graphene oxide: Preparation, functionalization, and electrochemical applications, *Chemical Reviews* 112 (**2012**) 6027–6053.

[96] H.L. Poh, F. Šaněk, A. Ambrosi, G. Zhao, Z. Sofer, M. Pumera, Graphenes prepared by Staudenmaier, Hofmann and Hummers methods with consequent thermal exfoliation exhibit very different electrochemical properties, *Nanoscale* 4 (**2012**) 3515.

[97] Y. Zhu, S. Murali, M.D. Stoller, A. Velamakanni, R.D. Piner, R.S. Ruoff, Microwave assisted exfoliation and reduction of graphite oxide for ultracapacitors, *Carbon* 48 (**2010**) 2118–2122.

[98] S. Pei, H.M. Cheng, The reduction of graphene oxide, *Carbon* 50 (**2012**) 3210–3228.

[99] A. Ambrosi, M. Pumera, Precise tuning of surface composition and electron-transfer properties of graphene oxide films through electroreduction, *Chemistry - A European Journal* 19 (**2013**) 4748–4753.

[100] L. Peng, Z. Xu, Z. Liu, Y. Wei, H. Sun, Z. Li, X. Zhao, C. Gao, An iron-based green approach to 1-h production of single-layer graphene oxide, *Nature Communications* 6 (**2015**) 5716.

[101] H. Yang, H. Li, J. Zhai, L. Sun, H. Yu, Simple Synthesis of Graphene Oxide Using Ultrasonic Cleaner from Expanded Graphite, *Industrial & Engineering Chemistry Research* 53 (**2014**) 17878–17883.

[102] S. Eigler, Controlled Chemistry Approach to the Oxo-Functionalization of Graphene, *Chemistry - A European Journal* 22 (**2016**) 7012–7027.

[103] N. Morimoto, T. Kubo, Y. Nishina, Tailoring the Oxygen Content of Graphite and Reduced Graphene Oxide for Specific Applications, *Scientific Reports* 6 (**2016**) 21715.

[104] D.-W. Kang, H.-S. Shin, Control of size and physical properties of graphene oxide by changing the oxidation temperature, *Carbon Letters* 13 (**2012**) 39–43.

[105] K. Kakaei, A. Balavandi, Synthesis of halogen-doped reduced graphene oxide nanosheets as highly efficient metal-free electrocatalyst for oxygen reduction reaction, *Journal of Colloid and Interface Science* 463 (**2015**) 46–54.

[106] Z. Wang, J. Wang, Z. Li, P. Gong, X. Liu, L. Zhang, J. Ren, H. Wang, S. Yang, Synthesis of fluorinated graphene with tunable degree of fluorination, *Carbon* 50 (**2012**) 5403–5410.

[107] L. Wang, Z. Sofer, R. Zboril, K. Cepe, M. Pumera, Phosphorus and Halogen Co-Doped Graphene Materials and their Electrochemistry, *Chemistry - A European Journal* 22 (**2016**) 15444–15450.

[108] O. Jankovský, P. Šimek, K. Klimová, D. Sedmidubský, S. Matějková, M. Pumera, Z. Sofer, Towards graphene bromide: bromination of graphite oxide, *Nanoscale* 6 (**2014**) 6065–6074.

[109] K. Kakaei, A. Balavandi, Synthesis of halogen-doped reduced graphene oxide nanosheets as highly efficient metal-free electrocatalyst for oxygen reduction reaction, *Journal of Colloid and Interface Science* 463 (**2016**) 46–54.

[110] F.-G. Zhao, G. Zhao, X.-H. Liu, C.-W. Ge, J.-T. Wang, B.-L. Li, Q.-G. Wang, W.-S. Li, Q.-Y. Chen, Fluorinated graphene: facile solution preparation and tailorable properties by fluorine-content tuning, *Journal of Materials Chemistry A* 2 (**2014**) 8782.

[111] S. Bag, B. Mondal, A.K. Das, C.R. Raj, Nitrogen and sulfur dual-doped reduced graphene oxide: Synergistic effect of dopants towards oxygen reduction reaction, *Electrochimica Acta* 163 (**2015**) 16–23.

[112] H. Cui, Z. Zhou, D. Jia, Heteroatom-doped graphene as electrocatalysts for air cathodes, *Materials Horizons* (**2017**).

[113] J. Duan, S. Chen, M. Jaroniec, S.Z. Qiao, Heteroatom-Doped Graphene-Based Materials for Energy-Relevant Electrocatalytic Processes, *ACS Catalysis* 5 (**2015**) 5207–5234.

[114] Y. Gong, H. Fei, X. Zou, W. Zhou, S. Yang, G. Ye, Z. Liu, Z. Peng, J. Lou, R. Vajtai, B.I. Yakobson, J.M. Tour, P.M. Ajayan, Boron- and nitrogen-substituted graphene nanoribbons as efficient catalysts for oxygen reduction reaction, *Chemistry of Materials* 27 (**2015**) 1181–1186.

[115] F.-X. Ma, J. Wang, F.-B. Wang, X.-H. Xia, The room temperature electrochemical synthesis of N-doped graphene and its electrocatalytic activity for oxygen reduction, *Chemical Communications* 51 (**2015**) 1198–1201.

[116] Z. Lin, G. Waller, Y. Liu, M. Liu, C.P. Wong, Facile synthesis of nitrogen-doped graphene via pyrolysis of graphene oxide and urea, and its electrocatalytic activity toward the oxygen-reduction reaction, *Advanced Energy Materials* 2 (**2012**) 884–888.

[117] H.-C. Youn, S.-M. Bak, M.-S. Kim, C. Jaye, D. a. Fischer, C.-W. Lee, X.-Q. Yang, K.C. Roh, K.-B. Kim, High-Surface-Area Nitrogen-Doped Reduced Graphene Oxide for Electric Double-Layer Capacitors, *ChemSusChem* 8 (**2015**) 1875–1884.

[118] H. Xing, J. Xu, X. Zhu, X. Duan, L. Lu, W. Wang, Y. Zhang, T. Yang, Highly sensitive simultaneous determination of cadmium (II), lead (II), copper (II), and mercury (II) ions on N-doped graphene modified electrode, *Journal of Electroanalytical Chemistry* 760 (**2016**) 52–58.

[119] Y. Qu, Y. Gao, L. Wang, J. Rao, G. Yin, Mild Synthesis of Pt/SnO2/Graphene Nanocomposites with Remarkably Enhanced Ethanol Electro-oxidation Activity and Durability, *Chemistry - A European Journal* 22 (**2016**) 193–198.

[120] E. Umeshbabu, G. Ranga Rao, A Vanadium(V) Oxide Nanorod Promoted Platinum/Reduced Graphene Oxide Electrocatalyst for Alcohol Oxidation under Acidic Conditions, *ChemPhysChem* 17 (**2016**) 3524–3534.

[121] G.H. Moon, Y. Park, W. Kim, W. Choi, Photochemical loading of metal nanoparticles on reduced graphene oxide sheets using phosphotungstate, *Carbon* 49 (**2011**) 3454–3462.

[122] G. Chen, F. Wang, F. Liu, X. Zhang, One-pot preparation of Ni-graphene hybrids with enhanced catalytic performance, *Applied Surface Science* 316 (**2014**) 568–574.

[123] S.X. Guo, Y.P. Liu, a M. Bond, J. Zhang, P.E. Karthik, I. Maheshwaran, S.S. Kumar, K.L.N. Phani, Facile electrochemical co-deposition of a graphene-cobalt nanocomposite for highly efficient water oxidation in alkaline media: direct detection of underlying electron transfer reactions under catalytic turnover conditions, *Physical Chemistry Chemical Physics* 16 (**2014**) 19035–19045.

[124] Z.-S. Wu, G. Zhou, L.-C. Yin, W. Ren, F. Li, H.-M. Cheng, Graphene/metal oxide composite electrode materials for energy storage, *Nano Energy* 1 (**2012**) 107–131.

[125] Q. Cheng, R. Yuge, K. Nakahara, N. Tamura, S. Miyamoto, KOH etched graphite for fast chargeable lithium-ion batteries, *Journal of Power Sources* 284 (**2015**) 258–263.

[126] Z. Chen, P. Lu, H. Zhu, B. Du, T. Xie, W. Wang, M. Xu, AC impedance investigation and charge-discharge performance of NaOH surface-modified natural graphite, *Electrochimica Acta* 102 (**2013**) 44–50.

[127] K. Meng, H. Guo, Z. Wang, X. Li, M. Su, B. Huang, Q. Hu, W. Peng, Self-assembly of porous-graphite/silicon/carbon composites for lithium-ion batteries, *Powder Technology* 254 (**2014**) 403–406.

[128] H.S. Kim, Electrochemical properties of graphite-based electrodes for redox flow batteries, *Bulletin of the Korean Chemical Society* 32 (**2011**) 571–575.

[129] A. Di Blasi, O. Di Blasi, N. Briguglio, a. S. Aricò, D. Sebastián, M.J. Lázaro, G. Monforte, V. Antonucci, Investigation of several graphite-based electrodes for vanadium redox flow cell, *Journal of Power Sources* 227 (**2013**) 15–23.

[130] J.-Z. Chen, W.-Y. Liao, W.-Y. Hsieh, C.-C. Hsu, Y.-S. Chen, All-vanadium redox flow batteries with graphite felt electrodes treated by atmospheric pressure plasma jets, *Journal of Power Sources* 274 (**2015**) 894–898.

[131] A.K. Mishra, S. Ramaprabhu, Graphite Nanoplatelets/Multiwalled Carbon Nanotubes Hybrid Nanostructure for Electrochemical Capacitor, *Journal of Nanoscience and Nanotechnology* 12 (**2012**) 6658–6664.

[132] S.S. Jyothirmayee Aravind, K. Ramanujachary, A. Mugweru, T.D. Vaden, Molybdenum phosphide-graphite nanomaterials for efficient electrocatalytic hydrogen production, *Applied Catalysis A: General* 490 (**2015**) 101–107.

[133] M. Yuan, W. Liu, Y. Zhu, Y. Xu, Electrochemical performance of pre-lithiated graphite as negative electrode in lithium-ion capacitors, *Russian Journal of Electrochemistry* 48 (**2014**) 1–8.

[134] C.M. Park, Y.N. Jo, J.W. Park, J. Yu, J.-S. Kim, J. Choi, Y. Kim, Anodic Performances of Surface-Treated Natural Graphite for Lithium Ion Capacitors, *Bulletin of the Korean Chemical Society* 35 (**2014**) 2630–2634.

[135] M. Wang, F. Xu, H. Sun, Q. Liu, K. Artyushkova, E. a. Stach, J. Xie, Nanoscale graphite-supported Pt catalysts for oxygen reduction reactions in fuel cells, *Electrochimica Acta* 56 (**2011**) 2566–2573.

[136] A. Döner, E. Telli, G. Kardaş, Electrocatalysis of Ni-promoted Cd coated graphite toward methanol oxidation in alkaline medium, *Journal of Power Sources* 205 (**2012**) 71–79.

[137] R.N. Goyal, S. Chatterjee, a. R.S. Rana, H. Chasta, Application of modified pyrolytic graphite electrode as a sensor in the simultaneous assay of adenine and adenosine monophosphate, *Sensors and Actuators, B: Chemical* 156 (**2011**) 198–203.

[138] T. Ndlovu, O.A. Arotiba, S. Sampath, R.W. Krause, B.B. Mamba, An Exfoliated Graphite-Based Bisphenol A Electrochemical Sensor, *Sensors* 12 (**2012**) 11601–11611.

[139] L. Han, S. Tricard, J. Fang, J. Zhao, W. Shen, Prussian blue @ platinum nanoparticles/graphite felt nanocomposite electrodes: application as hydrogen peroxide

sensor., *Biosensors & Bioelectronics* 43 (**2013**) 120–4.

[140] M. Lu, R.G. Compton, Voltammetric pH sensor based on an edge plane pyrolytic graphite electrode., *The Analyst* 139 (**2014**) 2397–403.

[141] S. Pan, M.J. Deen, R. Ghosh, Low-Cost Graphite-Based Free Chlorine Sensor, *Analytical Chemistry* 87 (**2015**) 10734–10737.

[142] M.N. Abbas, A.A. Saeed, B. Singh, A.A. Radowan, E. Dempsey, A cysteine sensor based on a gold nanoparticle–iron phthalocyanine modified graphite paste electrode, *Anal Methods* 7 (**2015**) 2529–2536.

[143] J. Zhu, X. Chen, W. Yang, A high performance electrochemical sensor for NADH based on graphite nanosheet modified electrode, *Sensors and Actuators, B: Chemical* 150 (**2010**) 564–568.

[144] C. Karuppiah, S. Palanisamy, S.M. Chen, S.K. Ramaraj, P. Periakaruppan, A novel and sensitive amperometric hydrazine sensor based on gold nanoparticles decorated graphite nanosheets modified screen printed carbon electrode, *Electrochimica Acta* 139 (**2014**) 157–164.

[145] S. Palanisamy, C. Karuppiah, S.-M. Chen, P. Periakaruppan, Highly sensitive and selective amperometric nitrite sensor based on electrochemically activated graphite modified screen printed carbon electrode, *Journal of Electroanalytical Chemistry* 727 (**2014**) 34–38.

[146] J.-H. Yang, H. Yang, S. Liu, L. Mao, Microwave-assisted synthesis graphite-supported Pd nanoparticles for detection of nitrite, *Sensors and Actuators B: Chemical* 220 (**2015**) 652–658.

[147] Y. Yu, N. Zhao, C. Shi, C. He, E. Liu, J. Li, Electrochemical hydrogen storage of expanded graphite decorated with TiO_2 nanoparticles, *International Journal of Hydrogen Energy* 37 (**2012**) 5762–5768.

[148] X. Yu, Y. Zhang, X. Cheng, Preparation and photoelectrochemical performance of expanded graphite/TiO2 composite, *Electrochimica Acta* 137 (**2014**) 668–675.

[149] X. Hu, K. Huang, D. Fang, S. Liu, Enhanced performances of dye-sensitized solar cells based on graphite-TiO2 composites, *Materials Science and Engineering B: Solid-State Materials for Advanced Technology* 176 (**2011**) 431–435.

[150] Y.-Y. Li, C.-T. Li, M.-H. Yeh, K.-C. Huang, P.-W. Chen, R. Vittal, K.-C. Ho, Graphite with Different Structures as Catalysts for Counter Electrodes in Dye-sensitized Solar Cells, *Electrochimica Acta* 179 (**2015**) 211–219.

Chapter II

Materials and methods

2.1   Introduction

Graphite based nanomaterials possess enormous potential for various applications such as electrochemical sensors, catalyst supports, metal free catalysts, and more. The scope and objective of this thesis is summarized in the previous chapter along with a literature review. The materials used in this work are mentioned, and the methods employed are discussed. Methods, principles, and purpose of the techniques used will be described in this chapter, with specific details to be articulated in the respective chapters.

2.2   Materials

Graphite samples provided by Zenyatta Ventures Ltd. (ZEN 378 and ZEN 915), graphite powder (Aldrich 99.999%, -325mesh (product # 496596, batch #04612TB)), graphite powder Alfa Aesar (99%, -325mesh (product # 10129, lot #G01Z068)) were used as the raw materials for this project.

Reagents used for synthesis were sulfuric acid (98% Aldrich), phosphoric acid (85%, Ffisher Scientific), potassium permanganate (≥99.0%, Caledon), hydrofluoric acid (50% Sigma-Aldrich product # 7664-39-3).

Reagents used for the electrochemical experiments, including potassium chloride (99.0-100.5%), potassium ferricyanide (99+% ACS reagent), sodium dihydrogen phosphate (≥99.0%), sodium mono hydrogen phosphate (≥99.0%), acetic acid (≥99.7% Anachemia), and sodium acetate (≥99.0%, EMD), were used as received from Sigma Aldrich without treatment. CopperII nitrate trihydrate (99.0-104.0%), mercuryII nitrate monohydrate (≥98.5%, ACS reagent), leadII nitrate (≥99.0%, ACS Reagent), and cadmiumII nitrate tetrahydrate (98%, B.D.H), were used as

received from Sigma Aldrich without further purification. Pure water (18 MΩ cm) was obtained from a Nanopure® Diamond^{TM} UV ultrapure water purification system and used for dilutions and in the preparation of solutions.

2.3   Instrumentation & methods

A hotplate with temperature controller (Chemglass) and centrifuge (Thermo electron Co., sorvall biofuge stratos centrifuge) were used for the synthesis and purification of the graphene derivatives.

Morphological studies were conducted using a scanning electron microscope (SEM, Hitachi SU-70), transmission electron microscope (TEM, JOEL 2010), and atomic force microscope (AFM, Picoscan 2100). Spectroscopic studies conducted in this context included X-ray diffraction (XRD), Fourier transform infrared spectroscopy (FTIR), Raman microscopy, and X-ray photoelectron spectroscopy (XPS). All electrochemical experiments were conducted using a CHI 660E electrochemical workstation and the methods employed were cyclic voltammetry (CV), electrochemical impedance spectroscopy, galvanostatic charging/discharging, and square wave voltammetry (SWV).

2.4   Microscopy

2.4.1 Scanning electron microscopy

Principle: An electron beam from a source is accelerated and collimated to sample surface. As a result of the bombardment of the incident beam, the sample releases secondary and backscattered electrons, where the released electrons contain information about the sample. By capturing the electrons emitted from the sample a SEM image is formed. In addition, the back scattered electrons from the sample are used for X-Ray analysis to elucidate the approximate composition of the material [1].

Purpose: Information related to the surface morphology, particle size, shape, and distribution may be interpreted from the SEM image, and when combined with X-ray analysis yields the elemental composition. SEM images may provide data as to the orientation of graphite sheets and average particle dimensions. Based on the thickness of the sheets that are present, the exfoliation of graphite can be confirmed [2].

Sample: SEM samples of a powder material may be prepared as follows. A tiny portion of material is dispersed in a suitable solvent and ultrasonicated. The as-prepared dispersion is then coated onto a cleaned silicon wafer and dried at room temperature.

2.4.2 Transmission electron microscopy

Principle: The fundamental principle in a TEM is similar to SEM except that in this case the electron beam transmitted through the specimen is used to form high resolution images. The accelerating voltage is higher compared to SEM technique, and X-rays generated from the sample are analyzed to produce a diffraction pattern which is a fingerprint of the specimen's crystal structure [1].

Purpose: TEM is capable of generating high resolution images that facilitate the elucidation of the shape, size (flake length, flake width) and morphology of a given material. High resolution and magnification may be achieved due to the high energy electron beam. This technique can impart data that makes even atomic level visualization possible. From TEM images, the edges of graphene layers can be clearly discerned. The number of graphene layers can be determined by counting the edges in one flake. Furthermore, it is useful for the determination of the aspect ratios (lateral size/thickness). It is also very useful for the generation of statistical data on the number of layers. Using TEM data one can calculate the fraction of monolayers using (number

of monolayers/total number of flakes). The selected area electron diffraction (SAED) pattern conveys information on the crystallographic attributes of the sample [2].

Sample: The sample preparation for TEM proceeds as follows: a thin dispersion of the sample is coated on to a carbon coated grid and then dried. The limitation of SEM and TEM techniques is that the use of high energy electron beams may interact with the sample and cause issues.

2.4.3 Atomic force microscopy

Principle: AFM generates a 3D profile of the sample by measuring the force between the AFM probe and the sample. The AFM probe is accurate enough to sense atomic scale (0.2 to 10 nm) thicknesses. With respect to the sample topography, the tip deflects toward or away from the surface. This is captured by a laser beam reflection to generate the image of the surface features of the specimen. AFM technique that can generate three dimensional topographic images of specimens [1].

Purpose: The AFM technique is useful in determining the thickness and number of graphene layers, and it generates three dimensional images from which the thickness of layers may be quantified, as well as the size of the layer, at atomic scale resolution. The limitations of this technique include expensive instrumentation and high sensitivity to the surroundings (vibrations, etc.). AFM images depict a wrinkle-like appearance of graphene, which may be attributed to the functional groups that are present in graphene, or the space created due to the evaporation of the intercalant. The thickness of the monolayer graphene sheet is ≈1 nm [3].

Sample: The material to be analyzed is dispersed and coated on to a silicon substrate and dried at room temperature. The dispersion of the material is diluted to lower concentrations to obtain higher quality images.

2.5 Spectroscopy

2.5.1 UV visible spectroscopy

Principle: For this technique the absorbance of the material is recorded by irradiating the specimen in the range of UV-visible/near infrared wavelengths (200-800 nm) range.

Purpose: From the absorbance data the band gap energy of the material can be quantified using the Tauc equation. It is useful to differentiate between graphene and graphene oxide. Graphene exhibits absorbance at 270 nm, which corresponds to C-C bond's π / π* transition, whereas for graphene oxide, the characteristic peak is observed at 230 nm. This technique is also useful for determining the concentration of unknown graphene dispersions. The concentration may be learned using the Lambert-Beer law by determining the absorbance coefficient using known concentration solutions [3].

Sample: A uniform low concentration dispersion of the material is prepared in suitable solvents.

2.5.2 X-ray diffraction

Principle: For this technique, X-rays are employed to analyze the crystal structure of the materials as their wavelength is similar to interatomic distances. The particle size of the material plays a significant role as X-rays cannot produce a good diffractogram for larger particles. X rays are typically generated using a Cu metal target with a 0.154 nm wavelength (Cu Kα). Incident X-rays on a sample will scatter in all directions; thesee are subsequently collimated and directed to a detector. Constructive interference of incident X-rays with the sample's atomic arrangement resulting in the generation of a peak in the diffractogram. Single crystal XRD is used for highly crystalline materials, whereas powder XRD is used for polycrystalline materials [2,4].

Purpose: XRD is utilized to confirm the structure and crystallinity of a material. In a diffractogram, narrow and sharp peaks are obtained for highly crystalline materials. A full width

half maximum (FWHM) of the peak corresponds to the average crystallite size that is wider for the smaller crystallite size. From the FWHM one can determine the average crystallite size using the Scherer equation. Further, in graphitic materials interlayer distances may also be determined using Bragg's law which is related to the peak position 2Θ [3].

Sample: Powders may be used for XRD without any processing.

2.5.3 Raman spectroscopy

Principle: The principle behind Raman spectroscopy is Raman scattering. Raman scattering may be defined as the small fraction of scattered radiation that has less frequency than the incident radiation due to its interactions with the vibrating molecules in the substance. The sample is irradiated with a monochromatic laser and the scattered radiation from the sample is analyzed. A 514 nm laser, as monochromatic laser source, was used to investigate the material structures in this work. Raman shifts offer useful information on vibrational, rotational, and other changes in the microstructure of a material [1].

Purpose: Raman scattering is highly sensitive to the electronic structure of carbon based materials, particularly for the changes of the C-C, C=C, edges, defects, and the randomness of carbon. It may also provide information on formation of graphene, the destruction of the graphitic structure, and functionalization. Moreover, based on the peak position and shape, the number of layers within graphene derivatives may be determined. Raman peak intensities may also be used to calculate the lateral dimensions of graphite-based materials [5,6].

Sample: For Raman microscopy the sample is prepared on a glass slide. The material is dispersed in water/ethanol, coated on the glass slide, and then allowed to dry at room temperature.

2.5.4 Fourier transform infrared spectroscopy

Principle: In FT-IR spectroscopy, a broad band of infrared radiation from an IR source transits to an interferometer, which applies Fourier transform to the incident IR radiation and then passes through the specimen. Transmitted radiation from the sample is subsequently analyzed in a cryogenic detector (liquid nitrogen cooled MCT (mercury cadmium telluride) detector). The absorption of IR depends on various functional groups and molecules that are present in the sample at different frequencies.

Purpose: FTIR is primarily used to investigate functional groups in organic chemistry. FTIR reveals the characteristic peaks for different functional groups using the different absorbance frequencies of the IR radiation, which is due to the stretching and bending vibration of the bonds within it. Each functional group has a specific frequency of IR absorption. This technique is useful in confirming functionalization and identifying functional groups that are present in graphene derivatives [7].

Sample: For this study KBr was employed as a beam splitter in the interferometer. A small portion of material is combined with KBr powder and mixed using a mortar until a homogenous mixture is obtained. A pinch of this mixture is compressed via a die to make a transparent pellet, which is used as the sample.

2.5.5 X-ray photoelectron spectroscopy

Principle: X-rays are used to emit electrons from the core atomic level of a sample. High energy X-ray photons interact with the sample which releases core atomic level electrons from its initial state with different kinetic energies. The kinetic energy and intensity of electrons are used to analyze the binding energy of the electron to the atom. The binding energies of electrons are different for each atom under different oxidation states; the X-ray sources used are Al Kα or Mg

Kα. The energy of the X-rays is between 200-2000eV. XPS is a powerful technique that may provide a rapid response with a relatively small quantity of sample required. However, this technique is expensive due to the ultrahigh vacuum that is required for precise analysis.

Purpose: The XPS technique is employed to elucidate the surface composition and oxidation states of a material, and is useful for determining the C/O ratio. XPS data is also useful as it can quantify the composition of functional groups. In this work it was used to analyze the composition of the various prepared graphene derivatives [8].

Sample preparation: Powdered samples for XPS may be prepared either by sprinkling the powder on carbon tape, or by compressing the powder to form a thin film.

2.6 Thermal analysis

Principle: For this technique a known weight of sample is heated at constant rate in an inert/air environment, wherein the weight and energy loss/gain is monitored. While being heated, the sample either releases heat (exothermic) or absorbs heat (endothermic). The energy loss/gain is associated with the weight loss of the sample. In addition, chemical changes associated with mass change may also be interpreted from this information.

Purpose: The weight loss of a material indicates its state of decomposition. The temperature at which point a major weight loss occurs is referred to as the decomposition point; that is, the material is structurally stable up to that temperature. Initially, a minor weight loss may occur due to the impurities or residual moisture that is present in the material. Hence, this analysis assists with understanding the thermal stability of the prepared materials, as well as to characterize the starting material [9].

Sample: No preparation is required for thermal analysis; the sample powder is sufficient for conducting the analysis. However, the sample cannot be aggregated and must be in a uniform powdery form, as large surface area exposure will yield better results.

2.7 BET surface area

Principle: The physical adsorption of gases is the basic principle of this method. Gases without any external trigger may adsorb onto surfaces. The basic assumption of this method is that there is no interaction with the material. The sample is subjected to liquid nitrogen adsorption, and by using the adsorption volume and specific surface area, the pore volume and pore size distribution may be determined.

Purpose: This method is used to analyze the surface area of graphite and graphite derivatives. The surface area of the material is related to its performance [10].

Sample: The Sample is required to be dry and free from moisture in order to obtain accurate and reproducible results. In this work, the samples were dried in an oven at a constant temperature (150-300°C) before subjecting them to surface area analysis.

2.8 Electrochemical techniques

The fundamental principle of the basic electrochemical techniques used in this project are discussed in this section.

2.8.1 *Electrochemical Cell*

In this work, a three electrode cell was used for all electrochemistry measurements. An Ag/AgCl in saturated KCl and Pt foil were used as the reference and counter electrode, respectively. The Pt foil was flame annealed until red hot and quenched immediately in water prior to every experiment in order to prevent any sources of contamination. The electrolyte employed was dependent upon the study, where KCl, H_2SO_4, phosphate buffer, and acetate

buffer were employed for different experiments. The working electrode was prepared using the material under study and was specific to the study, which is explained in the corresponding chapters.

2.8.2 *Electrode preparation*

The GCE was polished with 0.05 μm alumina until a mirror finish was achieved, and then sonicated in water for 3 minutes prior to each modification. A known weight of the material was dispersed in water or ethanol, and 0.1% Nafion was used as a binder, unless specifically mentioned. The dispersion was then sonicated for 30 minutes, after which 3-5 μL of the sample was drop casted onto the well-polished GCE and allowed to dry at room temperature. Electrode preparation method may e with respect to the samples, changes will be discussed in the corresponding chapters.

2.8.3 *Cyclic voltammetry*

The electrochemical activity of any material may be gauged by performing cyclic voltammetry, which is one of the potential sweep techniques. In this method, the potential of the working electrode is increased from one potential to another, and then back to the initial potential at a constant rate, and the current response is recorded. The electrochemical activity may be interpreted from the current response.

2.8.4 *Electrochemical impedance spectroscopy*

In this technique, the electrochemical cell is perturbed with a small AC signal, which is scanned over a defined frequency range. Prior to this; the working electrode is maintained at a constant DC potential to maintain a steady state. In this work, a faradaic impedance method was used to gauge the resistance of the materials. Potassium ferricyanide was employed as the redox

couple, and equilibrium was established by holding the potential at $E_{0.5}$ or open circuit potential (OCP), where $E_{0.5}$ was defined as the average reduction and oxidation peak potentials.

2.8.5 *Specific capacitance*

In this technique, the specific capacitance of the electrode is determined by conducting charge/discharge studies in galvanostatic mode. In this mode constant current can be applied to or drawn from a working electrode of electrochemical cell. The working electrode is imposed with a constant current until it attains a defined maximum potential. Subsequently, it is subjected to discharge by drawing the same current until defined minimum potential is attained, and the duration required for charging and discharging is recorded. Usually potential range for capacitance studies is 0 to 1.0 V. Using this technique, the specific capacitance and stability of the electrode at different current rates may be determined. The specific capacitance may be calculated using the equation **2.1** [11].

$$C = \frac{I\Delta t}{m\Delta V}$$ …………………………………………………**2.1**

where *I*=discharge current (A); *Δt*=discharge duration (s); *m*=mass of material in working electrode (g); *ΔV*= voltage window (end voltage - beginning voltage) (V); and *C* = capacitance in Farads/gram

2.8.6 *Heavy metal ion sensing*

Heavy metal ion sensing activity may be determined via three steps. The initial step involves the deposition of the heavy metals from solution, and is referred to as the adsorption step. In the second step, the deposited metal ions are stripped from the electrode surface. Square wave anodic stripping voltammetry (SWASV) is commonly used to eliminate capacitive signals and to maximize faradaic signals. From the stripping current, the concentration of the metal ions present in the solution may be calculated. The final step is to desorb the remaining metal atoms from the

surface (cleaning of the electrode) prior to the next addition of analyte. Adsorption and desorption of the metal ions is accomplished by holding the electrode at a constant potential.

2.9 Summary

In this chapter materials, characterization techniques and analytical methods utilized in the thesis are discussed. Each characterization method was discussed along with the corresponding principle, purpose and preparation procedures.

References

[1]   J.H. Warner, F. Schäffel, A. Bachmatiuk, M.H. Rümmeli, Characterisation Techniques, in: Graphene, *Elsevier* **2013**: pp. 229–332.

[2]   H.L. Poh, F. Šaněk, A. Ambrosi, G. Zhao, Z. Sofer, M. Pumera, Graphenes prepared by Staudenmaier, Hofmann and Hummers methods with consequent thermal exfoliation exhibit very different electrochemical properties, *Nanoscale* 4 (**2012**) 3515.

[3]   D.C. Marcano, D. V. Kosynkin, J.M. Berlin, A. Sinitskii, Z. Sun, A. Slesarev, L.B. Alemany, W. Lu, J.M. Tour, Improved Synthesis of Graphene Oxide, *ACS Nano* 4 (**2010**) 4806–4814.

[4]   Y. Liu, Y. Zhang, G. Ma, Z. Wang, K. Liu, H. Liu, Ethylene glycol reduced graphene oxide/polypyrrole composite for supercapacitor, *Electrochimica Acta* 88 (**2013**) 519–525.

[5]   M. Yi, Z. Shen, S. Ma, X. Zhang, A mixed-solvent strategy for facile and green preparation of graphene by liquid-phase exfoliation of graphite, *Journal of Nanoparticle Research* 14 (**2012**) 1003.

[6]   L.G. Cançado, K. Takai, T. Enoki, M. Endo, Y.A. Kim, H. Mizusaki, A. Jorio, L.N. Coelho, R. Magalhães-Paniago, M.A. Pimenta, General equation for the determination of the crystallite size La of nanographite by Raman spectroscopy, *Applied Physics Letters* 88 (**2006**) 163106.

[7]   C.K. Chua, Z. Sofer, M. Pumera, Graphite oxides: Effects of permanganate and chlorate oxidants on the oxygen composition, *Chemistry - A European Journal* 18 (**2012**) 13453–13459.

[8]   J.G.S. Moo, B. Khezri, R.D. Webster, M. Pumera, Graphene oxides prepared by Hummers', Hofmann's, and Staudenmaier's methods: Dramatic influences on heavy-metal-ion adsorption, *ChemPhysChem* 15 (**2014**) 2922–2929.

[9]   X. Van Heerden, H. Badenhorst, The influence of three different intercalation techniques on the microstructure of exfoliated graphite, *Carbon* 88 (**2015**) 173–184.

[10]   S.S. Jyothirmayee Aravind, K. Ramanujachary, A. Mugweru, T.D. Vaden, Molybdenum phosphide-graphite nanomaterials for efficient electrocatalytic hydrogen production, *Applied Catalysis A: General* 490 (**2015**) 101–107.

[11]   K.H. Lee, J. Oh, J.G. Son, H. Kim, S.S. Lee, Nitrogen-doped graphene nanosheets from bulk graphite using microwave irradiation, *ACS Applied Materials and Interfaces* 6 (**2014**) 6361–6368.

Chapter III

Investigation of graphite properties toward the preparation of graphene based materials

3.1 Introduction

The global demand for graphite and its related carbon materials to be used in mobile energy storage systems alone is expected to grow to more than 100,000 tons per year (https://investorintel.com/sectors/technology-metals/technology-metals-intel/graphite-critical-to-the-development-of-the-automotive-industry/). Graphite type, geological origin, morphology, carbon content, impurities, and defect density significantly influence the preparation of graphene based materials.

The properties of the starting graphite influence the quality of the graphene prepared. Wu et al. compared the quality of the graphene oxide obtained from five different graphite sources, namely, highly ordered pyrolytic graphite (HOPG), natural flake graphite (NFG), kish graphite (KG), flake graphite (FG), and artificial graphite (AG). They observed that a smaller crystallite size possesses weak interlayer bonding which leads to effective oxidation. Variations in the number of graphene layers affect its electronic properties [1]. In another work, Tran et al. investigated the effects of precursor graphite size on prepared graphite oxide and reduced graphene oxide. In this work they considered three graphite samples with 20, 74, and 149 μm lateral dimensions. Their findings were consistent with previous work in that smaller graphite crystallites had the capability to yield effectively oxidized graphite oxide [2]. Graphene oxide yields were higher for small graphite particulates than for larger sized graphite particles. The structure, size, and morphological properties of graphene oxide and reduced graphene oxide were almost similar irrespective of sizes [3].

Chen et al. investigated the oxidation capability of five different synthetic and natural graphite samples. Graphite resident defect densities may be directly correlated with its oxidation ability. The graphene oxide derived from starting graphite with a lower population of defects required less activation energy for ion transport. The extent of oxidation was reduced in the case of lower defect graphite materials [4]. Impurities that were present in the source graphite influenced the property of the graphene based material. A study by Ambrosi et al. showed that synthetic graphite possessed lower impurities compared to natural graphite and metal impurities that were present in the source graphite, which does not get removed completely during oxidation. Trace amount of impurities present in graphite were intercalated such that it is difficult to remove. Impurities present at trace (ppm) levels can dramatically alter the electrochemical and toxicological properties of graphene derivatives. It was also revealed that the catalytic activity of graphene derivatives arises primarily from the metal impurities present within it [5]. In another work, Wong et al. compared the different origins of natural graphite in the preparation of chemically modified graphene, where geological processes and the environment impact their fundamental properties. Their report asserted that most oxidized graphite undergoes efficient reduction and vice versa [6].

Asghar et al. investigated five types of graphite with different morphologies, namely, Chinese flake, Madagascan flake, natural vein, recycled vein, and synthetic to compare their ability to form GIC. Chinese flake graphite showed a high exfoliation volume compared to the Madagascan graphite due to its inherent flake morphology, whereas other types of graphite did not exhibit exfoliation because of their grainy morphology. Thus the morphology of graphite also influences the intercalation phenomena [7]. Kozhemyakina et al. compared the dispersibility and various other properties of different types of graphite such as natural, synthetic, amorphous, etc.

They reported that smaller crystallite sized graphite disperses easily within a solvent. Improved dispersibility facilitates the exfoliation in solvents to generate graphene with just a few layers [8]. The higher carbon content and larger lateral dimensions of kish graphite facilitate the preparation of graphene with a few layers via GIC. It was also observed that the higher carbon content of kish graphite GIC had a larger surface area compared to those with a lower carbon content [9].

Zenyatta ventures ltd discovered the unique Albany graphite deposit formed as a result of hydrothermal process. Unlike vein graphite mined in Sri lanka this graphite is precipitated from CO_2, CH_4, H_2O containing magmatic liquid and its isotopic ratio is identical to graphite precipitated in Fisher-Tropsch synthesis. From the isotopic ratio, it is determined that carbon source for this graphite deposit is from carbon rich country rock through assimilation and devolatization. Average graphite concentration in the deposit is 3.98% and the capacity estimated is 968000 tonnes of graphite. Formation of Albany graphite deposit consists four stages i) intrusion of CO_2 rich magma, ii) formation of CO_2-CH_4 magmatic fluid, iii) development of two tubes and iv) precipitation of graphite. This is unique type of vein graphite i.e highly pure and crystalline graphite [10]. The properties of graphite have an impact on the graphene based materials that are derived from it. Therefore, an investigation of the properties of Albany graphite is critical toward the preparation of graphene based materials.

Graphite properties has strong influence on the quality of graphene prepared from it. Thus it is essential to investigate graphite properties for preparing graphene with desired quality. This chapter provides a comparison of four different types of graphite. Two high purity graphite samples provided by Zenyatta Ventures Ltd., were compared with commercially available graphite. In this chapter, the characteristics and properties of graphite are studied using various techniques. The surface morphology of the graphite was imaged using SEM; crystallinity is

analyzed using XRD, defect density studied by Raman spectroscopy, and electrochemical behavior was studied using cyclic voltammetry.

3.2   Experimental

In this work, graphite samples were used as received for characterization studies without any further purification or treatment.

For electrochemical characterization, the graphite was drop casted onto a glassy carbon electrode (GCE) surface, where a 4mg/ml graphite in 30% ethanol dispersion was prepared with 1% Nafion (100 µL). This dispersion was ultrasonicated for 30 minutes and 5 µL aliquot drop casted on a well-polished GCE, followed by air drying at room temperature. Electrochemical characterization was performed on the graphite-modified GCE in a deaerated 0.5M H_2SO_4 solution at a 100 mV/s scan rate.

3.3   Morphology and composition of graphite

Scanning electron microscopy was used to compare the surface morphology of the graphite samples. From SEM analysis one may glean the size distribution and shape of the material. Figure 3.1 compares the SEM images of different graphite samples, and from this it may be deduced that graphite is a stacks of 2D graphene layers. All graphite possesses a flakey morphology which is similar to what is described in the literature [1], where the flaky morphology is an indication of its crystallinity. Natural flake graphite stands above the others in terms of crystallinity. The formation of this morphology requires higher pressures (up to 1GPa) and higher temperatures 750°C [8], and the nature of the layer distribution varies from sample to sample. The orientation of the graphite sheets was almost flat in the case of AA 325 and SA 325, and in contrast randomly oriented sheets were observed with ZEN 915 and ZEN 378. It was very clear that the lateral dimensions were larger than 10µm for SA 325 and AA 325. In comparison,

in ZEN 378 and ZEN 915, the lateral dimensions were relatively smaller. These differences in layer distribution, orientation, and lateral dimensions among the graphite samples had an impact on the preparation of graphene derivatives, as discussed in the following chapters.
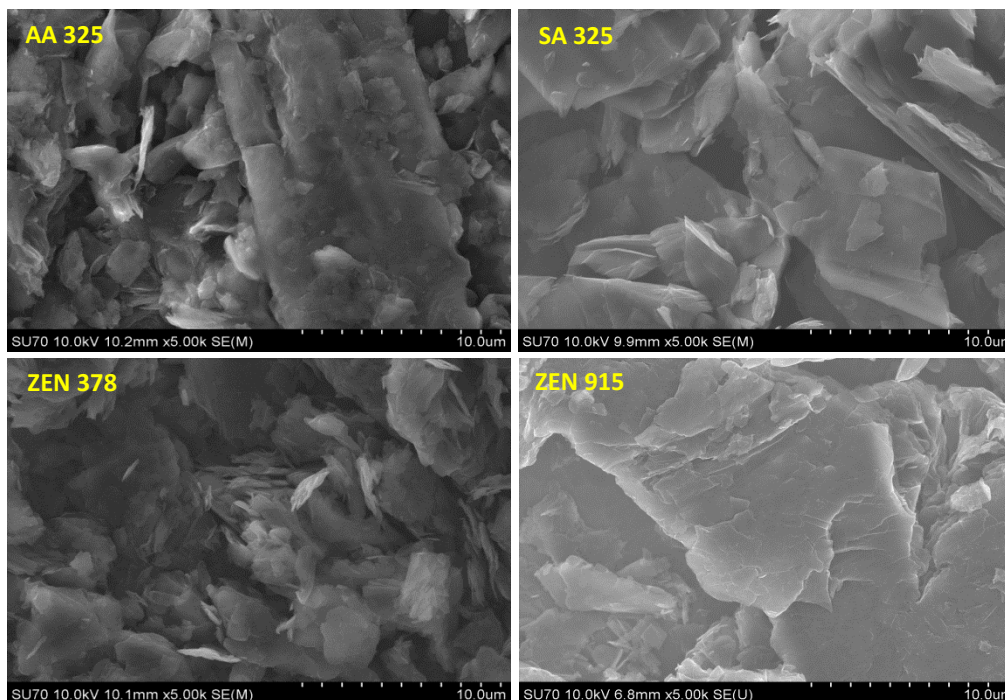
Figure 3.1 SEM images of graphite samples.

The composition of the graphite was determined through the energy dispersive analysis of X-rays (EDX). It was found that there was 100% carbon in the SA 325, ZEN 378, and ZEN 915 samples. However, AA 325 contained 97% carbon, while the remaining content was oxygen and sulfur. Although the EDX technique was not precise enough to confirm the composition, it gave an indication that the AA 325 graphite contained impurities compared to other graphite samples. The accurate composition was further confirmed via X-ray photoelectron spectroscopy is discussed later in this chapter.

3.4 Physiochemical characterization

3.4.1 Specific surface area

The specific surface areas of all the graphite samples were determined with a Quantachrome Nova 220 surface area analyzer, using the N_2 adsorption method. The surface area was computed by the Brunauer–Emmett–Teller (BET) method. The specific surface areas of the AA 325, SA325, ZEN 378, and ZEN 915 samples were 4.11, 9.01, 12.89, and 8.16 m^2/g, respectively. The surface areas obtained are comparable to the values reported for natural graphite, which is 2.71 m^2/g [11,12]. The ZEN 378 graphite had 12.89 m^2/g, which was higher than the other three samples. ZEN 915 was smaller than ZEN 378, and SA 325 and AA 325 were next in the order. The surface area results were in agreement with SEM observations. As SA 325 and AA 325 samples contained larger sheets, they showed a smaller surface area. In addition, a smaller surface area may be result of aggregation sites in graphite. Graphite comprises blocks of 2D graphene sheets; in the case of larger surface areas the number of graphite layers in the blocks was lower in contrast to the smaller surface area graphite. Although the AA 325 graphite contained random lateral sizes, it may have contained additional aggregation sites; hence, it indicated as lower surface area.

3.4.2 Thermal stability

The thermal stability of graphite was examined (TGA- SDT Q600) in presence of ambient air, with the Thermal gravimetric analysis (TGA) graphs of all graphite samples shown in Figure 3.2(A)**.** The graphite samples may be arranged in the following order, from low to high thermal stability; ZEN 378 < ZEN 915 < AA 325 < SA 325. Thermal stability depends on the oxygen content of the graphite, where the ZEN 378, ZEN 915, and AA 325 graphite samples might possess trace levels of oxygen, however the oxygen content could not be traced from EDX because of the lower sensitivity of the instrument. Another factor relates to structural defects, as

it is known that defective sites are reactive. Graphite with defects will undergo oxidation more readily as compared to crystalline graphite. The energy change accompanied with the raised temperature was monitored via differential scanning calorimetry (DSC). The DSC curves show the energy exerted or absorbed during the heating of the known mass of the graphite samples (Figure 3.2(B)). The energy lost is due to exothermic reactions, for all of the graphite samples. The mass loss associated with temperatures of above 500°C was due to the combustion of graphite. It has been reported that in a nitrogen environment, graphite is stable to over 1000°C. As one studied the stability of graphite in the presence of ambient air, the graphite reacted with oxygen when the temperature exceeded 500°C. The SA 325 sample reacted with oxygen when the temperature exceeded 600°C due to the fact that it was purer and more crystalline than the other samples.
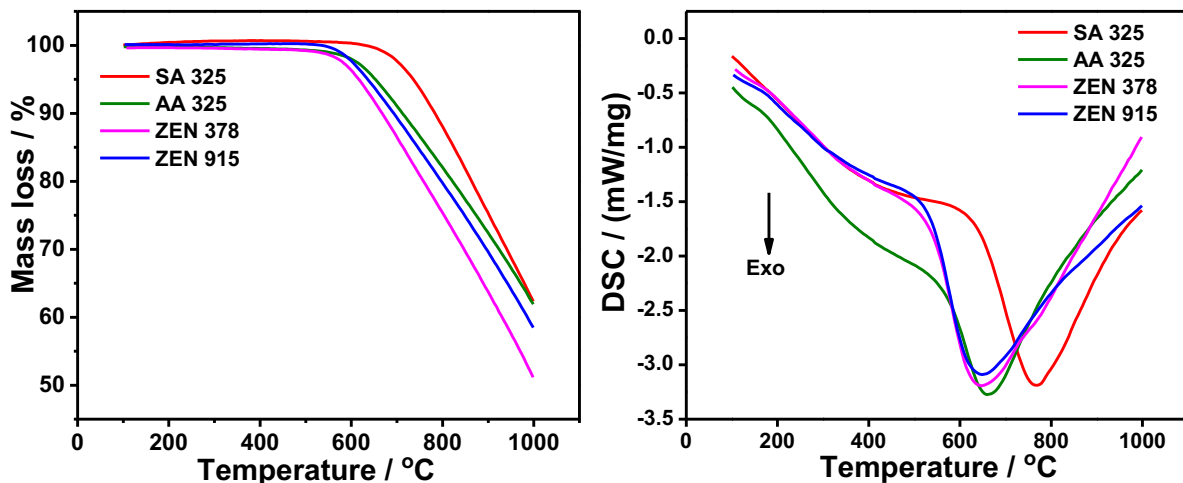
Figure 3.2 (A) Thermogravimetric analysis of graphite samples, (B) Differential scanning calorimetry curves of graphite samples.

3.4.3 Crystallinity of graphite - X-ray diffraction

The crystallinity of graphite was compared by X-ray diffraction studies. All graphite samples showed the characteristic peak for graphite around $2\Theta = 26.42°$, which corresponded to its hexagonal structure. Respective h k l values were found to be (0 0 2), which indicated a layered sheet structure (Figure 3.3(A)). From the peak position, the d spacing between the layers may be computed. The interlayer distances of the graphite samples were practically identical, and were calculated to be 0.3374, 0.3375, 0.3362, and 0.3366 nm for the AA 325, SA 325, ZEN 378, and ZEN 915 graphite samples. The SA 325 sample appeared more crystalline in contrast to the others, and is inferred from the intensity of the characteristic peak at 26.42°. In Figure 3.3(B), weak peaks observed between 40° to 90° are shown, and the corresponding h k l values are marked based on data from the literature [13]. In addition, the obtained pattern is matched with reference code- 98-001-7146 in the ICSD data base, which corresponds to graphite.

As graphite is a polycrystalline material, its average crystallite dimensions may be calculated in two directions, namely, the horizontal direction (basal plane) and vertical direction (c-direction). The crystallite calculation was performed using the Scherrer formula shown in equations (3.1) and (3.2) [14,15, 16]. The (0 0 2) plane corresponded to the c direction; hence, the crystallite size was denoted as Lc. For the basal plane it was determined from the weak peak that corresponded to the (100) plane at 42.30°, which is denoted as La. The full width of the peak was measured at half maximum intensity (FWHM) for all of the graphite samples in order to calculate the average crystallite size.

$$Lc = \frac{0.90 \times \lambda}{(B002 \times \cos\theta 002)}$$ 3.1

$$La = \frac{1.84 \times \lambda}{(B100 \times \cos\theta 100)}$$ 3.2

λ= wavelength of X ray used for analysis 1.54056 Å

B002, B100 = FWHM of the peaks of corresponding planes

Using crystallite size (Lc) the number of layers may be determined using equation (3.3),

$$number\ of\ layers(N) = \frac{Lc(nm)}{d(nm)} \quad ....3.3$$
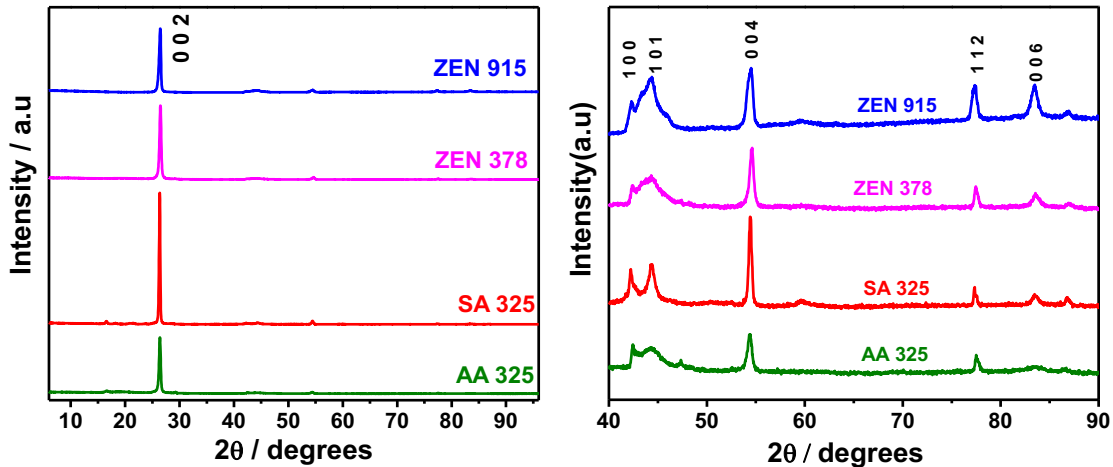
Figure 3.3 (A) X-ray diffractogram of AA 325, SA 325, ZEN 378, and ZEN 915 graphite, (B) magnified XRD spectrum, from 40-90°.

The crystallite size, d spacing, and the number of layers are shown in Table-3.1. The ZEN samples had a similar crystallite size (Lc), whereas the SA 325 graphite was larger compared to the other samples. This indicated that the SA 325 graphite possessed a higher number of layers. The La values were similar for AA 325, SA 325, and ZEN 378; however, ZEN 915 was smaller than the other samples. The crystallite size deduced from the XRD was not comparable to the SEM morphology particle size, as this technique is sensitive to thin folds or crumples in the structure. The number of layers found was 72, 97, 69, and 62 in AA 325, SA 325, ZEN 378, and ZEN 915 respectively. The ZEN 915 samples had a smaller crystallite size and lower number of

layers compared to the other samples. Aspect ratio is defined as width/height; for graphite it is La/Lc, and was in the order of AA 325 > ZEN 378 > SA 325 > ZEN 915.

Table 3.1 X-ray diffraction data analysis, crystallite size, d spacing, and calculated number of layers.

Sample Name	2Θ	d spacing (nm)	(0 0 2) Lc (nm)	(1 0 0) La (nm)	Aspect ratio	N (number of Layers)
AA 325	26.396	0.3374	24.30		2.06	72
	42.431			49.95		
SA 325	26.370	0.3375	32.79		1.40	97
	42.226			45.96		
ZEN 378	26.288	0.3362	23.12		1.78	69
	42.177			41.17		
ZEN 915	26.461	0.3366	20.83		1.30	62
	42.310			27.14		

3.4.4 Composition of graphite - X-ray photoelectron spectroscopy

The X-ray photoelectron spectroscopy (XPS) technique is beneficial to elucidate the precise composition of a material, as well as the oxidation states of the species that are present within it. Figure 3.4(A) depicts the XPS survey spectrum of all the graphite samples. The composition obtained from the XPS analysis contained two elements, namely, carbon and oxygen. The carbon content of the graphite samples was 96.30, 98.56, 94.80, and 92.70 at.% for AA 325, SA 325, ZEN 378, and ZEN 915, respectively. The oxygen content of each graphite sample may be easily distinguished in the Figure 3.4(B) O1s spectrum of all the samples. The oxygen content was observed from 2.68 to 7.30 at%. The calculated O/C ratio of the graphite samples showed SA

325 (0.03) as the lowest, with ZEN 915 (0.08) as the highest. The SA 325 graphite had a high carbon content compared to the other samples, which was consistent with the EDX analysis. Interestingly, the oxygen content in the graphite samples was significantly different. It was in the order of ZEN 915 > ZEN 378 > AA 325 > SA 325. The ZEN samples contained relatively higher oxygen content than did the commercial graphite samples. The HR C1s spectra reveals a similar pattern for all of the graphite samples (C-C bonding with sp^2 hybridization), which is characteristic for graphite.
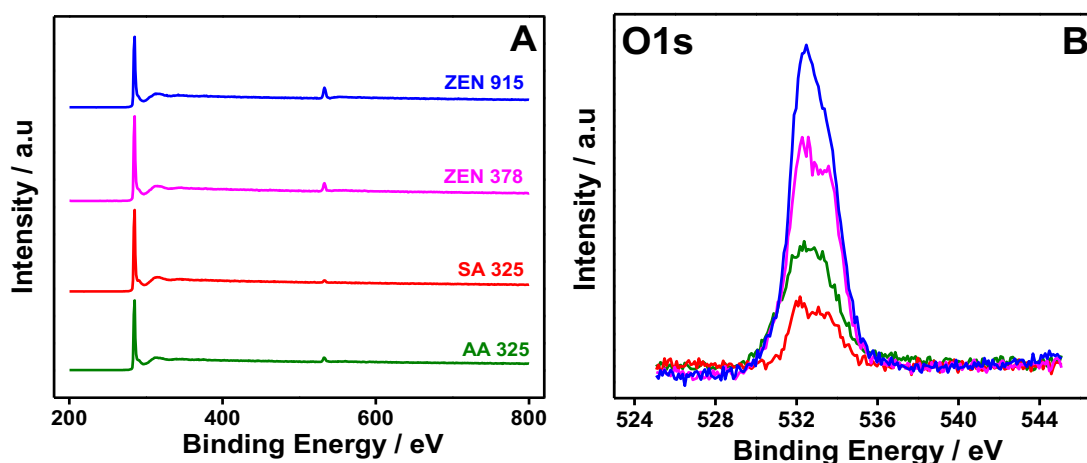
Figure 3.4 (A) X-Ray Photoelectron spectrum of AA 325, SA 325, ZEN 378, and ZEN 915 graphite, (B) O1s spectra of graphite samples.

3.4.5 Raman spectroscopy

Raman spectroscopy is an effective probe for the analysis of carbon nanomaterials, and imparts significant information as to the structural defect density, crystallinity, and number of layers. The defect density may be gauged from the d band which appears at 1350 cm^{-1}, and is the result of scattering from the defects that are present in the structure [17-20]. Structural stability may be deduced from the intensity of the G band, which is due to the in-plane vibrations of sp^2

carbon atoms. Another characteristic feature is the 2D band, which provides information on the graphene layers that are stacked up in graphite [17–20].

For Raman measurements, graphite is dispersed in water and cast on glass slides, and then dried at room temperature. A 514 nm laser light beam was used for Raman scattering, whereas a confocal microscope and 100X magnification was employed to focus the spot. Figure 3.5 depicts a comparison of the Raman spectra of the AA 325, SA 325, ZEN 378, and ZEN 915 graphite samples. All samples showed characteristic graphite peaks, namely, D, G, and 2D bands located at ~1350 cm^{-1}, ~1560 cm^{-1} and ~2700 cm^{-1} respectively. There was no significant difference in the position of the peaks, and the G band, predominant among other two, indicated the crystalline
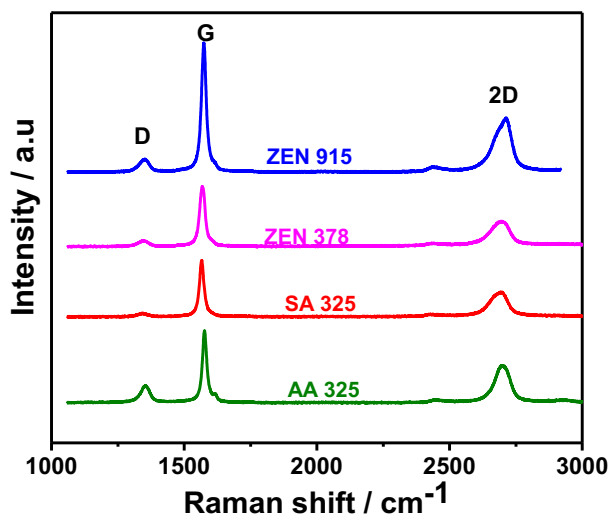
Figure 3.5 Raman spectra of AA 325, SA 325, ZEN 378, and ZEN 915 Graphite.

nature of the graphite. The calculated Id/Ig ratio was 0.23, 0.06, 0.09, and 0.10 for AA 325, SA 325, ZEN 378, and ZEN 915, respectively. The D band was practically nil and the weakest band indicated imperfections in the structure, where the intensity of the D band was in following order: AA 325>ZEN 915>ZEN 378>SA 325. This indicated that AA 325 possessed more defects than did the other three samples. The ZEN samples had identical defect densities, whereas SA 325 has

the lowest defect density which indicates pure and crystalline graphite. The 2D band at ~2700 cm^{-1} was weaker and broader than the G band and is characteristic of graphite [21].

3.5   Electrochemistry

The basic electrochemical characterization of graphite was conducted in order to understand its specific capacitance and potential stability.

3.5.1 Cyclic voltammetry

Cyclic voltammetry is a fundamental electrochemical technique that is used to study the electrochemical activity of a material. In this method, the applied potential of the working electrode (graphite) is increased, from -0.2 to 1.0 V with respect to an Ag/AgCl reference electrode at a 100 mV/s rate, and measures the current that is flowing between the working electrode and the Pt counter electrode, precisely followed by same process in the reverse direction. Figure 3.6 displays the cyclic voltammetry responses of AA 325, SA 325, ZEN 378, and ZEN 915 graphite samples, with a selected potential window of from -0.2V to 1.0V. A glassy carbon electrode was used as a substrate; thus, it was compared along with the graphite samples. All of graphite samples showed a rectangular pattern, which is indicative of a capacitive material that does not have any redox species on its surface. For graphite, the edge sites and surface functional groups are electrochemically active species. A small hump observed at ~0.38V, was attributed to trace surface oxygen functionalities that were present in the graphite and defect sites [22]. This result was consistent with XPS observations and Raman spectroscopy results, and the area of the curve was directly related to the capacitance of the material. The SA 325 sample has a low capacitance in contrast to the other graphite samples. ZEN 378 had the relatively highest capacitance compared to ZEN 915 and AA 325. There was very small

difference between AA 325, ZEN 378, and ZEN 915. Further specific capacitance studies were conducted in order to precisely quantify the capacitance of the graphite samples.
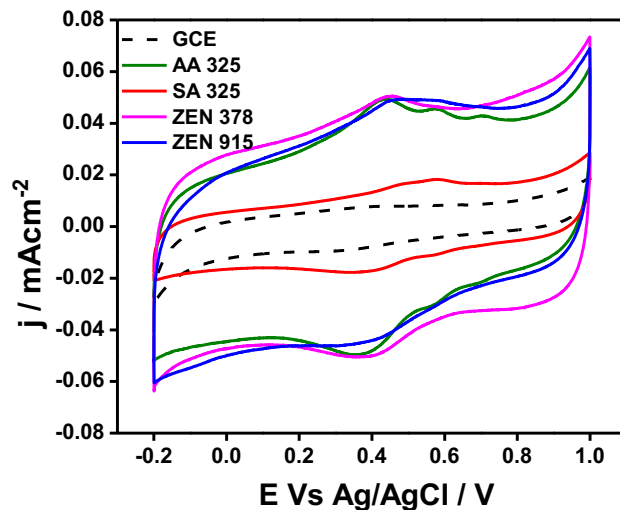
Figure 3.6 Cyclic voltammograms of AA 325, SA 325, ZEN 378, and ZEN 915 graphite recorded in 0.5M H_2SO_4 at a scan rate of 100 mV/s.

3.5.2 Specific capacitance

Capacitance studies were performed in galvanostatic mode, which involves applying/drawing a constant current to measure the charge/discharge ability of a material, respectively. The current is normalized with respect to the mass of material present in the working electrode, and a 100 mA/g current and potential window from 0 to 1 V was selected. Charge/discharge studies were performed in 0.5M H_2SO_4. From the discharge duration, the specific capacitance of the material may be calculated using equation 3.4 [23].

$$Capacitane = \frac{(I \times \Delta t)}{(m \times \Delta V)} \text{ F/g} \dots\dots\dots\dots\dots\dots\dots\dots\dots 3.4$$

I-discharge current (A); Δt-discharge duration (s); m-mass of active material (g); ΔV-working voltage range (V)

Charge/discharge experiments were continuously performed for five cycles until stable results were observed. Representative charge/discharge curves are depicted in Figure 3.7. The specific capacitance computed from the discharge duration was 1.29, 0.41, 1.53, and 1.48 Farads/gram for AA 325, SA 325, ZEN 378, and ZEN 915, respectively. These values were consistent with the CV results. SA 325 has lowest capacitance, which may have been attributed to larger particle size and lower defects. Although ZEN 378 showed a slightly higher capacitance, ZEN 915 and AA 325 were not far from it. The ZEN 915, ZEN 378, and AA 325 graphite samples showed an almost 3-fold higher capacitance than the SA 325 graphite sample. This higher value might have been related to the oxygen content and the defect density.
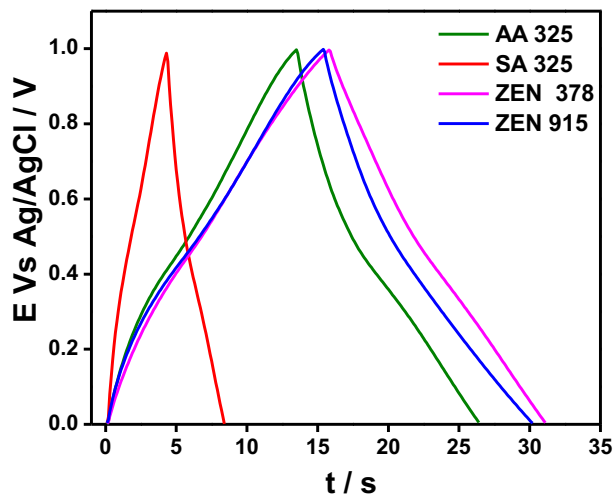
Figure 3.7 Galvanostatic charge/discharge of AA 325, SA 325, ZEN 378, and ZEN 915 graphite samples recorded in 0.5M H_2SO_4 at discharge current of 100 mA/g.

3.5.3 Potential range

The electrochemical stability of graphite was investigated in 0.5M H_2SO_4. Electrochemical stability is important for various applications, in terms of durability and performance of the material. Graphite possesses a wide operating potential window; hence, we selected -0.7 V to 1.6

V was selected. The full range cyclic voltammograms of AA 325, SA 325, ZEN 378, and ZEN 915 are shown in Figure 3.8. The SA 325 sample appeared more stable over the potential range examined, as there were no sudden spikes in current observed at more negative, and at more positive potentials. In contrast, the remaining three graphite samples showed a significant change in current following exposure to ~1.30 V in the positive direction. This current increase corresponded to oxygen evolution due to water electrolysis. Oxygen evolution occurred at a lower potential for the ZEN graphite samples and AA 325, than the SA 325 graphite due to the presence of electroactive species. In the reverse direction hydrogen evolution occurred and the increase in the corresponding current was observed at ~ -0.60V for AA 325, ZEN 378, and ZEN 915. The SA 325 graphite sample was stable in the negative direction until -0.65 V was attained, which was 50 mV wider than the other graphite samples. The wider potential range of SA 325 corresponded to its high carbon content and no oxygen content. The capacitance was larger for ZEN 378 in the wider potential window, same trend as in CV can be witnessed.
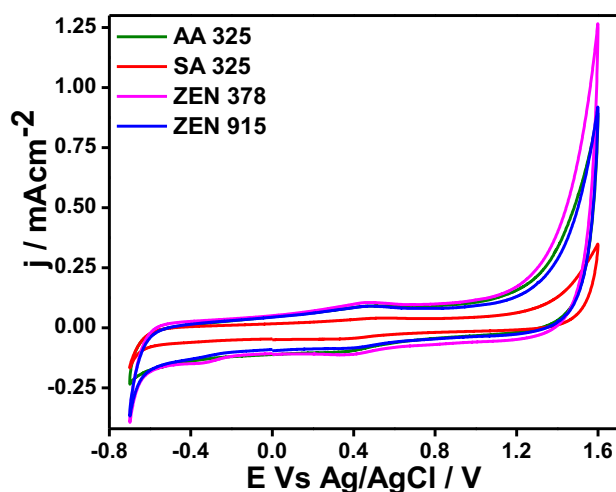
Figure 3.8 Full range cyclic voltammogram of AA 325, SA 325, ZEN 378, and ZEN 915 graphite recorded in 0.5M H_2SO_4 at the scan rate of 100 mA/g.

3.6 Summary

In this project the physiochemical and electrochemical properties of four different graphite samples were investigated in detail to understand their capability for the preparation of graphene oxide based derivatives. Summary of this analysis is shown in Table 3.2. Based on the morphology results ZEN 378 showed smaller particle sizes than other graphite samples; hence, it might have a higher oxidative ability in contrast to the other samples. The surface area of ZEN 378, was then analyzed, and the high surface area was consistent with SEM observations. The thermal stability of the graphite samples was investigated in ambient atmosphere, with no significant differences observed among the four graphite samples. Further, the SA 325 graphite was relatively more stable in comparison to the other samples. XRD observations conveyed additional information on the graphite crystallinity, interlayer spacing, average crystallite size, and number of layers. The SA 325 sample had more stacked layers of graphite and a larger crystallite size compared to the others samples. This might relate to the extent of exfoliation, which may not be efficient in larger size graphite materials. Further, XPS imparted a clearer understanding of the composition of graphite. It was discovered that all graphite samples have some level of surface oxygen content, and the ZEN 915 exhibited a higher oxygen % compared to the other samples. Raman spectroscopy revealed additional information on defect density; accordingly AA 325 revealed a higher defect density, which translated to its having an improved oxidative ability. Further to this, the electrochemical properties of the graphite samples were studied to elucidate the specific capacitance and potential stability. The SA 325 graphite exhibited a lower capacitance and wider potential window. This observation complemented previous results, which included high carbon content, large crystallite size, low surface area, and

fewer defects. This analysis provided a better understanding of graphite and its capability to produce graphene derivatives.

Table 3.2 Summary of graphite samples' properties

Parameter	*Superior*	*Trend*	*Inferior*
Surface area	**High**	**ZEN 378 > SA 325 > ZEN 915 > AA 325**	**Low**
Thermal stability	**High**	**SA 325 > AA 325 > ZEN 915 > ZEN 378**	**Less**
Sheet size (La)	**Smaller**	**ZEN 915 < ZEN 378 < AA 325 < SA 325**	**Bigger**
Number of layers	**Fewer**	**ZEN 915 < ZEN 378 < AA 325 < SA 325**	**More**
I_d/I_g ratio	**Large**	**AA 325 > ZEN 915 < ZEN 378 < SA 325**	**Fewer**
Oxygen content	**High**	**ZEN 915 > ZEN 378 > AA 325 < SA 325**	**Slower**
Specific capacitance	**High**	**ZEN 378 > ZEN 915 > AA 325 > SA 325**	**Low**

 References

[1]   Z.S. Wu, W. Ren, L. Gao, B. Liu, C. Jiang, H.M. Cheng, Synthesis of high-quality graphene with a pre-determined number of layers, *Carbon* 47 (**2009**) 493–499.

[2]   M.-H. Tran, C.-S. Yang, S. Yang, I.-J. Kim, H.K. Jeong, Influence of graphite size on the synthesis and reduction of graphite oxides, *Current Applied Physics* 14 (**2014**) S74–S79.

[3]   J. Chen, Y. Li, L. Huang, C. Li, G. Shi, High-yield preparation of graphene oxide from small graphite flakes via an improved Hummers method with a simple purification process, *Carbon* 81 (**2015**) 826–834.

[4]   Z.-L. Chen, F.-Y. Kam, R.G.-S. Goh, J. Song, G.-K. Lim, L.-L. Chua, Influence of Graphite Source on Chemical Oxidative Reactivity, *Chemistry of Materials* 25 (**2013**) 2944–2949.

[5]   A. Ambrosi, C.K. Chua, B. Khezri, Z. Sofer, R.D. Webster, M. Pumera, Chemically reduced graphene contains inherent metallic impurities present in parent natural and synthetic graphite, *Proceedings of the National Academy of Sciences* 109 (**2012**) 12899–12904.

[6]   C.H.A. Wong, Z. Sofer, M. Pumera, Geographical and Geological Origin of Natural Graphite Heavily Influence the Electrical and Electrochemical Properties of Chemically Modified Graphenes, *Chemistry - A European Journal* 21 (**2015**) 8435–8440.

[7]   H.M.A. Asghar, S.N. Hussain, H. Sattar, N.W. Brown, E.P.L. Roberts, Potential Graphite Materials for the Synthesis of GICs, *Chemical Engineering Communications* 202 (**2015**) 508–512.

[8]   N. V. Kozhemyakina, S. Eigler, R.E. Dinnebier, A. Inayat, W. Schwieger, A. Hirsch, Effect of the Structure and Morphology of Natural, Synthetic and Post-processed Graphites on Their Dispersibility and Electronic Properties, *Fullerenes, Nanotubes and Carbon Nanostructures* 21 (**2013**) 804–823.

[9]   J.-C. An, H.J. Kim, I. Hong, Preparation of Kish graphite-based graphene nanoplatelets by GIC (graphite intercalation compound) via process, *Journal of Industrial and Engineering Chemistry* 26 (**2015**) 55–60.

[10]   A.G. Conly, L.C. Moore, Geology, ore characteristics, and origin of the Albany graphite deposit, *British Columbia Geological Survey Paper* 3 (**2015**) 173–185.

[11]   M.-S. Park, J.-H. Kim, Y.-N. Jo, S.-H. Oh, H. Kim, Y.-J. Kim, Incorporation of phosphorus into the surface of natural graphite anode for lithium ion batteries, *Journal of Materials Chemistry* 21 (**2011**) 17960.

[12]   G. Sun, X. Li, Y. Qu, X. Wang, H. Yan, Y. Zhang, Preparation and characterization of graphite nanosheets from detonation technique, *Materials Letters* 62 (**2008**) 703–706.

[13]   Z.Q. Li, C.J. Lu, Z.P. Xia, Y. Zhou, Z. Luo, X-ray diffraction patterns of graphite and turbostratic carbon, *Carbon* 45 (**2007**) 1686–1695.

[14]   D. Roy Chowdhury, C. Singh, A. Paul, Role of graphite precursor and sodium nitrate in graphite oxide synthesis, *RSC Advances* 4 (**2014**) 15138.

[15]   B. Manoj, A.G. Kunjomana, Study of stacking structure of amorphous carbon by X-ray diffraction technique, *International Journal of Electrochemical Science* 7 (**2012**) 3127–3134.

[16]   F.R. Feret, Determination of the crystallinity of calcined and graphitic cokes by X-ray diffraction, *The Analyst* 123 (**1998**) 595–600.

[17]   H. Feng, X. Wang, D. Wu, Fabrication of spirocyclic phosphazene epoxy-based nanocomposites with graphene via exfoliation of graphite platelets and thermal curing for enhancement of mechanical and conductive properties, *Industrial and Engineering Chemistry Research* 52 (**2013**) 10160–10171.

[18] D. Joseph, N. Tyagi, A. Ghimire, K.E. Geckeler, A direct route towards preparing pH-sensitive graphene nanosheets with anti-cancer activity, *RSC Advances* 4 (**2014**) 4085–4093.

[19] D. Nuvoli, L. Valentini, V. Alzari, S. Scognamillo, S.B. Bon, M. Piccinini, J. Illescas, A. Mariani, High concentration few-layer graphene sheets obtained by liquid phase exfoliation of graphite in ionic liquid, *Journal of Materials Chemistry* 21 (**2011**) 3428–3431.

[20] A. Kaniyoor, T.T. Baby, S. Ramaprabhu, Graphene synthesis via hydrogen induced low temperature exfoliation of graphite oxide, *Journal of Materials Chemistry* 20 (**2010**) 8467.

[21] L.G. Cançado, K. Takai, T. Enoki, M. Endo, Y.A. Kim, H. Mizusaki, A. Jorio, L.N. Coelho, R. Magalhães-Paniago, M.A. Pimenta, General equation for the determination of the crystallite size La of nanographite by Raman spectroscopy, *Applied Physics Letters* 88 (**2006**) 163106.

[22] Z. Lin, Y. Liu, Y. Yao, O.J. Hildreth, Z. Li, K. Moon, C.P. Wong, Superior capacitance of functionalized graphene, *Journal of Physical Chemistry C* 115 (**2011**) 7120–7125.

[23] H.. Yu, K.. Xie, J.. Hu, C.. Shen, J.-G.. Wang, B.. b Wei, The importance of raw graphite size to the capacitive properties of graphene oxide, *RSC Advances* 6 (**2016**) 17023–17028.

Chapter-IV

Chemical and electrochemical characterization of graphene oxide synthesized from different graphites

4.1   Introduction

Graphene oxide is a potential intermediate for the preparation of graphene. Graphene oxide is obtained through the exfoliation of graphite oxide. Graphite oxide has a long history since 1859. The term graphite oxide is derived from 'Graphitic acid'. Interest in the preparation of graphene oxide accelerated following the isolation of graphene sheets by micromechanical cleavage in 2004 by Geim et al. [1]. Graphene oxide has been explored for various electrochemical applications due to its excellent properties, namely, sensors, electrocatalysis, electrochemical energy storage, and photocatalysts.

The evolution of graphite oxide preparation is briefly illustrated in Table 4.1. In 1859 Brodie synthesized graphite oxide for the first time, using $KClO_4$ as an oxidizing agent. The oxidation procedure was repeated three times until no further changes were observed in the final product. Limitations of this method are long preparation duration and toxic gas evolution [2]. Later, in 1898, Staudenmaier improved on this procedure toward efficient oxidation. In this method excess $KClO_4$ and sulfuric acid were used as oxidizers and the reaction was conducted at room temperature. Although this method oxidized graphite under controlled conditions, the toxicity of the process was high due to excess $KClO_4$ [3]. Further to this, in 1937 Hofmann improved this method by reducing the toxicity of the process. Based on the Hofmann method, 1:2 nitric acid and sulfuric acid was used without any change in the $KClO_4$ and graphite. The remaining processes were similar to the Staudenmaier method. For this technique, nitric acid was used in place of fuming nitric acid; thus, the toxicity was further reduced. This process gave hope for

bulk production and improvement, as the toxicity was reduced [4]. Subsequent to this, in 1957 Hummers and Offeman introduced a method to prepare graphite oxide over two days, which is the most widely used and explored method. In this method, potassium permanganate and sodium nitrate were employed as oxidizers in sulfuric acid. The oxidation of graphite was performed under high temperatures, albeit for a shorter duration. Again, toxic gas evolution was the limitation of this process [5]. Several modifications have been reported to the Hummers method toward the reduction of the toxic gas evolution, duration of process, etc. These modifications include adding excess sodium nitrate and potassium permanganate and adjusting the duration of the process. [7]. In 2010, Tour et al. reported a method referred to as the improved Hummers method which was a more rapid process that demonstrated a significant improvement in yields, and the properties of the resulting graphite oxide. In this method GO had fewer defects in the basal plane, no toxic gas evolution, and high yield (effective oxidation), compared to the standard Hummers' method [6].

There have been several novel methods reported for the preparation GO with fewer defects and a faster procedure. Graphite oxide preparation carried out with same reagents used in the Hummers' method reaction was conducted at less than 10°C and for 16 hours. The rinsing process was also carried out at below 10°C. This resulted in a C/O ratio that was similar to Hummer's method, and the defect density was significantly reduced with compromise in yield. This opened the way to prepare graphene with fewer defects; equivalent to chemical vapor deposition technique [8]. In 2014, K_2FeO_4 was reported as an oxidizer for the preparation of graphene oxide. This process took one hour at room temperature, with no toxic gas evolution, as well as a simplified washing procedure [9].

Table 4.1 Graphite oxide preparation methods.

Year	Method	Oxidizer	Acid	Toxicity	Duration	Ref
1859	**Brodie**	$KClO_4$ (3X graphite)	Fuming HNO_3	Hazardous chemicals, 60°C ClO_2, $KClO_3$	1 Day reaction X 3 times	[2]
1898	**Staudenmaier**	$KClO_4$ (11X graphite)	Fuming HNO_3 + H_2SO_4 (1:3)	Toxic gas $KClO_3$, ClO_2, CO_2	Four days reaction	[3]
1937	**Hofmann**	$KClO_4$ (11X graphite)	HNO_3 + H_2SO_4 (1:2)	Toxic gas $KClO_3$, ClO_2, CO_2	Four days reaction	[4]
1958	**Hummers**	$NaNO_3$ (0.5Xgraphite) $KMnO_4$ (3X graphite)	H_2SO_4	35°C = 30 min 98°C = 15 min Toxic gas NOx, Mn_2O_7	2-10 hours	[5]
2010	**Tour**	$KMnO_4$ (6X graphite)	H_3PO_4 + H_2SO_4 (1:9)	No toxic gas	12-15 hours	[6]

Graphene oxide comprises oxygen functional group decorated graphene sheets. It is non-stoichiometric compound, and its exact structure is not known. The composition of functional groups varies from method to method; hence, it is challenge to propose a defined structure and chemical formula. According to Lerf-Klinowski model, hydroxyl and epoxyl groups were attached to basal planes, whereas carbonyl and carboxyl were connected to the edge sites [10]. Graphene oxide properties vary with respect to the preparation and purification methods. Graphene oxide is a semiconductor due to the presence of a large population of oxygen functional groups, and structural sp^3 defects. As GO contains reactive surface functional groups, it is an excellent platform for functionalization. In addition it exhibits high electron mobility due to the existence of monolayers and a high surface area [11,12]. The properties of graphene oxide

prepared by different methods are presented in Table 4.2. The properties of graphene oxide may be manipulated by varying experimental conditions and the dosage of oxidizing agents. The adsorption capacity of GO can be increased by ultrasonication of GO dispersion in water. This is attributed to the exfoliation into monolayer graphene oxide, which enhanced the active surface area [13]. Lee et al. investigated the effects of the duration of oxidation, where the longer the duration, the sp^2 carbon content was decreased, while the sp^3 carbon content was increased [14].

Table 4.2 Comparison of graphene oxide properties prepared by various methods.

Parameter	Description	Trend	Description
C/O ratio	Low	HU<HO<BR<ST	High
Duration of process	Shorter	HU<HO<ST<BR	Longer
Heterogeneous electron transfer rate	Slower	TO<HU<ST<HO	Faster
Interlayer distance	Wider	TO>HU>HO>ST>BR	Narrower
Sheet size (FWHM)	Smaller	ST<BR<HU	Bigger
Charge Transfer Resistance 50mM PBS pH 7.2 / 10 mM FeCN	High	TO<HU<ST<HO	Low
I_d/I_g ratio	Fewer	TO<HU=HO<BR<ST	Large
Protonic conductivity	High	HU>ST>BR	Low
Carbonyl and carboxyl functional groups	High	HU, TO > > HO, ST	Low
Affinity to Pb II and Cd II (proportional to carboxyl)	High	HU>HO>ST	Low
Reduction peak potential		ST,HO= -1.2 to -1.3V HU,TU= -1.4 to -1.8V	
Abbreviation		BR-Brodie GO, ST-Staudenmaier GO, HO-Hofmann GO, HU-Hummers' GO and TO-Tour's GO	
References [6,7,16–19]			

Morimoto et al. reported effects of the dosage of oxidizing agents in reducing the oxygen content in GO, and also the stepwise reduction of GO for tuning the C/O ratio. As per their results, a 23% oxygen content of GO exhibits high electrochemical capacitance [15].

Graphene oxide properties are varied with respect to the source graphite material. Smaller sized graphite undergoes effective oxidation and produces smaller sized graphite oxide. Smaller GO will undergo effective reduction and demonstrated improved electrochemical energy storage properties [20]. In contrast, Yu et al. reported that larger size graphite generated high specific capacitance graphene oxide [21]. The chemical oxidative reactivity of graphite may be related to its defect density. A higher defect density will possess additional active sites and high activation energy for charge transport, which facilitates the oxidation process [22]. Furthermore, the pretreatment of graphite influences the properties of the resultant graphene oxide. Electron beam irradiated graphite was subjected to oxidation via an improved Hummer's method. The dosage of electron beam irradiation increased the density of oxygen functional groups. This was due to defects that were induced into graphite during electron beam irradiation [23]. Thus, the selection of the appropriate graphite source is essential for the synthesis of graphene oxide with the desired characteristics. The objective of this chapter is to investigate different graphite samples in the preparation of graphene oxide.

For this project, graphene oxide was synthesized from four different graphite samples through an improved Hummers' method with a slight modification. To understand the influence of graphite properties, graphene oxide was investigated using a similar method as was done for graphite. The surface morphology of the graphene oxide was compared using SEM images and the C/O ratio was determined from EDX composition analysis. Crystallographic changes were then examined by X-ray diffraction analysis. Subsequently, Fourier transform spectroscopy was

employed to elucidate the oxygen functional groups, followed by defect density changes, which were probed by Raman spectroscopy. Finally, fundamental electrochemical characterization was investigated using cyclic voltammetry, specific capacitance, heterogeneous electron transfer properties, and full range cyclic voltammetry techniques.

4.2   Experimental

4.2.1   Synthesis of graphene oxide

Graphene oxide was synthesized with slight modifications to an improved Hummers' method. The synthesis method is illustrated in Figure 4.1.
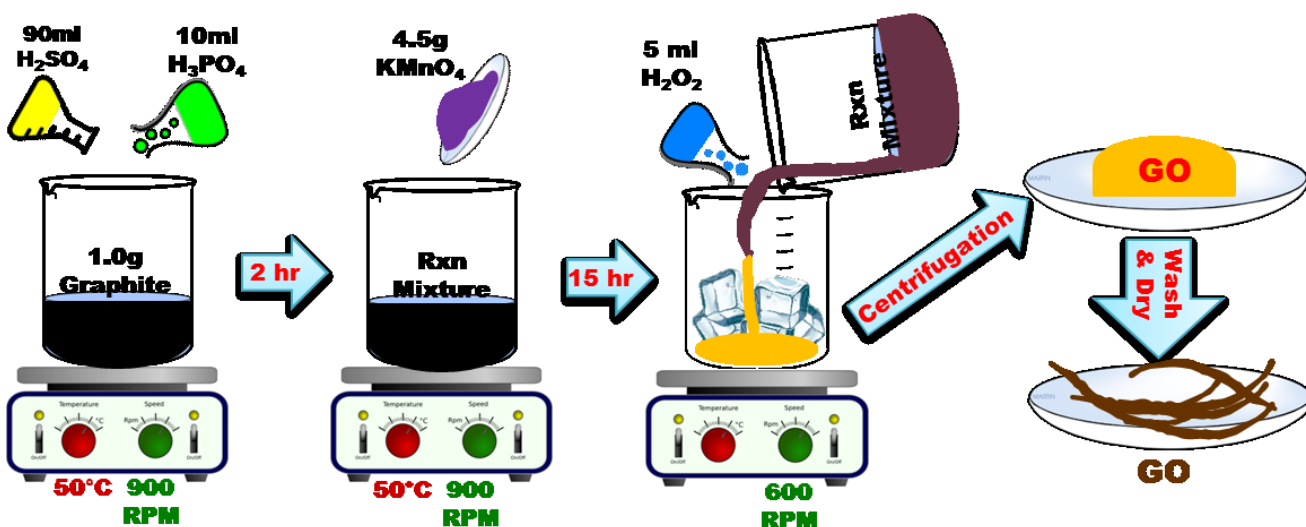
Figure 4.1 Scheme for synthesis of graphene oxide.

In a typical method, 4.0 g of graphite is mixed with 400 ml of 9:1 sulfuric acid (98%) and phosphoric acid (85%), and mixed vigorously at 900 RPM. The temperature of the mixture was maintained at 50°C for 2 hours; soon afterward 18 g of $KMnO_4$ was slowly added over 15 minutes. As the reaction proceeds the mixture was become thick and brown in color. The reaction continued for 15 hours after which the mixture was cooled down to room temperature, and then poured onto 400 ml of ice, and the excess $KMnO_4$ was consumed by adding 20 ml of 30%

hydrogen peroxide. The colour of the mixture then turned from brown to a yellowish colour. The mixture was then centrifuged and the supernatant was discarded, using 200 ml 30% HCl; 5 times water, then 200 ml ethanol, and finally soaked in diethyl ether. Subsequently, the product was dried at <60°C for 24 hours [6].

The four graphite samples investigated in Chapter-III were used in the preparation of graphene oxide. Along with the graphite sample name, the GO suffix is included. Graphene oxide from AA 325, SA 325, ZEN 378, ZEN 915 graphite samples are denoted as AA 325-GO, SA 325-GO, ZEN 378-GO, and ZEN 915-GO, respectively.

For this synthesis procedure the improvements to Hummers' method include the increased quantity of $KMnO_4$, and the inclusion of phosphoric acid. Sodium nitrate is not included as it causes toxic gas evolution; hence, the quantity of $KMnO_4$ was increased to compensate for that. Phosphoric acid caused the formation of five-membered cyclic phosphate groups, which assisted with protecting the basal planes of the graphene sheets, as it reduces the generation of defects. Furthermore, no toxic gas was produced during this procedure [6].

4.2.2 Electrode preparation

The electrochemical characterization of graphene oxide was performed with a glassy carbon electrode that was modified with GO. For the modification, 4 mg of graphene oxide is dispersed in 900 µL water and 100 µL of 1% Nafion, which was then sonicated for 1 hour. A 3µL aliquot was drop casted onto a well-polished GCE surface and then dried at room temperature. For heterogeneous electron transfer studies, the GO dispersion was prepared without a binder and drop casted on to well-polished GCE.

4.2.3 Electrochemical reduction

In order to compare the reduction capability of graphene oxide prepared from different graphite samples, electrochemical reduction was performed. Electrochemical reduction was performed in a 0.1 M phosphate buffer at pH 7.4 through a constant potential method. The graphene oxide- modified glassy carbon electrode was subjected to -1.2 V for 900 s. The electrode was then dipped in water and employed for further analysis; this was denoted as reduced graphene oxide (RGO). During the reduction, the surface functional groups were reduced and the conductivity of GO was improved. A portion of the sp^2 carbon was restored from the sp^3 defects [24].

4.3   Surface morphology

The morphology of the four graphene oxides, namely, SA 325-GO, AA 325-GO, ZEN-378 GO, and ZEN 915-GO are shown in Figure 4.2. All of the GO samples had a crumpled layered structure, which is representative of functionalized and exfoliated GO. ZEN 915-GO was effectively oxidized compared to ZEN 378-GO, AA 325-GO, and SA 325-GO which may be inferred from their fine sheet structures. Wrinkle and edge densities has been shown to increase in highly oxidized graphene oxide sheets [25,26]. Hence, the intensity of the folds/crumples may be directly related to oxidation. Intensity of the folds and wrinkles were high in ZEN GOs, in contrast to SA 325-GO and AA 325-GO.
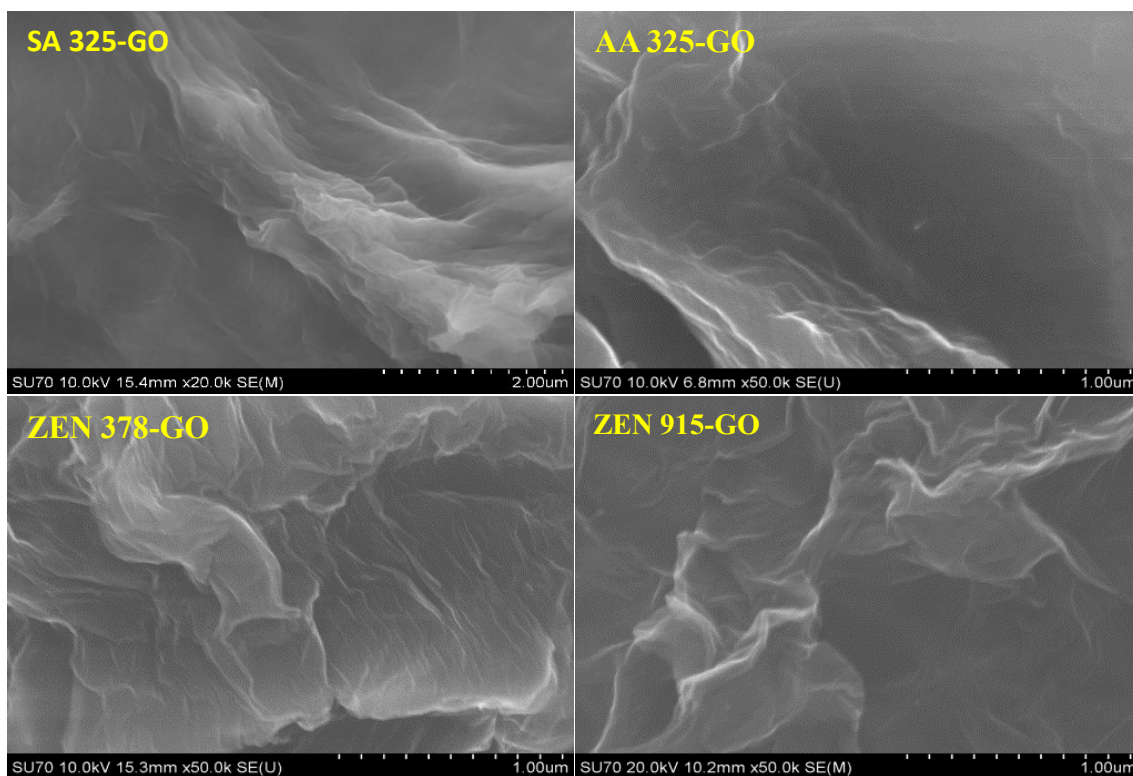
Figure 4.2 Scanning electron micrographs of GO prepared from different graphite samples.

4.4   Physiochemical characterization

4.4.1   X-ray diffraction –crystallographic study

X-ray diffractogram was used to study the structure of graphene oxide and its transformation from graphite. In Figure 4.3 X-ray diffractogram of four graphene oxide samples and the SA 325 graphite sample are shown. There are two noticeable peaks observed in the GO's diffractogram located at ~11.00° and ~42.30°. In the SA 325, the graphite XRD (0 0 2) plane observed at 26.37° was shifted to 12.15° in SA 325 GO. The characteristic graphite peak was shifted to lower 2ϴ due to the oxidation. The disappearance of the peak at 26.37° indicated complete oxidation. Peak shifting inferred an increased interlayer distance (d spacing) [26,27]. Oxygen functional groups formed during oxidation caused an increase in the d spacing. The d_{002} of SA 325 graphite was 0.3375 nm, which was enhanced to 0.7279 nm in SA 325 GO. The

interlayer spacing of GO was in the order ZEN 915-GO > ZEN 378-GO > AA 325-GO > SA 325-GO. The ZEN 915-GO sample had a wider interlayer distance, which confirmed effective oxidation.
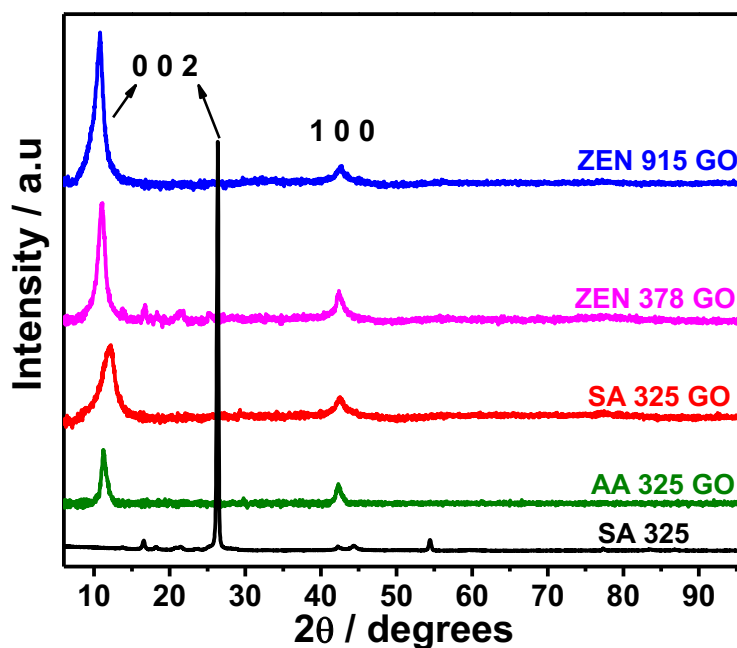
Figure 4.3 XRD patterns of GOs and SA 325 graphite.

Table 4.3 X-ray diffraction analysis comparison between graphite and GO.

Sample Name	d002 (nm)		La (nm)		Lc (nm)		N (Number of layers)	
	Graphite	GO	Graphite	GO	Graphite	GO	Graphite	GO
AA 325	0.3374	0.7866	49.95	21.51	24.30	9.93	72	13
SA 325	0.3375	0.7279	45.96	11.50	32.79	4.77	97	7
ZEN 378	0.3362	0.8030	41.17	14.26	23.12	6.94	69	9
ZEN 915	0.3366	0.8178	27.14	8.23	20.83	6.25	62	8

4.4.2 Fourier transform infra-red spectroscopy

The FTIR spectra of AA 325-GO, SA 325-GO, ZEN 378-GO, and ZEN 915-GO are shown in Figure 4.4, with the spectrum of SA 325 graphite included for comparison. It is observable from the figure that graphite does not show any features, whereas GO shows peaks that correspond to different oxygen functional groups. Functional groups were identified from their bond stretching and bending vibration characteristics. The FTIR spectra of all four GO had similar patterns. The broad peak at $\sim$3400 cm^{-1} was due to the O-H stretching vibration, whereas the next peak, at $\sim$1726 cm^{-1} was the result of the C=O stretching vibration. Close to the C=O vibration another peak was observed near 1600 cm^{-1}, which was attributed to sp^2 hybridized C=C bonding. Next to that a hump, seen at $\sim$1375-1400 cm^{-1}, matched with the O-H deformation vibration from the C-OH group. Next were two combined peaks observed proximate to 1226 cm^{-1} and 1050 cm^{-1}, which were attributed to C-O-C stretching and C-O stretching vibrations, respectively [27,28].

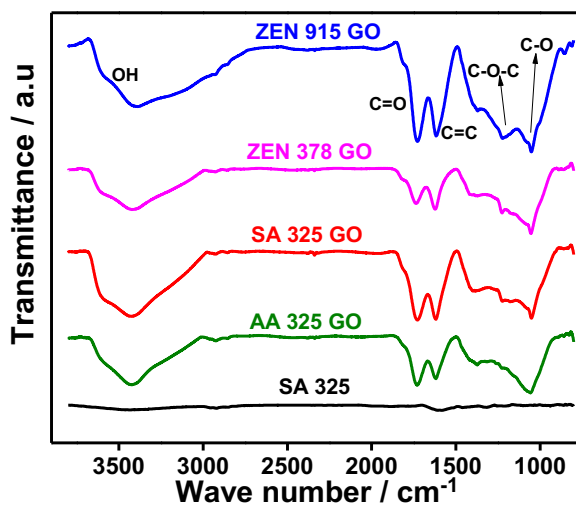**Figure 4.4** FTIR spectra of GOs and SA 325 graphite.

Although all GO samples had similar patterns, the ZEN 915 GO sample showed relatively intense peaks compared to the other three samples, which were attributed to effective oxidation.

In AA325GO alcoxy (C-O-C) peak was not distinctly pronounced. The AA325GO sample showed relatively less functionalization than the remaining three GO samples.

4.4.3 Raman spectroscopy

The Raman spectra of all GO samples were compared with SA 325 graphite in Figure 4.5. The Raman spectra showed two characteristic peaks, namely, the D band at ~1340 cm^{-1} and the G band at ~1580 cm^{-1}. The D band corresponds to scattering derived from defects/disorder in structure (i.e. sp^3 carbon atoms), whereas the G band corresponds to scattering from sp^2 hybridized carbon atoms. The GO samples showed an intense D band compared to graphite. The SA325 graphite G band is located at 1566 cm^{-1}, whereas the G band of the GO samples shifted toward a higher wave number than graphite. The corresponding D and G bands wavenumbers and I_d/I_g ratio are displayed in Table 4.4. The extent of disorder may be compared from the I_d/I_g ratio. Unlike graphite, the I_d/I_g ratio trend was slightly different for the GO samples (i.e. ZEN 378-GO > AA 325-GO > ZEN 915-GO > SA 325-GO). The ZEN 915-GO sample had a relatively lower defect density, which might be understood from the crystallite size of its starting graphite. The ZEN 915 graphite had a smaller crystallite size; hence, it did not undergo excessive damage based on the defect density of ZEN 915 GO, as the feature of this synthesis is that minimal disorder was imparted to the basal planes. Another noticeable feature in the Raman spectra of graphite is the 2D band observed at ~2700 cm^{-1}. Following oxidation, the 2D band disappeared in the GO samples[18,27]. It is noteworthy that the SA 325-GO sample had a residual 2D band compared to other GOs. This indicated an incomplete oxidation in the case of the SA 325-GO sample. Thus, Raman spectra provides useful information toward understanding and relating GO and graphite. Furthermore, broader D and G bands in all GOs may be implicit, in that disorder was caused due to the harsh oxidative process.
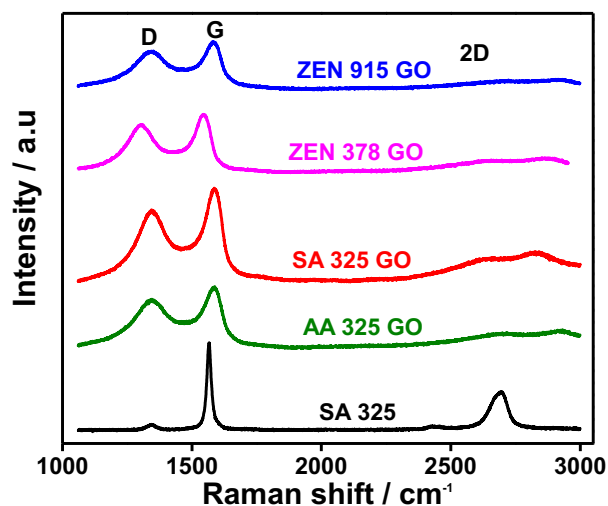
Figure 4.5 Raman spectra of GO and SA 325 graphite samples.

Table 4.4 I_d/I_g ratio comparison of graphite and GO.

Sample Name	Id/Ig		La (nm)	
	Graphite	GO	Graphite	GO
AA 325	0.23	0.80	71.62	20.76
SA 325	0.06	0.76	280.62	21.73
ZEN 378	0.09	0.82	191.09	20.28
ZEN 915	0.10	0.79	193.48	20.87

4.5 Electrochemical characterization

In order to understand the electrochemistry of graphene oxide that was prepared from the four different graphite samples the following study was conducted. Firstly, cyclic voltammetry was performed to understand the electrochemical activity of graphene oxide and reduced graphene oxide. Then the specific capacitance of reduced graphene oxide was determined through a

galvanostatic method. Subsequently, the heterogeneous electron transfer properties were investigated for GO and RGO using a potassium ferricyanide standard redox probe. A full range CV was then performed to compare the reduction behavior of the four different graphene oxide samples.

4.5.1 Cyclic voltammetry

A cyclic voltammogram (CV) of graphene oxide was recorded in 0.1M Phosphate buffer solution (PBS) at 7.4 pH. Figure 4.6(A) depicts the cyclic voltammograms of all the graphene oxides, SA 325 graphite and a glassy carbon electrode (GCE). The capacitance of graphene oxide from the area of the CV curves was almost same as GCE, and the capacitance of graphene oxide was smaller than SA 325 graphite. The presence of surface functional groups reduced the conductivity of the graphene oxide and therefore, a very small current was observed.
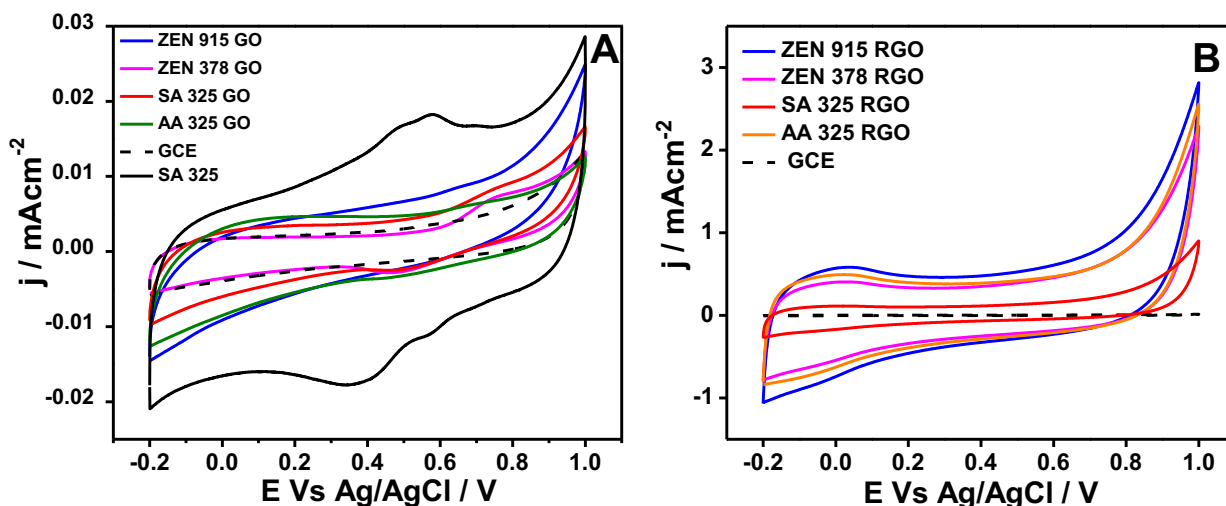
Figure 4.6 Cyclic voltammogram of (A) GOs and (B) RGOs recorded in 0.1M PBS with pH 7.4 at a scan rate of 50mV/s.

The same GO electrodes were subjected to electrochemical reduction at -1.2V for 900s in 0.1M PBS with pH 7.4. The CV response of the corresponding RGO is shown in Figure 4.6(B).

Following reduction, the current response of the CV was dramatically increased. The capacitance trend based on the CV area was revealed to be the same as for the graphite (i.e ZEN 915-GO > ZEN 378-GO = AA 325-GO > SA 325-GO). This increase in capacitance was attributed to the reduction of functional groups. The reduction of functional groups improves conductivity, which is reflected in the capacitance [15,29]. In addition, it may be noticed from the graph that RGO had a >50 times higher capacitance than did GO.

4.5.2   Specific capacitance

To accurately study the capacitance of the electrochemically reduced graphene oxide, constant current charge/discharge was performed. The constant current was determined with respect to the mass of the graphene oxide that was cast on the surface, based on 1.0 A/g. The capacitance trend was similar to the graphite (i.e. AA 325-GO > ZEN 915-GO > ZEN 378-GO > SA 325-GO). A comparison of graphite and reduced graphene oxide capacitance is shown in Table 4.5. The capacitance of graphite in 1A/g was ~10 times less than RGO. The capacitance trend was slightly different in contrast to graphite, which may have been related to the effectiveness of the oxidation. The AA 325-GO and ZEN 915-GO samples exhibited high capacitance compared to the ZEN 378-GO and SA 325-GO samples. SA 325-GO had the lowest capacitance which was due to insufficient oxidation. The SA 325 graphite was less active due to its larger crystallite size, thus it yielded relatively less interlayer distance and lower defect density in SA 325-GO. This was due to less active graphite undergoing less oxidation. From this it may be inferred that the density of functionalization was lower; hence, it was relatively inactive compared to other the GO samples. The ZEN 915-GO sample had a larger interlayer distance and relatively smaller crystallite size, which were associated with high capacitance. The capacitance values were similar as compared to those reported in the literature (10.9 F/g) [30].
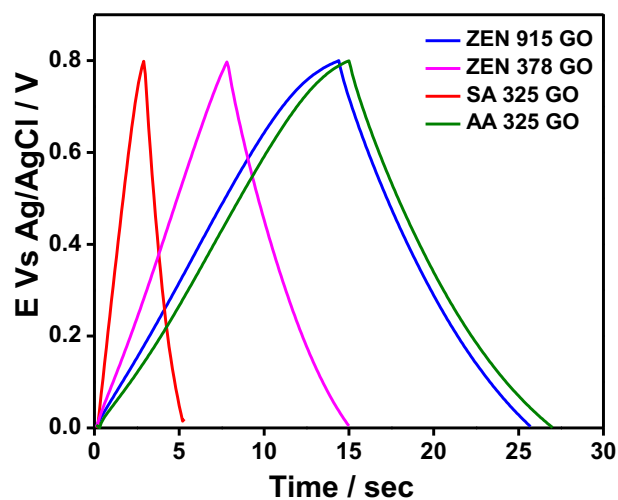
Figure 4.7 Specific capacitance of RGO recorded in 0.1M PBS with pH 7.4 at discharge current of 1.0A/g.

Table 4.5 Capacitance of graphite and RGO at 1.0 A/g.

Sample	Graphite F/g	RGO F/g
ZEN 915	1.00	14.25
ZEN 378	1.30	9.00
AA 325	0.90	15.00
SA 325	0.30	3.00

4.5.3   Heterogeneous electron transfer kinetics

Heterogeneous electron transfer studies were conducted using a 5 mM potassium ferricyanide redox couple in a 0.1M potassium chloride solution via cyclic voltammetry and electrochemical impedance measurements. Figure 4.7(A) depicts the cyclic voltammetry response of the graphene oxide samples and a glassy carbon electrode. It may be seen that a pair of redox peaks corresponded to $[Fe(CN)_6]^{3-/4-}$ in the conversion of ferri/ferro cyanide. The cyclic voltammogram

began from +0.6V as initially, the solution contained $[Fe(CN)_6]^{3-}$, which was reduced to $[Fe(CN)_6]^{4-}$, leading to a peak in the negative direction (Fe^{3+} to Fe^{2+}). Subsequently, in reverse direction, from -0.2V to +0.6V; $[Fe(CN)_6]^{4-}$ it was oxidized to $[Fe(CN)_6]^{3-}$, which corresponded to the transition from Fe^{2+} to Fe^{3+}. This reaction caused the emergence of a peak in the positive
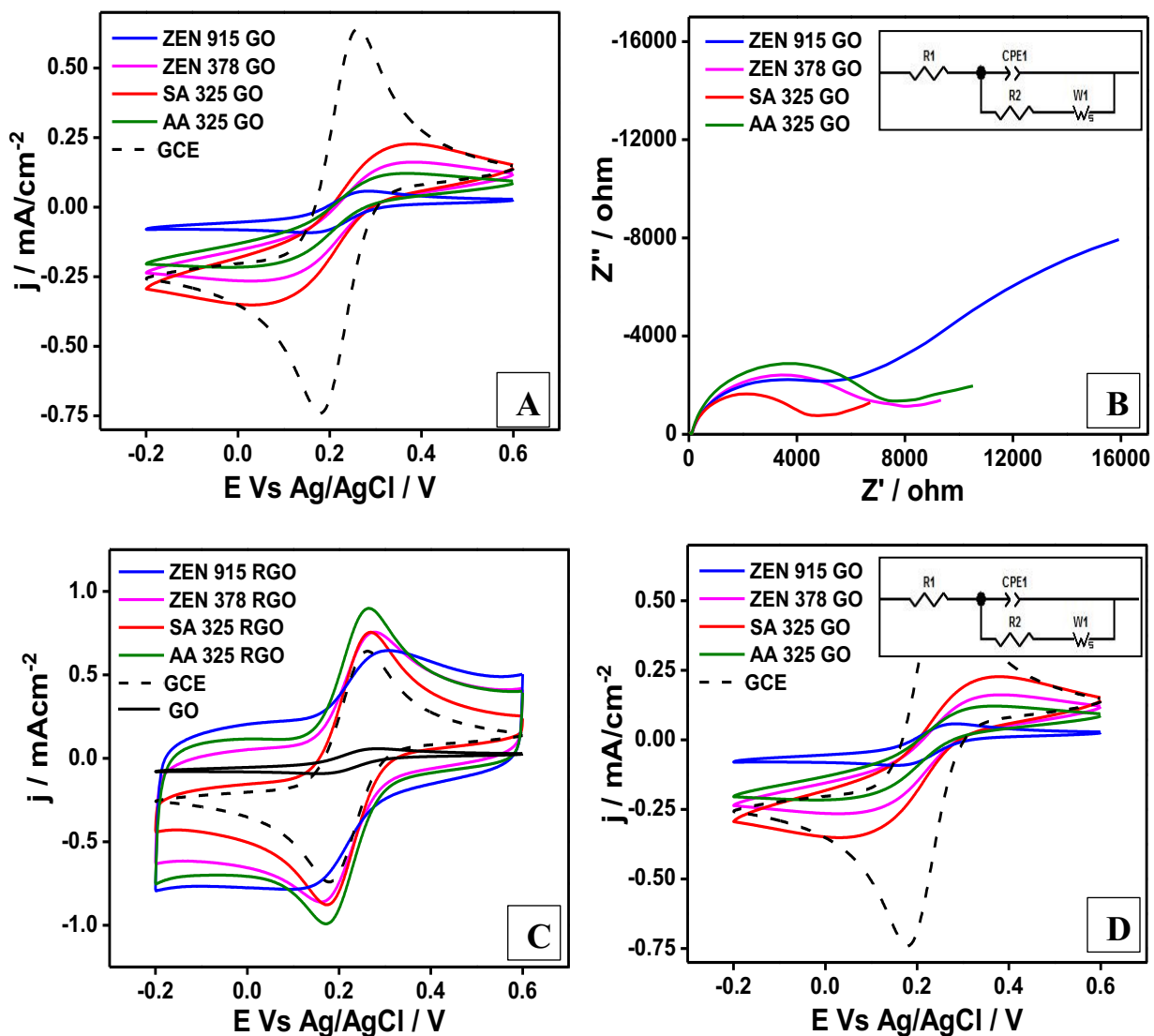
Figure 4.8 Cyclic voltammogram of potassium ferricyanide(5 mM) redox couple at a scan rate of 50 mV/s and electrochemical impedance spectrum recorded in 0.1M KCl for GO (A) & (B) and RGO (C) & (D). EIS equivalent circuits depicted at inset.

direction. Cyclic reduction and oxidation reactions occur corresponding to one electron transfer in each direction. For GCE, the redox peaks were sharp with equal current density on both sides, which indicated more rapid electron transfer.

In GO, all samples exhibited broad redox peaks, which was due to the repulsion of the $[Fe(CN)_6]^{3-/4-}$ from the surface, as the GO surface was also negatively charged. This electrostatic repulsion and the poor conductivity was due to the presence of oxygen functional groups, which slowed the electron transfer [29]. The potential difference between the redox peaks (ΔEp) for GCE was 83 mV, which corresponds to a quasi-reversible system [31]. A large ΔEp indicates slower electron transfer, whereas a narrow ΔEp relates to fast electron transfer. The ΔEp of all four graphene oxide samples are displayed in Table 4.6. Although the ZEN 915-GO sample showed a narrow potential difference, the corresponding current density was negligible. This response was due to the substrate GCE via thin layer diffusion. The trend of the ΔEp of remaining GO samples was, AA 325-GO > ZEN 378-GO = SA 325-GO. These electrodes were subjected to electrochemical impedance analysis by applying a 10 mV AC amplitude at $E_{1/2}$ [$E_{1/2}$ = (Eo+Er)/2] DC potential in the 0.1 Hz to 10^6 Hz frequency range. Information related to the electrode-electrolyte interface can be understood with the EIS responses of the GO samples displayed in Figure 4.7(B). This assists with distinguishing the GO samples more quantitatively. Charge transfer resistance (Rct) may be noted from the intercept of the semicircle observed in the EIS response. The lower resistance end relates to a high frequency range and vice versa. Inset of Figure 4.8(C) and (D) shows the equivalent circuit for the corresponding EIS response. From the EIS response, various resistances associated with the electrochemical cell and double layer capacitive behavior of the electrode may be understood. The intercept of the curve at the high frequency range is the sum of the resistances (Rs) from the electrode material, the contact

resistance of the connections, and the electrolyte resistance. Subsequently, the intercept of the semicircle at low frequency range, which differed from Rs, was attributed to the charge transfer resistance [32]. The observed charge transfer resistance (Rct) was consistent with the ΔEp in the CV. The trend of the Rct was AA 325-GO > ZEN 915-GO > ZEN 378-GO > SA 325-GO. The higher Rct may be directly related to the functional groups density, that is, a higher functional group density will initiate more resistance [18]. From these results, the resistance of the ZEN 915-GO found to be similar to the other samples. Furthermore the SA 325-GO sample exhibited a lower resistance, which may be understood in terms of it having a lower defect density and lower population of functional groups.

Table 4.6 Heterogeneous electron transfer study, ΔEp, Rs and Rct of GO and RGO samples.

Sample Name	*GO* ΔEp (mV)	*RGO* ΔEp (mV)	*GO* Rs (Ω)	Rct (Ω)	*RGO* Rs (Ω)	Rct (Ω)
AA 325	253	90	89.7	7095	10.0	97.8
SA 325	249	93	86.4	4248	10.9	91.3
ZEN 378	247	116	90.0	6646	13.9	113.5
ZEN 915	91	165	88.2	6063	16.2	128.4

Subsequently, the RGO's ferri/ferro cyanide response and EIS were studied in order to compare them with the GO sample responses. The RGOs had a conductive surface and showed a higher capacitance than the GO. The ferri/ferro cyanide CV response of the RGOs is shown in Figure 4.7(C). Sharp peaks in the CV responses corresponded to facile electron transfer as well as higher capacitance current, which was also noticeable from the CV curves. The ΔEp corresponding to each RGO is illustrated in Table 4.6. The trend in ΔEp of RGOs was ZEN 915-

RGO > ZEN 378-RGO > AA 325-RGO > SA 325-RGO. The ZEN 915-GO sample had a wider

ΔEp, which may be related to residual functional groups causing resistance. The SA 325-RGO

sample exhibited facile electron transfer, which was consistent with previous observations.

Improved electron transfer in the RGOs in contrast to GO was due to improved conductivity and

enhanced π conjugation (sp^2) [33].

Figure 4.7(D) illustrates the corresponding EIS responses of the RGOs. The trend of the

charge transfer determined was consistent with the CV response (i.e., ZEN 915-RGO > ZEN

378-RGO > AA 325-RGO > SA 325-RGO). An equivalent circuit was fitted using Z View

software, depicted in the inset of the EIS graphs, and was similar to that of GO. The Rs values of

GO and RGO are shown in Table 4.6, and it was large for GO due to a high intrinsic resistance in

response to the presence of functional groups. For the RGOs, the Rs was ~10 Ω, which was

primarily due to the electrolyte resistance, as the conductivity was improved following reduction.

Warburg region is observed after the semi-circle in the EIS responses (Figure 4.8(B) & (D)). In

addition, the Warburg region was well pronounced in the RGOs, and from the angle of the

Warburg line, the double layer capacitance of the electrode may be inferred. The Warburg line of

the ZEN 915-RGO sample shifted toward 90°, which indicated that its double layer capacitance

was higher than the other three samples.

4.5.4   *Full range cyclic voltammetry*

To understand the GO reduction pattern the full range cyclic voltammetry was investigated.

Full range CV was performed for GO-modified GCE in a deaerated 0.1M phosphate buffer with

7.4 pH at 50 mV/s. The CV was performed from an initial potential of 0.0V toward the negative

direction, up to -2.0 V, and from there, in positive direction, up to 1.8V. Initial voltage and the

potential window were chosen based on the available literature. The potential range selected was

wider (-2.0V to +1.8 V) to accompany the entire redox feature of GO within it. Figure 4.9(A) displays the first cycle of the full range CV of all the GO samples, and the inset depicts the full range CV of the SA 325 graphite. The CV of SA 325 graphite did not exhibit any significant redox features and the stable potential range was -0.5 to +1.4 V. The GO samples had a wider stable potential window than did graphite, at ~ -1.5 to +1.5 V. In contrast, all of the GO samples showed redox features in the CV, which was ascribed to the functional groups that were present. The amount of functional groups may be directly related to its peak current density.
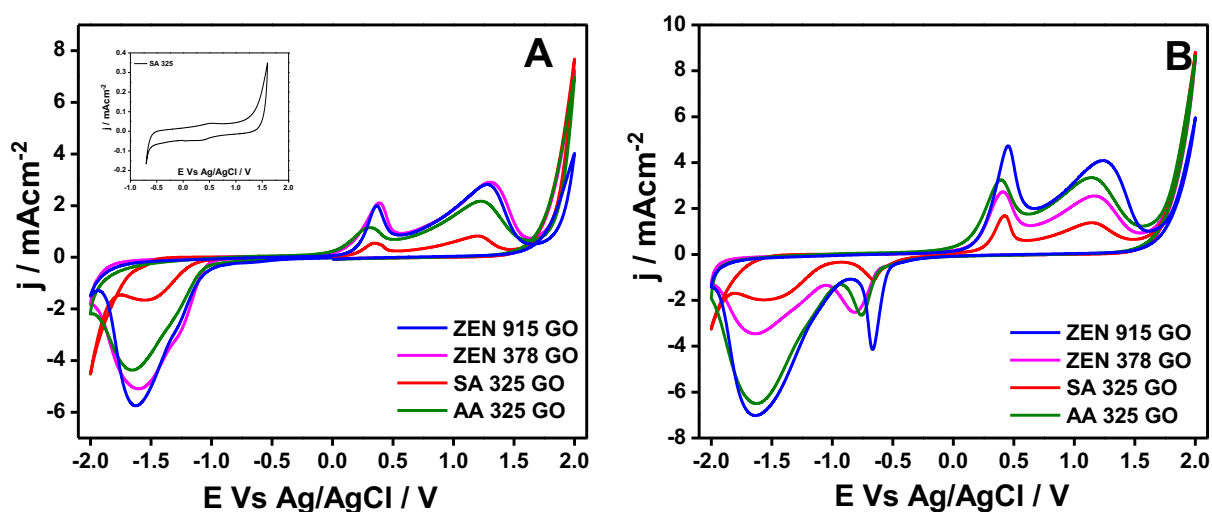
Figure 4.9 Full range cyclic voltammetry of GO recorded in 0.1M PBS with pH 7.4 at a scan rate of 50 mV/s (A) Cycle-1 (inset: SA 325 graphite full range CV) and (B) Cycle-2.

In the first cycle a large peak was observed at ~ -1.5 V, with its onset at 1.0 V. This corresponded to aldehyde (-1.0 V) and epoxyl (-1.5 V) functional groups [34, 35]. The onset potential for the SA 325-GO sample was 100 mV negative, compared to other three GO samples. This might have been due to the lower proportion of aldehyde functional groups (-1.0V). The peak intensity of the reduction peak was high at -1.5, which indicated a higher proportion of carbonyl functional groups. All of the GO samples showed reversible behavior that is,

corresponding oxidation was observed under the positive potential, which is characteristic of permanganate oxidized GO. The oxidation peak was observed at ~ 0.30-0.40V followed by a broad peak, which was observed near 1.25-1.30 V for all of the GO samples.

Figure 4.9(B) illustrates the 2nd cycle of the full range CV. Interestingly, unlike the Hummer's method, the redox peaks were not weakened in the 2nd cycle, which was characteristic of the improved Hummers' GO. In fact, the peak currents were increased compared to the first cycle. Another interesting observation was a new sharp reduction peak at ~ -0.65 to -0.80V. This reduction peak was the result of oxidized species at 1.25-1.30 V as reported in the literature [36]. Furthermore, the activation of this peak (-0.6 to -0.80 V) was linked to the initial reduction, from -1.0 to -1.5 V. Furthermore, the ZEN 378-GO sample had diminished peak intensity in the 2nd cycle, which corresponded to presence of irreversible functional moieties. The trend based on the area of the full range CV was consistent with previous observations, (i.e., ZEN 915-GO >/= AA 325-GO > ZEN 378-GO > SA 325-GO). These observations suggested that the ZEN 915-GO sample had relatively more functionalized groups in comparison to the other three samples, which was consistent with other characteristic observations.

4.6 Summary

As a continuation of the previous chapter, graphene oxide was synthesized using an improved Hummer's method from four different graphite samples. To understand the influence of graphite in the preparation of graphene oxide derivatives, the properties of graphene oxide were studied, and the results were related to the characteristics of graphite. Summary of the characterization results of graphene oxide prepared from different graphites were depicted in the Table 4.7. The morphology of all four GOs appeared alike, with a wrinkled layered structure. It is also worth noting that the ZEN 915-GO sample exhibited fine exfoliated GO sheets, which were due to the

smaller size sheets in the ZEN 915 graphite sample. XRD confirmed the complete oxidation of graphite and showed a wider interlayer spacing for the ZEN 915-GO sample, which correlated to the smaller crystallite size of the ZEN 915 graphite sample, which underwent effective functionalization. The presence of functional groups in the GO sample was confirmed by FTIR spectra, and similar types of functional groups were observed in all four samples. The Raman spectra of the GO samples showed an enhanced D band, which was associated with the oxidation and enhanced proportion of the sp^3 hybridized carbon atoms. The ZEN 915-GO sample had fewer defects in contrast to the other samples; this was supportive of the smaller starting graphite and oxidizer selected. The electrochemistry of the GO samples was investigated with three motives, namely, to understand the specific capacitance, the electron transfer properties, and the reduction pattern. All of the GO samples showed smaller capacitance, which was enhanced significantly after being subjected to electrochemical reduction. The capacitance of the GO samples was smaller than graphite due to presence of functional groups and high resistance. The specific capacitance of RGO was gauged by the galvanostatic method, and in support of other characteristic observations the ZEN 915-GO sample exhibited high capacitance. The trend of capacitance was the same as that observed for the graphite samples (i.e., AA 325-GO = ZEN 915-GO > ZEN 378-GO > SA 325-GO). However, the heterogeneous electron transfer ability of GO was slower compared to RGO, which was due to the improved conductivity and restored sp^2 carbon atoms. The ZEN 915-GO and ZEN 378-GO samples had relatively high resistance in contrast to the AA 325-GO and SA 325-GO samples, which might have been caused by residual functional groups. Further to this was that the reduction pattern showed an identical trend, as was observed for the capacitance. The intensity of functional groups was high in the ZEN 915-GO sample and the composition of the functional groups was similar in all of GO samples. Therefore,

the estimates based on the characteristics of the graphite were observed experimentally. These analyses support the premise that graphite attributes have a considerable influence on the properties of graphene oxide.

Table 4.7. Comparison of properties of graphene oxide obtained from different graphite.

Parameter	*Superior*	*Trend*	*Inferior*
Interlayer distance	**Wider**	ZEN 915-GO > ZEN 378-GO > AA 325-GO > SA 325-GO	**Narrower**
Sheet size (La)	**Smaller**	ZEN 915-GO < SA 325-GO < ZEN 378-GO < AA 325-GO	**Bigger**
Number of Layers	**Fewer**	SA 325-GO < ZEN 915-GO < ZEN 378-GO < AA 325-GO	**More**
I_d/I_g **ratio**	**Fewer**	SA 325-GO < ZEN 915-GO < AA 325-GO < ZEN 378-GO	**Large**
Specific Capacitance	**High**	ZEN 915-GO> AA 325-GO > ZEN 378-GO > SA 325-GO	**Low**
Heterogeneous electron transfer ΔEp	**Faster**	AA 325-GO < SA 325-GO < ZEN 378-GO < ZEN 915-GO	**Slower**

References

[1]   K.S. Novoselov, Electric Field Effect in Atomically Thin Carbon Films, *Science* 306 (**2004**) 666–669.

[2]   B.C. Brodie, On the Atomic Weight of Graphite, *Philosophical Transactions of the Royal Society of London* 149 (**1859**) 249–259.

[3]   L. Staudenmaier, Verfahren zur Darstellung der Graphitsäure, *Berichte Der Deutschen Chemischen Gesellschaft* 31 (**1898**) 1481–1487.

[4]   U. Hofmann, E. König, Untersuchungen uber Graphitoxyd, *Zeitschrift Fur Anorganische Und Allgemeine Chemie* 234 (**1937**) 311–336.

[5]   J. William S. Hummers, R.E. Offeman, Preparation of Graphitic Oxide, *Journal of the American Chemical Society* 80 (**1958**) 1339.

[6]   D.C. Marcano, D. V. Kosynkin, J.M. Berlin, A. Sinitskii, Z. Sun, A. Slesarev, L.B. Alemany, W. Lu, J.M. Tour, Improved Synthesis of Graphene Oxide, *ACS Nano* 4 (**2010**) 4806–4814.

[7]   C. Botas, P. Álvarez, P. Blanco, M. Granda, C. Blanco, R. Santamaría, L.J. Romasanta, R. Verdejo, M.A. López-Manchado, R. Menéndez, Graphene materials with different structures prepared from the same graphite by the Hummers and Brodie methods, *Carbon* 65 (**2013**) 156–164.

[8]   S. Eigler, M. Enzelberger-Heim, S. Grimm, P. Hofmann, W. Kroener, A. Geworski, C. Dotzer, M. Röckert, J. Xiao, C. Papp, O. Lytken, H.P. Steinrück, P. Müller, A. Hirsch, Wet chemical synthesis of graphene, *Advanced Materials* 25 (**2013**) 3583–3587.

[9]   L. Peng, Z. Xu, Z. Liu, Y. Wei, H. Sun, Z. Li, X. Zhao, C. Gao, An iron-based green approach to 1-h production of single-layer graphene oxide, *Nature Communications* 6 (**2015**) 5716.

[10]   A. Lerf, H. He, M. Forster, J. Klinowski, Structure of Graphite Oxide Revisited, *Journal of Physical Chemistry B* 102 (**1998**) 4477–4482.

[11]   D. Chen, H. Feng, J. Li, Graphene oxide: Preparation, functionalization, and electrochemical applications, *Chemical Reviews* 112 (**2012**) 6027–6053.

[12]   S. Eigler, S. Grimm, F. Hof, A. Hirsch, Graphene oxide: a stable carbon framework for functionalization, *Journal of Materials Chemistry A* 1 (**2013**) 11559.

[13]   Y. Sun, S. Yang, C. Ding, Z. Jin, W. Cheng, Tuning the chemistry of graphene oxides by a sonochemical approach: Application of adsorption properties, *RSC Advances* 5 (**2015**) 24886–24892.

[14]   D.W. Lee, J.W. Seo, Sp2/sp3 carbon ratio in graphite oxide with different preparation times, *Journal of Physical Chemistry C* 115 (**2011**) 2705–2708.

[15]   N. Morimoto, T. Kubo, Y. Nishina, Tailoring the Oxygen Content of Graphite and Reduced Graphene Oxide for Specific Applications, *Scientific Reports* 6 (**2016**) 21715.

[16]   J.G.S. Moo, B. Khezri, R.D. Webster, M. Pumera, Graphene Oxides Prepared by Hummers', Hofmann's, and Staudenmaier's Methods: Dramatic Influences on Heavy-Metal-Ion Adsorption, *ChemPhysChem* 15 (**2014**) 2922–2929.

[17]   H.L. Poh, F. Šaněk, A. Ambrosi, G. Zhao, Z. Sofer, M. Pumera, Graphenes prepared by Staudenmaier, Hofmann and Hummers methods with consequent thermal exfoliation exhibit very different electrochemical properties, *Nanoscale* 4 (**2012**) 3515.

[18]   C.K. Chua, Z. Sofer, M. Pumera, Graphite oxides: Effects of permanganate and chlorate oxidants on the oxygen composition, *Chemistry - A European Journal* 18 (**2012**) 13453–13459.

[19] M.R. Karim, M.S. Islam, K. Hatakeyama, M. Nakamura, R. Ohtani, M. Koinuma, S. Hayami, Effect of Interlayer Distance and Oxygen Content on Proton Conductivity of Graphite Oxide, *The Journal of Physical Chemistry C* 120 (**2016**) 21976–21982.

[20] M.H. Tran, C.S. Yang, S. Yang, I.J. Kim, H.K. Jeong, Influence of graphite size on the synthesis and reduction of graphite oxides, *Current Applied Physics* 14 (**2014**) S74–S79.

[21] H.. Yu, K.. Xie, J.. Hu, C.. Shen, J.-G.. Wang, B.. b Wei, The importance of raw graphite size to the capacitive properties of graphene oxide, *RSC Advances* 6 (**2016**) 17023–17028.

[22] Z.-L. Chen, F.-Y. Kam, R.G.-S. Goh, J. Song, G.-K. Lim, L.-L. Chua, Influence of Graphite Source on Chemical Oxidative Reactivity, *Chemistry of Materials* 25 (**2013**) 2944–2949.

[23] J. Bai, H. Sun, X. Yin, X. Yin, S. Wang, A.E. Creamer, L. Xu, Z. Qin, F. He, B. Gao, Oxygen-Content-Controllable Graphene Oxide from Electron-Beam-Irradiated Graphite: Synthesis, Characterization, and Removal of Aqueous Lead [Pb(II)], *ACS Applied Materials & Interfaces* 8 (**2016**) 25289–25296.

[24] A. Ambrosi, M. Pumera, Precise tuning of surface composition and electron-transfer properties of graphene oxide films through electroreduction, *Chemistry - A European Journal* 19 (**2013**) 4748–4753.

[25] A.M. Pinto, C. Gonçalves, D.M. Sousa, A.R. Ferreira, J.A. Moreira, I.C. Gonçalves, F.D. Magalhães, Smaller particle size and higher oxidation improves biocompatibility of graphene-based materials, *Carbon* 99 (**2016**) 318–329.

[26] M.R. Karim, M.S. Islam, K. Hatakeyama, M. Nakamura, R. Ohtani, M. Koinuma, S. Hayami, Effect of Interlayer Distance and Oxygen Content on Proton Conductivity of Graphite Oxide, *The Journal of Physical Chemistry C* 120 (**2016**) 21976–21982.

[27] M.M. Kadam, O.R. Lokare, K.V.M.K. Kireeti, V.G. Gaikar, N. Jha, Impact of the degree of functionalization of graphene oxide on the electrochemical charge storage property and metal ion adsorption, *RSC Advances* 4 (**2014**) 62737–62745.

[28] N. Wu, X. She, D. Yang, X. Wu, F. Su, Y. Chen, Synthesis of network reduced graphene oxide in polystyrene matrix by a two-step reduction method for superior conductivity of the composite, *Journal of Materials Chemistry* 22 (**2012**) 17254–17261.

[29] A. Ambrosi, M. Pumera, Precise tuning of surface composition and electron-transfer properties of graphene oxide films through electroreduction, *Chemistry - A European Journal* 19 (**2013**) 4748–4753.

[30] S. Chen, J. Zhu, X. Wu, Q. Han, X. Wang, Graphene oxide-Mno2 nanocomposites for supercapacitors, *ACS Nano* 4 (**2010**) 2822–2830.

[31] A.J. Bard, L.R. Faulkner, Electrochemical Methods Fundamentals and Applications, **1944**.

[32] B. Xu, S. Yue, Z. Sui, X. Zhang, S. Hou, G. Cao, Y. Yang, What is the choice for supercapacitors: graphene or graphene oxide?, *Energy & Environmental Science* 4 (**2011**) 2826.

[33] M. Gao, Y. Xu, X. Wang, Y. Sang, S. Wang, Analysis of Electrochemical Reduction Process of Graphene Oxide and its Electrochemical Behavior, *Electroanalysis* 28 (**2016**) 1377–1382.

[34] A.P. Doherty, C.A. Brooks, Electrosynthesis in room-temperature ionic liquids: Benzaldehyde reduction, *Electrochimica Acta* 49 (**2004**) 3821–3826.

[35] L. Xiao, G.G. Wildgoose, A. Crossley, R.G. Compton, The electroreduction of "C60" films in aqueous electrolyte does not lead to alkali metal ion insertion-Evidence for the involvement of adventitious poly-epoxidated C60 (C60On), *Sensors and Actuators, B: Chemical* 138 (**2009**) 397–401.

[36] A.Y.S. Eng, A. Ambrosi, C.K. Chua, F. Šaněk, Z. Sofer, M. Pumera, Unusual Inherent Electrochemistry of Graphene Oxides Prepared Using Permanganate Oxidants, *Chemistry - A European Journal* 19 (**2013**) 12673–12683.

Chapter V

One pot synthesis of fluorinated graphene oxide for heavy metal ion sensing and electrochemical capacitor applications

5.1 Introduction

The functionalization and doping of graphene has been explored in order to optimize the resulting material properties. Functionalization alters the dispersion, orientation, interaction, and electronic properties of graphene derivatives. Various types of functionalization have been reported for graphene such as metal nanoparticles decorated graphene, graphene-metal oxide nanocomposites, heteroatoms doped graphene, and halogens doped graphene, etc. [1–4]. Halogen atoms exhibit dual characteristics: one is electron-withdrawing, which arises from electronegativity, whereas the other is electron donating, which emerges due to the presence of lone-pair electrons. The electronic structure of graphene may be significantly altered, contingent on the type of halogen atom dopant. The electrical resistivity of halogen-doped graphene decreases with the increased size of the halogen (decrease in electronegativity) [5]. Among halogenated graphene, fluorinated graphene has gleaned much attention because of its unique properties, including a wide bandgap and high room temperature resistance [6,7]. Fluorine has a higher electronegativity than carbon; hence, it exhibits different ionic, semi-ionic, and covalent, bonding characteristics, and the nature of C-F bonding varies with respect to the fluorination levels [8]. Hydrophobicity is increased by C-F bonds due to low surface energy [9]. Various synthesis techniques have been reported for the synthesis of fluorinated graphene, such as direct gas fluorination, plasma fluorination, hydrothermal fluorination, photochemical, electrochemical, sono-chemical fluorination, modified Hummer's exfoliation, and thermal exfoliation. The present methods for the preparation of fluorinated graphene derivatives require high temperatures, high pressure, multiple steps, and expensive instruments [7,8,10]. Hence, there is a need to develop

facile methods. The effects of trace levels of fluorine content have been scarcely explored [11]. In the present method, FGO was synthesized from graphite using a rapid one step process. Fluorographene derivatives have been explored for a variety of applications, such as in anode materials for batteries [12,13], bio applications [14], capacitors [15], catalysts [5], and more. In this context two applications for the prepared fluorinated graphene oxide were demonstrated.

Metals with a specific gravity of >5.0 g.cm^{-3} are referred to as heavy metals which are serious pollutants that pose a threat to human health and the ambient environment. Hence, intense efforts have been invested toward the development of sensors for the detection of ultralow concentrations of heavy metal ions. The sources of these pollutants are primarily wastewater from the mining and steel industries. Therefore, it is essential to monitor the levels of heavy metal ions in both wastewater streams and ambient waterways. Graphene based sensors including nitrogen doped graphene [4], metal nanoparticle/graphene [1], metal oxide/graphene [16], functionalized graphene [17], conducting polymer/graphene [3], etc. have been reported. Among these sensors, very few have been reported for heavy metal ion detection via graphene based materials without functionalization. In order to acquire better sensitivity, the in situ formation of a Hg/Bi thin film on graphene was reported [18,19]. To date, fluorine doped GO has not been reported for heavy metal ion sensing. FGO may be a cost effective sensor for the detection of ultralow concentrations of heavy metal ions.

As per the analysis in chapter-IV, GO from ZEN 915 graphite has better characteristics. In this project FGO was synthesized via a one pot modified improved Hummer's method using ZEN 915 graphite. Subsequently, its surface morphology using SEM, TEM, and AFM was studied to understand its structure, morphology, and size. The crystallinity of FGO was characterized using X-ray diffraction analysis. Fluorine doping and its effects have been

investigated by X-ray photoelectron spectroscopy, Fourier transform infrared spectroscopy, and Raman spectroscopy. Further, the electrochemistry of FGO in comparison to GO was also investigated. A distinct behaviour was exhibited by FGO in comparison to GO, for heavy metal ion stripping, and this activity may be traced due to the presence of fluorine. Based on the comparison of electrochemical characteristics, it was revealed that FGO possessed a large quantity of functional groups in contrast to GO. The addition of HF introduced more defects, as well as fluorine into GO.

5.2   Experimental

5.2.1   *Synthesis of fluorinated graphene oxide*
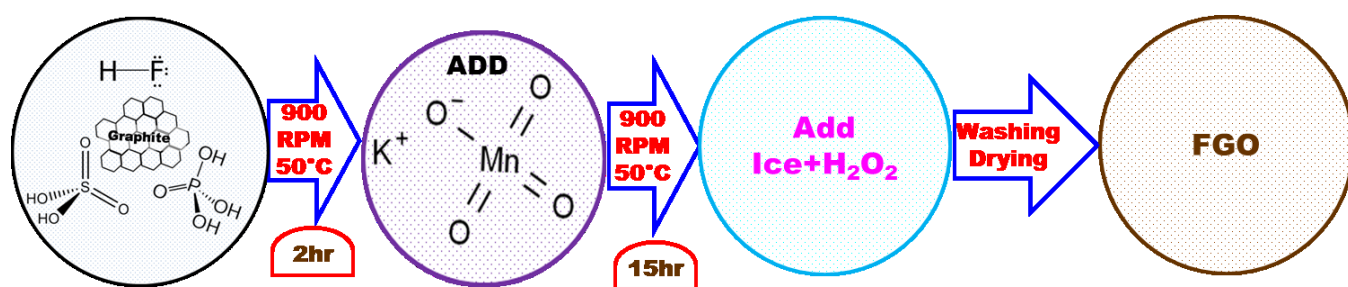
Figure 5.1 Synthesis procedure of fluorinated graphene oxide.

Graphene oxide has been synthesized by the improved Hummers' method reported elsewhere [20]. Fluorine doping was obtained by adding 20 ml of hydrofluoric acid into the reaction mixture of the improved Hummer's method. Hydrofluoric acid was added in order to enhance the density of functional groups, as well as to facilitate the doping of fluorine atoms onto the graphene oxide. A scheme showing the FGO synthesis procedure is shown in Figure 5.1. In a typical synthesis, 1 g of graphite was vigorously stirred (900 RPM) in a mixture of concentrated sulfuric acid, 85% phosphoric acid (9:1; 90 ml :10 ml), and 20 ml of HF. A polypropylene container was used for the synthesis as HF will corrode a glass container. Following 2 hours of vigorous mixing at 50°C, 4.5g of $KMnO_4$ was slowly added over 5 minutes, as the addition of

106

$KMnO_4$ increases the temperature. Subsequently, the reaction mixture was stirred vigorously for over 15 hours, which turned the mixture to a brown colour. The reaction mixture was then poured onto ice and 5 ml 30% hydrogen peroxide was added to the mixture to complete the oxidation of excess $KMnO_4$ and the exfoliation of the graphite oxide. The mixture was repeatedly rinsed by centrifuge in 30%HCl followed by ultrapure water (5 times), and then rinsed in ethanol and diethyl ether. Finally, the obtained yellowish brown solid was dried in an oven at <50 °C. Graphene oxide was also prepared using the same procedure without addition of HF for comparison.

5.2.2   *Electrochemical characterization*

Electrochemical experiments were carried out using a modified glassy carbon electrode with graphene oxide and fluorinated graphene oxide. A dispersion of 2.5mg/ml of GO or FGO in water was prepared by ultrasonication (Bransonic ultrasonicleaner 2510R-DTH, output 100 W) for 30 minutes. A 3 μL aliquot of the as-prepared dispersion was cast on a polished GCE and dried at room temperature for 30 minutes. Cyclic voltammetry (CV) studies were carried out in a 0.1 M phosphate buffer at pH 7.4, and capacitance studies were conducted in 0.5M H_2SO_4. Metal ion sensing experiments were conducted in a 0.1 M acetate buffer with pH 5. All cyclic voltammetry experiments done in this work used Ag/AgCl, and Pt was employed as the reference electrode and counter electrode, respectively at a scan rate of 50 mV/s.

### 5.2.3   *Metal ion stripping analysis procedure*

GO and FGO-modified GCE were subjected to pretreatment prior to metal ion sensing. The pretreatment of the electrodes proceeded in the absence of metal ions by applying a constant potential. Metal ion sensing was then carried out by following standard procedures.[4] There were three steps involved with metal ion stripping analysis; Firstly, a known quantity of metal

ion solution aliquot was added into the electrolyte for the required concentration. Secondly, metal ions were deposited by applying 0.9 V for 175 s (this step is also called the adsorption step). During deposition, the solution was continuously stirred at a constant speed in order to assist the diffusion process. And thirdly, the stripping was conducted using square wave anodic stripping voltammetry (SWASV) in the -1.0 to 0.6 V vs Ag/AgCl potential range. The square wave anodic stripping voltammetry parameters used included a 4 mV increment voltage, 25mV amplitude, and 15 Hz frequency for all stripping experiments. The stripping current for each metal ion was measured from the stripping voltammogram for further analysis. Subsequent to stripping, prior to the reuse of the electrode for further sensing, the desorption of the remaining metal ions proceeded electrochemically, by applying 0.6 V vs Ag/AgCl for 200 s.

5.3 Physiochemical characterization

5.3.1 *Morphology & composition*
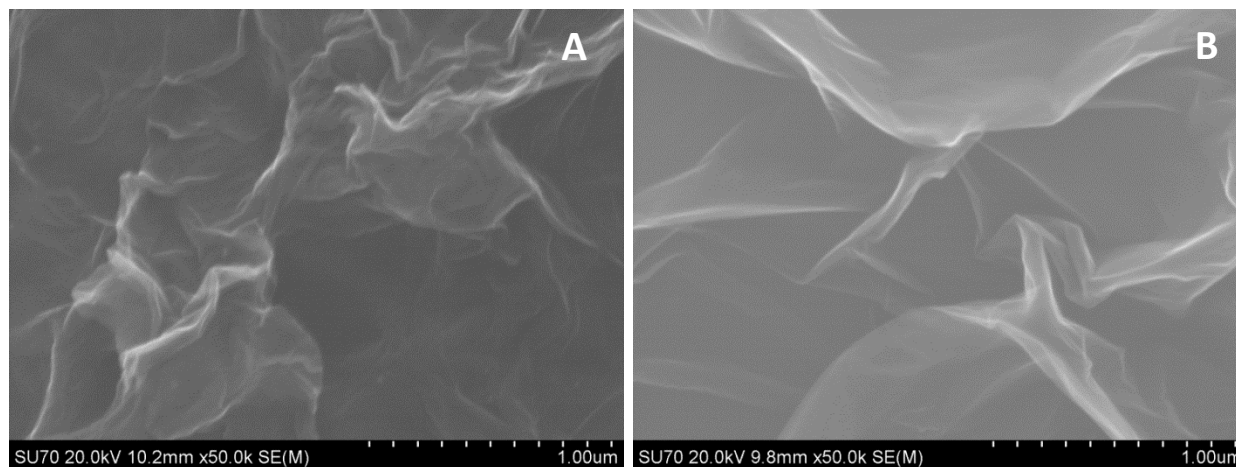
Figure 5.2 Scanning electron microscope images of (A) graphene oxide (GO), (B) fluorinated graphene oxide (FGO).

The surface morphology of GO and FGO are depicted in Figures 5.2(A) and (B), where the FGO showed a crumpled layered structure, and it may be seen that the sheets were transparent.

Crumples are due to the presence of defects and the functionalization of the graphene backbone. The morphology of the FGO was similar to GO [21], which was consistent with previous reports.

In order to confirm the existence of fluorine, elemental analysis (EDX) was performed along with SEM. The EDX spectra showed carbon oxygen and a tiny hump at ~0.68keV, which confirmed the fluorine doping (~1 at. %). The F peak was not clearly discernible as there was a very small amount which is equivalent to uncertainity of the EDX technique; hence, EDX spectrum was not included. The composition of carbon and oxygen was similar in GO and FGO, where FGO had a slightly lesser oxygen content in contrast to GO. [22].
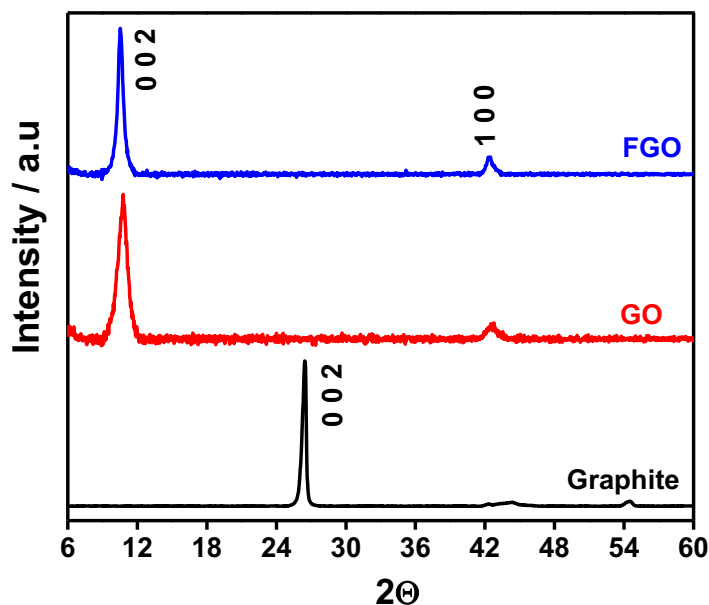
5.3.2 *X-ray diffraction*

Figure 5.3 XRD spectrum of graphite, GO and FGO.

The XRD pattern of FGO compared with GO and ZEN 915 graphite is illustrated in Figure 5.3. The graphite showed a typical response peak at ~26.42° corresponding to 0.337 nm d-spacing and crystallite size (Lc) 20.83 nm. GO and FGO has a characteristic peak at 10.81° and

10.53° and the graphitic peak at 26.46° has disappeared, which shows complete oxidation [23]. The 2ϴ of the peak corresponding to the (0 0 2) plane of the FGO was lower than that of the GO, which indicated a larger interlayer distance. Interlayer distance of GO and FGO are 0.818, 0.839 nm respectively. The interlayer distance increases due to repulsive effect due to the formation of C-F. The FGO peak was sharper and narrower compared to GO, where the narrowness of the peak indicated that the crystallite size in the c direction was higher compared to GO (i.e 6.35 and 14.96 nm respectively). FGO sheets are thicker than GO due to fluorine moieties sticking outside the layer [15]. Intensity of the characteristic peak was stronger in FGO, which indicated more potent oxidation in the case of FGO in contrast to GO. Stronger oxidation has the effect of introducing additional defects and functional groups. Another peak at ~42.32° corresponding to the (1 0 0) plane was similar as in GO; the lateral size (La) of GO and FGO are 19.25, 26.75 nm respectively.

### 5.3.3 *AFM and high resolution transmission electron microscopy (HRTEM) analysis*

The surface morphology of FGO was investigated using AFM and transmission electron microscope (TEM). From the AFM images in Figure 5.4(A) and (B), it is clear that the FGO possessed relatively smaller sheets and contained few layers. The thickness of the graphene oxide sheets from Figure 5.4(A), is ~1-1.5nm, whereas the thickness of FGO sheets measured from the Figure 5.4(B) is ~1.5 nm. This was consistent with earlier reports on the thickness of a single layer graphene oxide ~1 nm) [24]. The AFM images of FGO depicts smaller sheet sizes and additional etched surfaces compared to GO, which were due to a higher defect population in the presence of fluorine. However FGO possessed smaller lateral dimensions in contrast to GO [15].
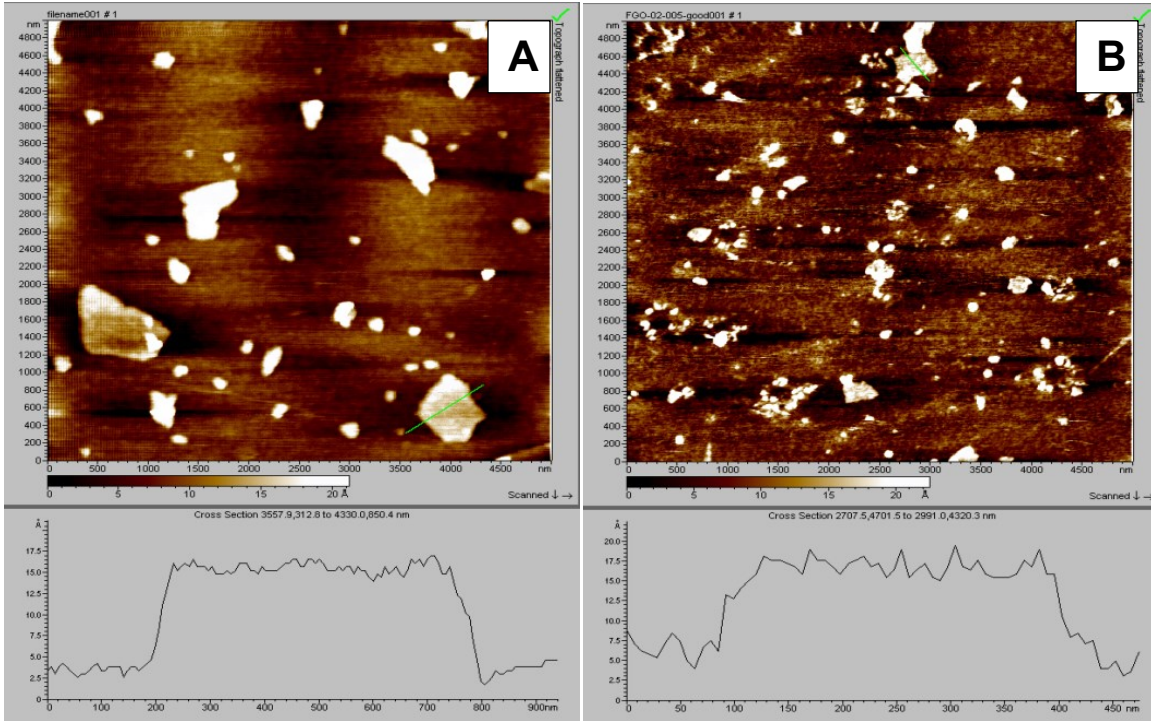
Figure 5.4 AFM images of (A) graphene oxide (GO), (B) fluorinated graphene oxide (FGO).

FGO's TEM confirmed the transparent flexible sheet structure, and the sheets contained intrinsic folds or wrinkles which are clearly observed in Figure 5.5(A). These wrinkles were due to the presence of oxygen and fluorine functional groups [25]. The sheet edges were not well defined in HRTEM (Figure 5.5(B)). The selected area electron diffraction (SAED) pattern (inset of Figure 5.5(A)) confirmed the hexagonal arrangement of the carbon atoms. The SAED pattern of the FGO exhibited a weak hexagonal structure that was indicative of severe exfoliation and sp^3 structure [26].
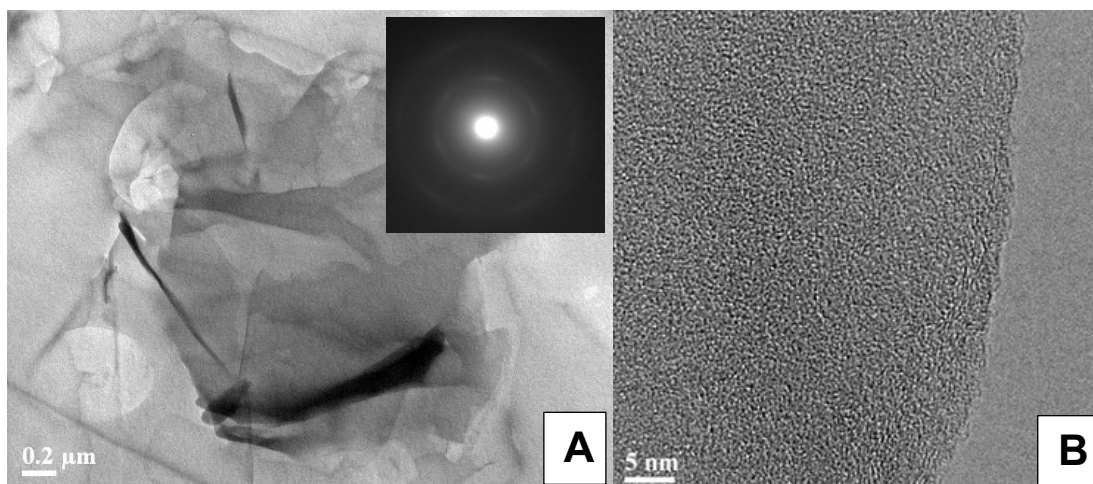
Figure 5.5 (A) and (B) HRTEM images of FGO. Inset of (A) is SAED pattern of FGO

5.3.4 X-ray photoelectron spectroscopy

XPS was employed to elucidate the composition of the FGO, particularly as it relates to the functional groups and the extent of doping. The type of bonding between the fluorine and carbon was also gleaned from XPS as ionic, semi-ionic, or covalent. Based on previous studies, fluorine doping may be measured from high resolution C1s and F1s spectra. In the C1s spectra, semi-ionic C-F bonding appeared at 287-290 eV, and in the F1s spectra at 685-688 eV [8]. Figure 5.6(A) shows the XPS survey spectra of FGO and GO. From the spectrum, the atomic composition of GO was C-64.21at.% and O-34.32 at.%, which were consistent with previous reports. The FGO contained C-63.95 at.%, O-33.00 at.%, and F-1.14 at.%; the existence of fluorine was confirmed by a peak at ~686.37 eV. The oxygen content was lower in the FGO, which was equivalent to the fluorine content. Thus, through this method, a low fluorine content graphene oxide was obtained.
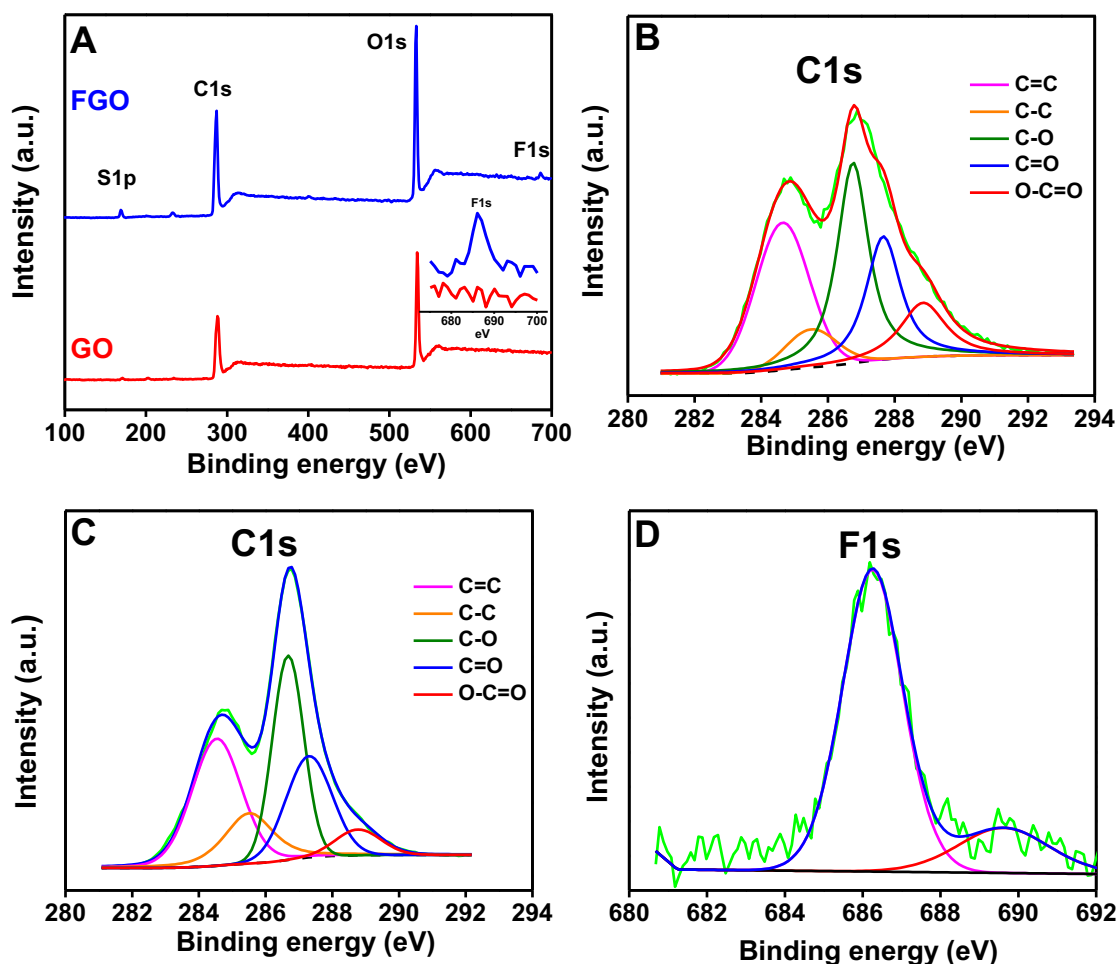
Figure 5.6 X-ray photoelectron spectra (XPS) of (A) Comparison of GO and FGO survey spectra, (B) C1s spectra of GO, (C) C1s spectra of FGO, (D) F1s spectra of FGO.

Figures 5.6(B) and (C) depict the high resolution C1s spectra of GO and FGO. In the high binding energy region, the FGO spectra appears as asymmetric, whereas this is not noticeable for the GO; hence, this feature indicated fluorination [23]. The high resolution C1s spectra was fitted by taking 284.5 eV, 285.5 eV, 286.7 eV, 287.6 eV, and 288.7 eV corresponding to C=C, C-C, C-O, C=O, and O-C=C [21]. The C=O and O-C=O content was diminished in FGO, while the C-O content increased. The semi-ionic nature of the C-F (286.8eV) bond was merged with the C-O (286.6) bond, as its binding energy was very similar [25].

Two different categories of C-F bonding are semi-ionic (with sp^3) and covalent (with sp^2) [25]. In Figure 5.6(D) the F1s spectra has two peaks, where one is a significant peak at 686.25eV, and the other is a small peak at 689.62 eV. The former corresponds to a semi-ionic bond, whereas the latter is covalent.

5.3.5 *Fourier transform infrared spectroscopy*

Figure 5.7(A) shows the FTIR spectra of GO and FGO. According to literature semi-ionic fluorine has IR absorption of 1080-1150 cm^{-1}. On the other hand, covalent C-F had an IR absorption of ~1210 cm^{-1} [27]. In our FGO, the C-F bond was semi-ionic, which was confirmed by the peak at 1083 cm^{-1}, which caused the broadening of the C-O peak. The C-F semi-ionic peak was not fully resolved due to relatively low F compared to the C-O functional group. Figure 5.7(B) is focused on the 2000-600 cm^{-1} wave numbers to visualize the difference..
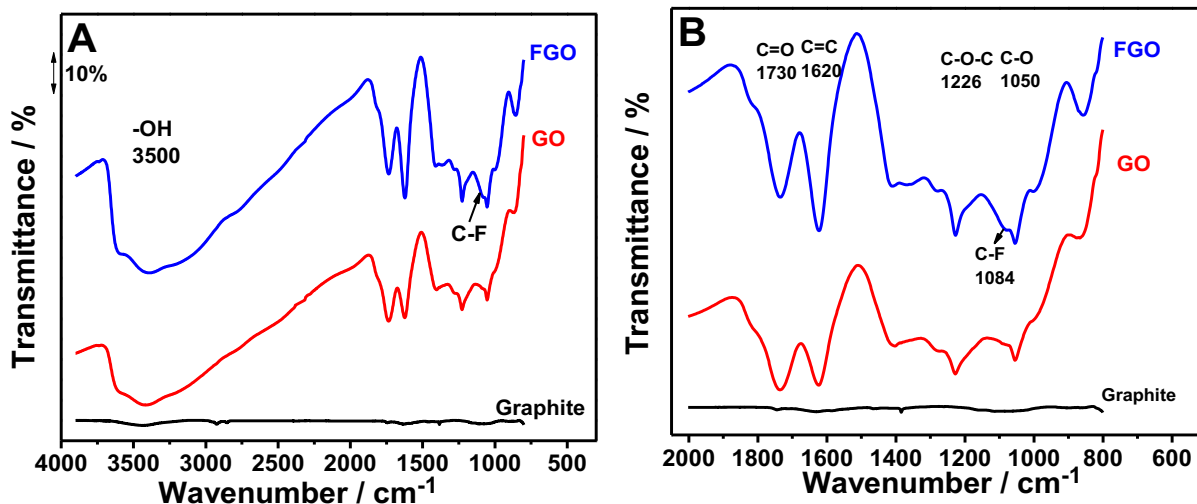
Figure 5.7 (A) Fourier transform infra-red spectra of graphite, graphene oxide, and fluorinated graphene oxide. (B) Magnified range 2000-600 cm^{-1}.

The FTIR spectra had characteristic peaks for various functional groups, such as carboxylic acids (-OH) 3500 cm-1, alcoxy(C-O) 1060 cm-1, carbonyl (C=O) 1730 cm^{-1}, sp^2 carbon (C=C) 1620

cm^{-1}, epoxide (C-O-C) 1228 cm^{-1}, in both the GO and FGO [23,25]. The FGO spectra contained

less intense C=O, which was consistent with XPS. The intensity of the C-O bond was relatively

higher in FGO, which was also in agreement with the XPS results.

5.3.6 Raman spectroscopy

The Raman spectra of the FGO and GO were recorded to understand the changes that

occurred following fluorination, and are shown in Figure 5.8. Raman spectrum of FGO looks

same as GO infers that fluorine content is less. The I_d/I_g ratio of FGO (0.84) was higher

compared to GO (0.82), which showed that fluorination caused more defects. In addition, the D'

peak appeared in FGO, but was not present in GO and also confirming fluorination. In FGO

(1595 cm^{-1}) the G band was at a higher wave number compared to GO (1586 cm^{-1}), which

indicated that it possessed fewer layers than the GO [28]. Fluorination increased the I_d/I_g ratio as

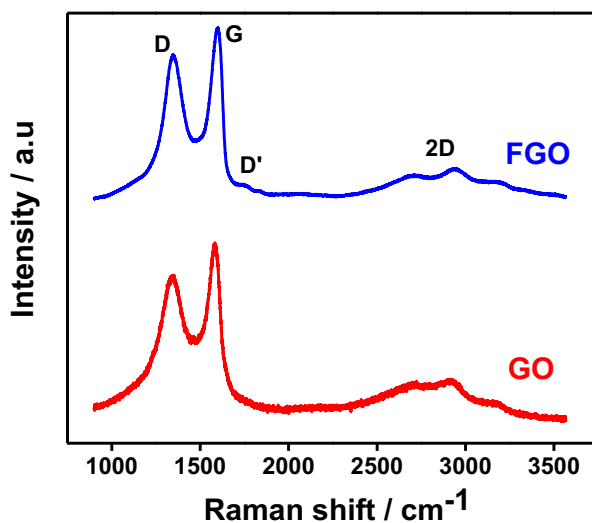well as broadened the G band. In addition, the appearance of a D' peak was significant in FGO

Figure 5.8 Raman spectra of FGO and GO.

rather than GO. Existance of D' band in FGO confirmed by averaging three sets of data recorded at different spots. The broadening of the G band occurred with a high degree of structural disorder [8].

5.4 Electrochemical characterization

5.4.1 *Full range cyclic voltammetry*

The electrochemical activity of as-prepared graphene oxide was elucidated by conducting full range cyclic voltammetry (CV) in 0.1M PBS at 7.4 pH, according to reported literature [29,30]. The 1st cycle of the full range CV for FGO and GO is shown in Figure 5.10(A). The initial potential for the scan was 0 V as there was no redox activity anticipated at this potential. From this potential, it was scanned in the negative direction, where the initial reduction of GO and FGO was observed. Three cycles were performed in the -2.0 V to 1.8 V range. This potential range was selected based on the available literature in this regard [29]. The onset potential of FGO reduction was ~0.85 V, whereas for GO, the reduction began at ~1.00 V. The peak current of reduction was achieved at 1.71 V and 1.90 V for GO and FGO, respectively. This difference indicated that the proportions of functional groups were different. The peak shapes were also broad in FGO compared to GO, which might have been due to the higher passivation in FGO. This might be related to the extent of functionalization in the case of FGO. With a higher proportion of functional groups, the surface resistivity was high which initiated slower electron transfer. The FGO did not reveal any new pattern which confirmed that the types of functional groups were similar.
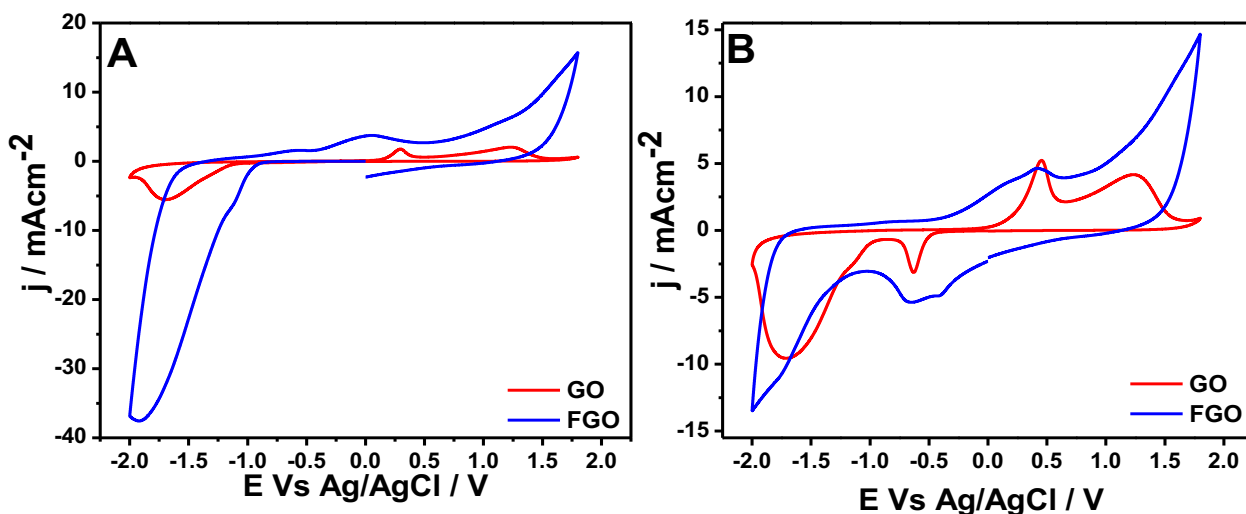
Figure 5.9 (A) Full range cyclic voltammogram of GO and FGO; (B) 2nd cycle of full range cyclic voltammogram of GO and FGO recorded in 0.1M PBS with pH 7.4 at 50 mV/s.

The 2nd cycle of the full range CV of GO and FGO is shown in Figure 5.10(B). In the 2nd cycle reduction, the current was the same or higher for GO, which was reduced slightly in the 3rd cycle. In the case of FGO, the reduction current was lower than the first cycle and remained same in the 3rd cycle. The change between the initial and remaining cycles in FGO was due to irreversible reduction of specific functional groups. In GO, the functional groups underwent reversible reduction; hence, the current was maintained in the 2nd cycle and reduced in the 3rd cycle. This was consistent with observations that were reported earlier. In the case of FGO, a significant decrease in the reduction current was observed between the 1st and 2nd reduction cycle. This may have been attributed to the presence of an irreversible functional group.

5.4.2   Electrochemical capacitor studies

Capacitance studies for GO and FGO were conducted in the -0.2V to 1.0V range using CV. The capacitance of GO and FGO was the same prior to their being subjected to the full range CV Figure 5.11(A). The capacitance values were very small due to the presence of oxygen functional

groups which caused high resistance, and minute differences may be seen, as FGO is smaller than GO. This may be the result of a large quantity of functional groups that were present in the FGO. During the full range CV, the surface functional groups present in GO and FGO were reduced and thus following the full range CV, they were denoted as rGO and rFGO, respectively. Following three cycles of the full range CV, the capacitance of rGO and rFGO were compared by performing a cyclic voltammogram in 0.5M H_2SO_4 at -0.2 to 1.0 V (Figure 5.11(B)). The capacitance after the full range CV was 50 times higher than the GO in rGO, whereas it was 100 times higher than the FGO in rFGO.
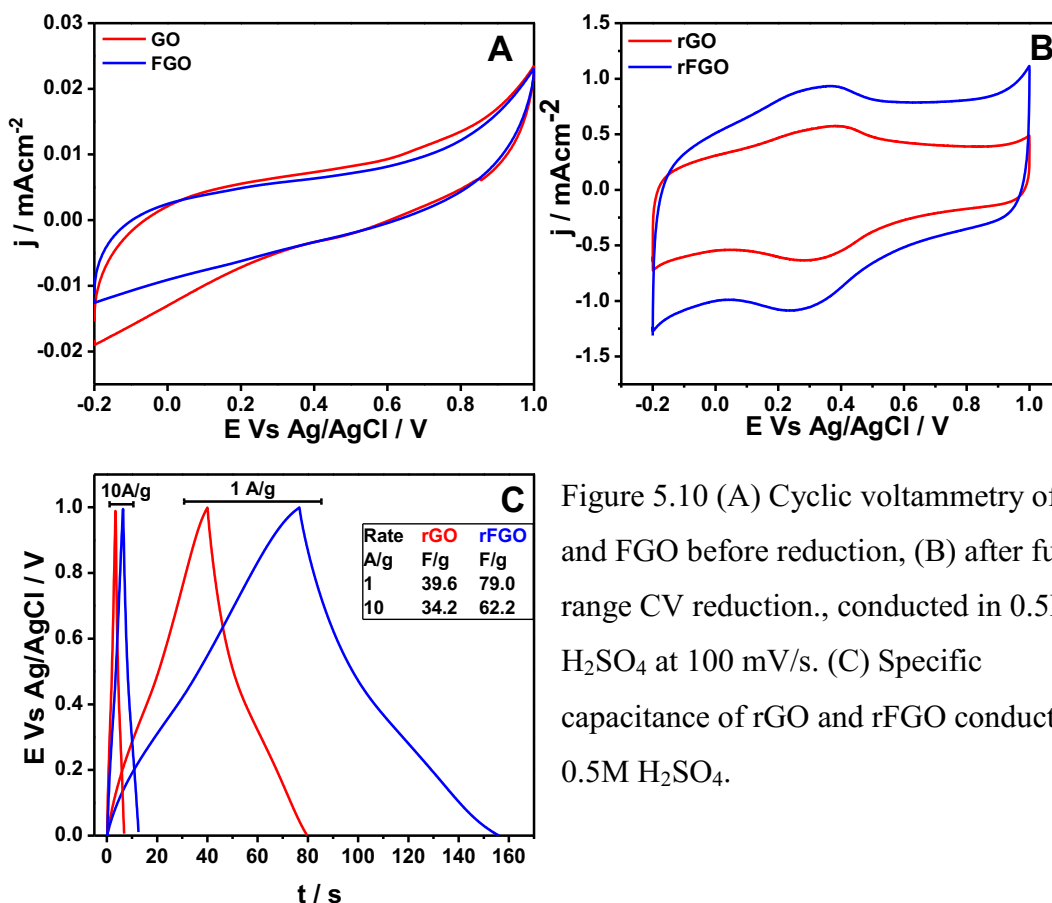

Figure 5.10 (A) Cyclic voltammetry of GO and FGO before reduction, (B) after full range CV reduction., conducted in 0.5M H_2SO_4 at 100 mV/s. (C) Specific capacitance of rGO and rFGO conducted in 0.5M H_2SO_4.

The rFGO has a higher capacitance than rGO, which may be inferred from the larger area of cyclic voltammogram [15]. The specific capacitance of the FGO and GO was compared by

galvanostatic cycling at a 1A/g rate in Figure 5.11(C). The FGO possessed 79.00 F/g, whereas the GO had 39.64 F/g. Further, the specific capacitance of FGO was consistent in the high rate discharge. At 10 A/g, the discharge rate of the capacitance of FGO was 62.2 F/g, and GO showed 34.2 F/g in Figure 5.11(C). The reasoning for this increased capacitance may be understood from the full range CV response. For the FGO, the full range CV irreversible reduction occurred in first cycle of reduction, which may initiate high capacitance. Furthermore, the intensity of functional groups and defects were high in FGO compared to GO, and can be understood from the XPS, FTIR, and Raman characterization results. Thus FGO may be a better co-material in the preparation of nanocomposites for supercapacitor applications.

5.5   Heavy metal ion sensing

Simultaneous heavy metal ion sensing was investigated via a systematic method for GO and FGO. The heavy metal ions selected for this study were Cd, Pb, Cu, and Hg. Prior to the sensing experiments the GO and FGO electrodes were pretreated to improve their conductivity. This pretreatment involved the partial reduction of GO and FGO. This pretreatment was achieved by applying -1.2 V for 300 s, and was applied to both the GO and FGO for identical comparison. During the pretreatment, the electrode surface was partially reduced, which altered the composition of the functional groups in order to obtain improved sensitivity toward metal ion sensing.

The heavy metal ion sensing ability was compared for the glassy carbon electrode, GO, and FGO in Figure 5.12 where equal quantity (2 µM) of each metal ion was used to compare the sensing activities of the different materials. The glassy carbon electrode did not show the stripping current for Cd and Pb, whereas Cu and Hg were detected. Even though SWASV was employed, the GO showed large background current, and no peaks were observed. GO is

reported as an adsorbent to remove heavy metal ions [31]. Thus it is understood that the stripping is not facile in GO, due to the strong bonding of metal ions to the GO surface. The broader stripping voltammogram of GO may be due to heavy metal ions accumulated are diffusing out slowly. In contrast, the FGO showed a significant current for all four heavy metals and the peaks were distinguishable. The corresponding peak potentials of Cd, Pb, Cu, and Hg were -0.73, -0.52, -0.03, and +0.33V, respectively. FGO possesses a smaller sheet size compared to GO, which imparts a higher surface area to FGO; on the other hand it enhances the metal ion absorption [4]. Although the metal ion adsorption was similar in both the GO and FGO, due to its higher affinity, GO did not allow for stripping, whereas in FGO, the presence of F facilitated the process. Once the metal ion stripping activity was confirmed, the optimization of experimental parameters was carried out to gauge the sensitivity of the material.
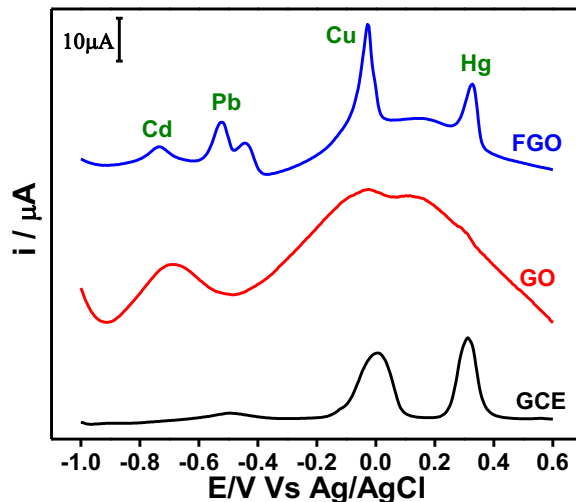
Figure 5.11 Square wave anodic stripping voltammetry (SWASV) response comparison for 2μM of Cd(II), Pb(II), Cu(II) and Hg(II), GCE, GO, FGO, recorded in 0.1M acetate buffer with pH 5.0.

5.5.1 Optimization of parameters

The optimization of sensing parameters was done for sensing 2 μM of each heavy metal ion in simultaneous sensing mode. The current response for each metal ion stripped from SWASV was compared. The optimization of parameters proceeded in the following order: preconditioning potential and duration, deposition potential and duration. The effect of each parameter is shown in Figures 5.13(A) – (D).
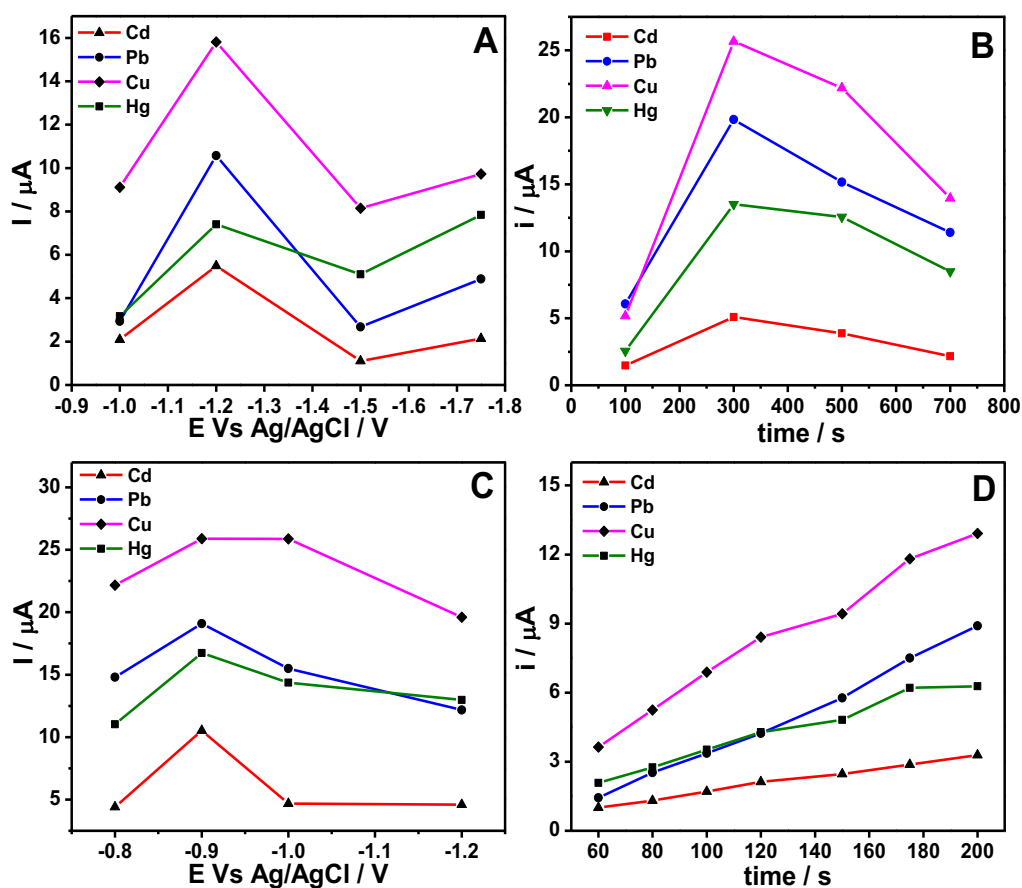
Figure 5.12 Optimization of parameters, (A) Pretreatment potential (B) Pretreatment duration, (C) Deposition potential and (D) Deposition time. Note: Current response recorded for 2 μM analyte and simultaneous sensing, carried out in 0.1M acetate buffer with pH 5.0.

According to available previous literature in this context, pH is a sensitive parameter, which can be optimized to 4-5 pH, and an acetate buffer may be used for improved sensitivity [4,32]. Firstly, the preconditioning potential was optimized at -1.2 V (Figure 5.13(A)). The sensitivity was decreased at positive potentials due to less conductivity, where adequate functional groups were not reduced in that potential. On the other hand, at more negative potentials, aggressive reduction caused loss of activity. During reduction it may cause the reduction of specific functional groups, which catalyze the metal ion stripping. Using this information, the preconditioning duration was optimized for better sensitivity. A higher current response was shown to be the result of 300 seconds of preconditioning, rather than a lower or higher duration (Figure 5.13(B)). This may also be explained in the same way as for the preconditioning potential. Further experiments were carried out with the optimized pretreatment potential and duration.

The deposition potential and duration directly affected the sensitivity and detection limit of the materials. The effect of the deposition potential in the range of from -0.8 V to -1.2 V was studied (Figure 5.13(C)). When the potential increased in the negative direction, the current response was increased. Following -0.9 V, the current response decreased while increasing the deposition potential in the negative direction. The onset of the reduction of GO and FGO occurred from -0.8 V to -1.0 V. Although the surface was partially reduced during the pretreatment, functional groups were still active on the surface. During the pretreatment, functional groups reducible at -0.8 to -1.2 V were considerably reduced. Hence, when the potential increased in the negative direction, the reduction of GO or FGO competed with the deposition of metal ions. The reduction process was more aggressive, thus, the metal ion absorption occurred under -1.0 V. Hence, -0.9 V was selected as the deposition potential for

further experiments. The next parameter was deposition duration, which may be directly related to the concentration of metal ions that are deposited on the electrode surface. As the deposition duration was increased, from 60 s to 200 s, the current response was increased and it was linear (Figure 5.13(D)), thus, longer deposition times will improve sensitivity. Longer deposition times increased the surface concentration of the analyte; surface saturation of the analyte diminish the upper detection limit [16]. Therefore, the deposition duration was optimized at 175 seconds for the remaining studies.

5.5.2   *Simultaneous sensing*

The simultaneous sensing of the four metal ions was investigated further with the optimized parameters. The SWASV and calibration plots are shown in Figures 5.14(A) and (B). All four metals were stripped with appropriate potential intervals, thus FGO was capable of simultaneous sensing. The stripping current increased proportionately with the concentration of metal ions that were present in the solution. The linear range of the FGO sensing ability was from 1.0 μM to 6.0 μM, as shown in Figure 5.7(A). Well distinguished peaks were observable for all metal ions when 1 μM of metal ion was present in the solution. This might have been due to the sensitivity variations between the metal ions. The correlation factors (R^2) obtained from the calibration plots obtained were 0.9881, 0.9951, 0.9879, and 0.9922 for Cd, Pb, Cu, and Hg, respectively (Figure 5.14(B)). This assured the linearity of the current increment with respect to the addition of the metal ions. The sensitivity of each metal ion was known from the slope of calibration curves, namely, 3.64, 6.05, 3.64, and 4.24 μA/μM for Cd, Pb, Cu, and Hg, respectively. The lowest detection limit (LOD) was determined using a 3σ method, by calculating the standard deviation (σ) of the baseline current and using the slope (*S*) of the calibration plot. The equation (1) used for LOD calculation.

$$LOD = \frac{3\sigma}{S} \quad \text{----------(1)}$$
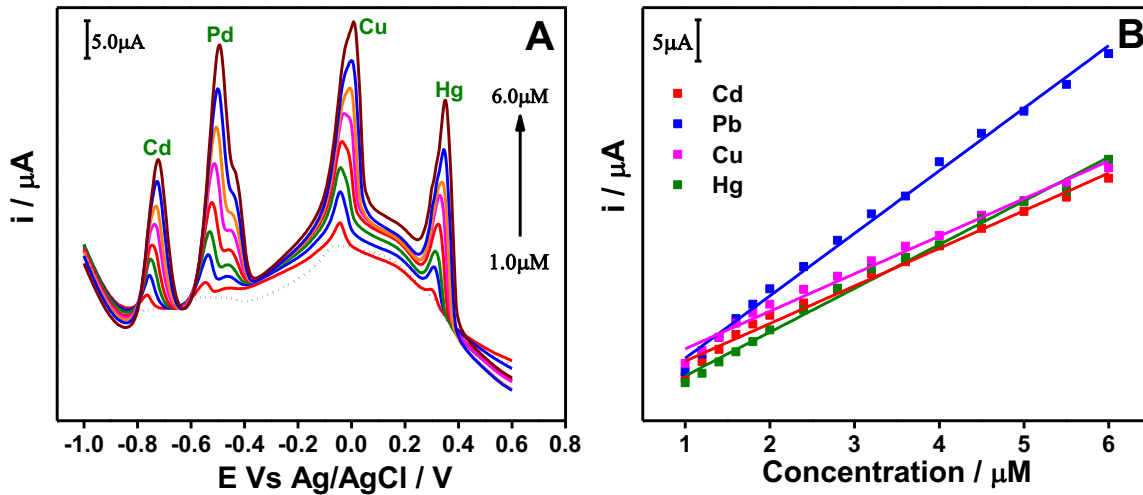
Figure 5.13 Concentration effect on the simultaneous sensing of Cd^{2+}, Pb^{2+}, Cu^{2+}, and Hg^{2+} ions, (B) SWASV response and (C) Calibration plot. Corresponding R^2 values in calibration plots for Cd-0.9881, Pb-0.9951, Cu-0.9879, Hg-0.9922., SWASVs recorded in 0.1M acetate buffer with pH 5.0.

The LOD obtained for Cd = 90 nM, Pb = 20 nM, Cu = 220 nM, and Hg=60 nM. The LOD for Cu was higher compared to the other metal ions, and was due to Hg complex formation. This resulted in an irregular stripping response for Cu. Wei et.al discussed that for a SnO_2/rGO composite, the peak shape of the Hg metal ion stripping was affected, and was likely due to the Cu-Hg complex formation [16]. This reasoning may be applicable here for the mismatched LOD for Cu, and further, the Pb stripping showed double peak. This might also be due to the complexing mechanism. The LOD and sensitivity of the present rFGO was comparable with previously reported metal/metal oxide nanocomposites [1]. The mutual presence of four metal ions might affect each other's detection limit and sensitivity; hence, in order to better understand this, individual sensing was carried out with optimized parameters for all four metal ions.

5.5.3 Individual sensing

Individual metal ion sensing was studied to understand the effects of mutual interference. The sensing activity and calibration curves of the individual metal ions Cd(II), Pb(II), Cu(II), and Hg(II) are shown along with respective calibration curves in Figure 5.15(A) – (D).
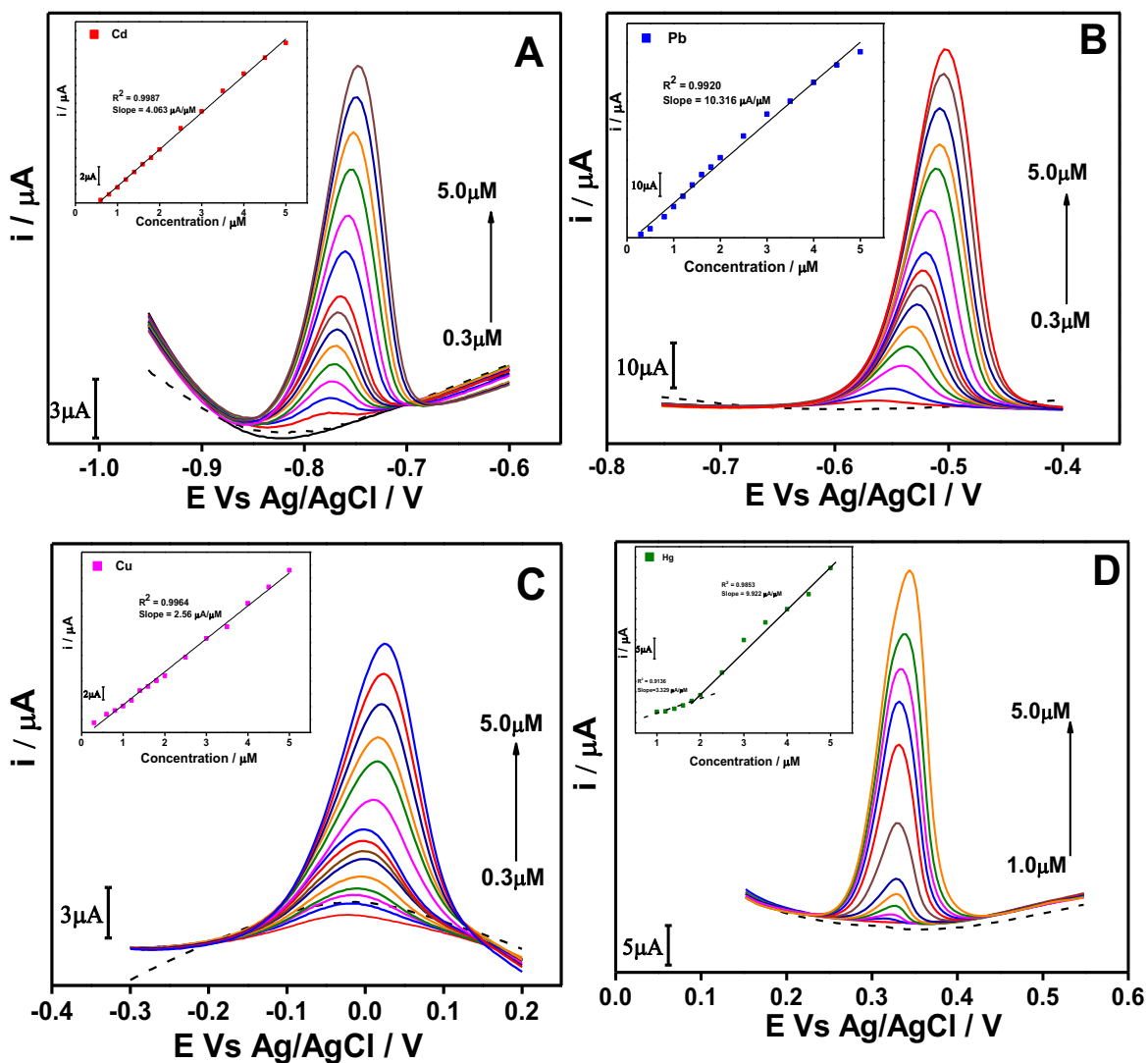
Figure 5.14 Concentration effect of individual ion sensing along with calibration plot in the inset; (A) Cd, (B) Pb, (C) Cu, (D) Hg; corresponding R^2 values Cd=0.9987, Pb=0.9920, Cu=0.9964, Hg=0.9821., conducted in 0.1M acetate buffer with pH 5.0.

The Cd sensing activity is depicted in Figure 5.15(A). The sensitivity of Cd read from the slope in the inset was 4.06 μA/μM, with a corresponding R^2 value of 0.9987, and calculated LOD was 10 nM. The Pb sensitivity was 10.32 μA/μM, with R^2 of 0.9920, and LOD of 10 nM (Figure 5.15(B)). The Cu sensitivity was 2.56 μA/μM and corresponding R^2 was 0.9964, with the LOD computed as 120 nM (Figure 5.15(C)). The Hg showed a different pattern, where the current response increment was in two steps; 1.0 to 2.0 μM was the first range, with a sensitivity of 3.36 μA/μM, and the next step was from 2 to 5 μM, with a sensitivity of 9.92 μA/μM (Figure 5.15(D)). According to literature, the lowest sensitivity is used to determine the LOD, which is 20 nM [33]. In individual sensing the LOD was lower than for the simultaneous sensing. The Cd, Pb, and Cu showed well-defined peaks below 1.0 μM. This indicated that there was an influence when all of the metal ions were simultaneously present in solution.

5.6 Summary

Fluorinated graphene oxide was synthesized using a facile one pot synthesis method using ZEN915 graphite. Its morphology, structure, composition were investigated, and FGO exhibited distinct characteristics in contrast to GO. The FGO exhibited different compositions of functional groups and at higher quantities than GO. It also revealed a relatively higher capacitance than GO. The presence of fluorine was confirmed by EDS, XPS, and Raman spectra analysis. The fluorine content was estimated as ~1.0 at. %. Heavy metal ion stripping was demonstrated on FGO, which was not evident on the GO surface. Furthermore, this work promoted the further scope of fluorine doped graphene oxide derivatives. FGO may be explored for additional applications.

References

[1]   P. Gnanaprakasam, S.E. Jeena, D. Premnath, T. Selvaraju, Simple and Robust Green Synthesis of Au NPs on Reduced Graphene Oxide for the Simultaneous Detection of Toxic Heavy Metal Ions and Bioremediation Using Bacterium as the Scavenger, *Electroanalysis* 28 (**2016**) 1885–1893.

[2]   Y.L. Xie, S.Q. Zhao, H.L. Ye, J. Yuan, P. Song, S.Q. Hu, Graphene/CeO2 hybrid materials for the simultaneous electrochemical detection of cadmium(II), lead(II), copper(II), and mercury(II), *Journal of Electroanalytical Chemistry* 757 (**2015**) 235–242.

[3]   N. Promphet, P. Rattanarat, R. Rangkupan, O. Chailapakul, N. Rodthongkum, An electrochemical sensor based on graphene/polyaniline/polystyrene nanoporous fibers modified electrode for simultaneous determination of lead and cadmium, *Sensors and Actuators, B: Chemical* 207 (**2015**) 526–534.

[4]   H. Xing, J. Xu, X. Zhu, X. Duan, L. Lu, W. Wang, Y. Zhang, T. Yang, Highly sensitive simultaneous determination of cadmium (II), lead (II), copper (II), and mercury (II) ions on N-doped graphene modified electrode, *Journal of Electroanalytical Chemistry* 760 (**2016**) 52–58.

[5]   R. Gusmão, Z. Sofer, F. Šembera, Z. Janoušek, M. Pumera, Electrochemical Fluorographane: Hybrid Electrocatalysis of Biomarkers, Hydrogen Evolution, and Oxygen Reduction, *Chemistry - A European Journal* 21 (**2015**) 16474–16478.

[6]   K.J. Jeon, Z. Lee, E. Pollak, L. Moreschini, A. Bostwick, C.M. Park, R. Mendelsberg, V. Radmilovic, R. Kostecki, T.J. Richardson, E. Rotenberg, Fluorographene: A wide bandgap semiconductor with ultraviolet luminescence, *ACS Nano* 5 (**2011**) 1042–1046.

[7]   L. Cheng, S. Jandhyala, G. Mordi, A.T. Lucero, J. Huang, A. Azcatl, R. Addou, R.M. Wallace, L. Colombo, J. Kim, Partially Fluorinated Graphene: Structural and Electrical Characterization, *ACS Applied Materials & Interfaces* 8 (**2016**) 5002–5008.

[8]   W. Feng, P. Long, Y. Feng, Y. Li, Two-Dimensional Fluorinated Graphene: Synthesis, Structures, Properties and Applications, *Advanced Science* 3 (**2016**) 1500413.

[9]   A. Mathkar, T.N. Narayanan, L.B. Alemany, P. Cox, P. Nguyen, G. Gao, P. Chang, R. Romero-Aburto, S.A. Mani, P.M. Ajayan, Synthesis of fluorinated graphene oxide and its amphiphobic properties, *Particle and Particle Systems Characterization* 30 (**2013**) 266–272.

[10]   X. Wang, Y. Dai, J. Gao, J. Huang, B. Li, C. Fan, J. Yang, X. Liu, High-yield production of highly fluorinated graphene by direct heating fluorination of graphene-oxide, *ACS Applied Materials and Interfaces* 5 (**2013**) 8294–8299.

[11]   X. Sun, Y. Zhang, P. Song, J. Pan, L. Zhuang, W. Xu, W. Xing, Fluorine-doped carbon blacks: Highly efficient metal-free electrocatalysts for oxygen reduction reaction, *ACS Catalysis* 3 (**2013**) 1726–1729.

[12] A. Vizintin, M. Lozinšek, R.K. Chellappan, D. Foix, A. Krajnc, G. Mali, G. Drazic, B. Genorio, R. Dedryvère, R. Dominko, Fluorinated Reduced Graphene Oxide as an Interlayer in Li–S Batteries, *Chemistry of Materials* 27 (**2015**) 7070–7081.

[13] D. Damien, P.M. Sudeep, T.N. Narayanan, M.R. Anantharaman, P.M. Ajayan, M.M. Shaijumon, Fluorinated graphene based electrodes for high performance primary lithium batteries, *RSC Advances* 3 (**2013**) 25702.

[14] R. Romero-Aburto, T.N. Narayanan, Y. Nagaoka, T. Hasumura, T.M. Mitcham, T. Fukuda, P.J. Cox, R.R. Bouchard, T. Maekawa, D.S. Kumar, S. V. Torti, S.A. Mani, P.M. Ajayan, Fluorinated graphene oxide; A new multimodal material for biological applications, *Advanced Materials* 25 (**2013**) 5632–5637.

[15] F.-G. Zhao, G. Zhao, X.-H. Liu, C.-W. Ge, J.-T. Wang, B.-L. Li, Q.-G. Wang, W.-S. Li, Q.-Y. Chen, Fluorinated graphene: facile solution preparation and tailorable properties by fluorine-content tuning, *Journal of Materials Chemistry A* 2 (**2014**) 8782.

[16] Y. Wei, C. Gao, F.-L. Meng, H.-H. Li, L. Wang, J.-H. Liu, X.-J. Huang, SnO 2 /Reduced Graphene Oxide Nanocomposite for the Simultaneous Electrochemical Detection of Cadmium(II), Lead(II), Copper(II), and Mercury(II): An Interesting Favorable Mutual Interference, *The Journal of Physical Chemistry C* 116 (**2012**) 1034–1041.

[17] S. Muralikrishna, K. Sureshkumar, T.S. Varley, D.H. Nagaraju, T. Ramakrishnappa, In situ reduction and functionalization of graphene oxide with l-cysteine for simultaneous electrochemical determination of cadmium(II), lead(II), copper(II), and mercury(II) ions, *Analytical Methods* 6 (**2014**) 8698–8705.

[18] P.J. Mafa, A.O. Idris, N. Mabuba, O.A. Arotiba, Electrochemical co-detection of As(III), Hg(II) and Pb(II) on a bismuth modified exfoliated graphite electrode, *Talanta* 153 (**2016**) 99–106.

[19] C.M. Willemse, K. Tlhomelang, N. Jahed, P.G. Baker, E.I. Iwuoha, Metallo-Graphene nanocomposite electrocatalytic platform for the determination of toxic metal ions, *Sensors* 11 (**2011**) 3970–3987.

[20] D.C. Marcano, D. V. Kosynkin, J.M. Berlin, A. Sinitskii, Z. Sun, A. Slesarev, L.B. Alemany, W. Lu, J.M. Tour, Improved Synthesis of Graphene Oxide, *ACS Nano* 4 (**2010**) 4806–4814.

[21] V. Mazánek, O. Jankovský, J. Luxa, D. Sedmidubský, Z. Janoušek, F. Šembera, M. Mikulics, Z. Sofer, Tuning of fluorine content in graphene: towards large-scale production of stoichiometric fluorographene, *Nanoscale* 7 (**2015**) 13646–13655.

[22] J.T. Robinson, J.S. Burgess, C.E. Junkermeier, S.C. Badescu, T.L. Reinecke, F.K. Perkins, M.K. Zalalutdniov, J.W. Baldwin, J.C. Culbertson, P.E. Sheehan, E.S. Snow, Properties of fluorinated graphene films, *Nano Letters* 10 (**2010**) 3001–3005.

[23] O. Jankovský, P. Šimek, D. Sedmidubský, S. Matějková, Z. Janoušek, F. Šembera, M.

Pumera, Z. Sofer, Water-soluble highly fluorinated graphite oxide, *RSC Advances* 4 (**2014**) 1378.

[24] F.-X. Ma, J. Wang, F.-B. Wang, X.-H. Xia, The room temperature electrochemical synthesis of N-doped graphene and its electrocatalytic activity for oxygen reduction, *Chemical Communications* 51 (**2015**) 1198–1201.

[25] X. Yang, X. Jia, X. Ji, Acid induced fluorinated graphene oxide, *RSC Advances* 5 (**2015**) 9337–9340.

[26] Y. Yang, G. Lu, Y. Li, Z. Liu, X. Huang, One-step preparation of fluorographene: A highly efficient, low-cost, and large-scale approach of exfoliating fluorographite, *ACS Applied Materials and Interfaces* 5 (**2013**) 13478–13483.

[27] X. Wang, W. Wang, Y. Liu, M. Ren, H. Xiao, X. Liu, Characterization of Conformation and Locations of C-F Bonds in Graphene Derivative by Polarized ATR-FTIR, *Analytical Chemistry* 88 (**2016**) 3926–3934.

[28] M. Yi, Z. Shen, S. Ma, X. Zhang, A mixed-solvent strategy for facile and green preparation of graphene by liquid-phase exfoliation of graphite, *Journal of Nanoparticle Research* 14 (**2012**) 1003.

[29] A.Y.S. Eng, A. Ambrosi, C.K. Chua, F. Šaněk, Z. Sofer, M. Pumera, Unusual Inherent Electrochemistry of Graphene Oxides Prepared Using Permanganate Oxidants, *Chemistry - A European Journal* 19 (**2013**) 12673–12683.

[30] J.G.S. Moo, A. Ambrosi, A. Bonanni, M. Pumera, Inherent electrochemistry and activation of chemically modified graphenes for electrochemical applications, *Chemistry - An Asian Journal* 7 (**2012**) 759–770.

[31] J.G.S. Moo, B. Khezri, R.D. Webster, M. Pumera, Graphene Oxides Prepared by Hummers', Hofmann's, and Staudenmaier's Methods: Dramatic Influences on Heavy-Metal-Ion Adsorption, *ChemPhysChem* 15 (**2014**) 2922–2929.

[32] Y.-F. Sun, L.-J. Zhao, T.-J. Jiang, S.-S. Li, M. Yang, X.-J. Huang, Sensitive and selective electrochemical detection of heavy metal ions using amino-functionalized carbon microspheres, *Journal of Electroanalytical Chemistry* 760 (**2016**) 143–150.

[33] Z. Liu, H. Forsyth, N. Khaper, A. Chen, Sensitive electrochemical detection of nitric oxide based on AuPt and reduced graphene oxide nanocomposites, *The Analyst* 141 (**2016**) 4074–4083.

Chapter VI

Summary and Future outlook

6.1 Concluding remarks

Natural graphite is a primary source for the preparation of graphene based materials. Graphene based nanomaterials is a very popular topic which has generated a copious quantity of literature over the last decade. The properties of graphite have an impact in the quality of prepared graphene based materials. For this thesis, different graphite samples and their corresponding graphene oxide properties were investigated. The results substantiated that crystallite size, defect density, and oxygen content of graphite have a noteworthy influence on the quality of graphene oxide. Based on the analysis, the best graphite was selected for the preparation of fluorine doped graphene oxide. In addition, two applications were identified for FGO, namely, electrochemical capacitors and heavy metal ion detection.

6.2 Graphite characterization and properties

For this project, four different graphite samples were characterized and their properties were estimated. All of the graphite samples had a layered morphology, and it was observed that the ZEN 378 samples had a smaller particle size, in contrast to the other samples. The ZEN 378 had a high surface area, which was consistent with the SEM observations. The thermal stability of graphite samples was investigated in ambient atmosphere, and no significant difference was observed. The XRD observation revealed details related to crystallinity, interlayer spacing, average crystallite size, and number of layers. The SA 325 sample possessed more layers of stacked graphite and a larger crystallite size compared to the other samples. The XPS then provided a clearer understanding of the composition of the graphite samples. It was discovered that all of graphite samples had some degree of surface oxygen content, with the ZEN 915 samples having a higher oxygen % compared to the other samples. The SA 325 graphite sample

had a high carbon content, which was confirmed via EDS and XPS analysis. Raman spectroscopy provided data on defect densities, where the AA 325 and ZEN 915 samples had a higher defect density in contrast to the other samples. Furthermore, the electrochemical properties of the graphite samples were studied to elucidate the specific capacitance and potential window. The SA 325 graphite sample exhibited a lower capacitance and a wider potential window. This observation complemented previous results, such as high carbon content, large crystallite size, low surface area, and fewer defects. This analysis provided useful data to facilitate the comparison of the physiochemical and electrochemical properties of the graphite samples.

6.3 Graphene oxide synthesis and characterization

Graphene oxide was synthesized using an improved Hummer's method from four different graphite samples. The properties of graphene oxide were studied and the results are related to the graphite characteristics. The morphology of all four GOs appeared alike, with wrinkled layered structures. The XRD pattern confirmed the complete oxidation of graphite and showed a wider interlayer spacing for the ZEN 915-GO sample. The functional groups present in the GO samples were confirmed from FTIR spectra; similar types of functional groups were observed in all four samples. The Raman spectra of the GO samples showed an enhanced D band, affirming the oxidation and enhanced proportion of the sp^3 hybridized carbon atoms. The electrochemistry of the GO samples was investigated in order to understand specific capacitance, to evaluate the electron transfer properties, and to observe the reduction pattern. All GO samples were subjected to electrochemical reduction and their electrochemical performance was examined. The trend of capacitance was the same as that observed for the graphite samples (i.e., AA 325-GO = ZEN 915-GO > ZEN 378-GO > SA 325-GO). The heterogeneous electron transfer ability improved

following reduction due to improved conductivity and π conjugation. The amount of the functional groups was high in the ZEN 915-GO sample, and composition of functional groups was similar across all GO samples. These analyses supported the premise that graphite properties can have substantial influence on the properties of graphene oxide.

6.4 Fluorine doped graphene oxide synthesis and electrochemical applications

Proceeding with previous results ZEN915 graphite was selected to develop a novel method for the synthesis of fluorine doped graphene oxide (FGO). The morphology, crystallography, FTIR, Raman, and UV visible absorbance characterization of the FGO were compared with GO. The FGO showed more unusual electrochemical properties than did graphene oxide. It was found that ~1at.% of fluorine doped in the graphene oxide matrix was instrumental in facilitating the sensing of ultralow concentrations of Cd(II), Pb(II), Cu(II), and Hg(II), both simultaneously and individually. In addition, FGO had an electrochemical capacitance of 79.0 F/g compared to 39.6 F/g for GO.

6.5 Future outlook

In this work, the influence of the properties of graphite on the quality of prepared graphene oxide was demonstrated. A novel method was developed to prepare fluorine functionalized graphene oxide, and its properties were examined.

Although recent methods have shown more rapid and high yielding processes toward the preparation of graphene based materials, there remains the requirement for improving the quality of graphene and reducing the toxicity of the process. Based on the understanding of the graphite properties, future studies will focus on novel methods to produce high quality graphene using green synthesis methods. Further, in-situ functionalization will be explored, along with the exfoliation of graphite through advanced physiochemical and electrochemical techniques.

To fine tune the approach developed for the synthesis of FGO, studies will explore how fluorine content might be enhanced by adjusting the HF dosage during synthesis. Graphene oxide (GO) was explored as a catalyst support for various energy conversion reactions. It was observed that FGO exhibited unusual electrochemical characteristics; hence, there is scope to investigate FGO as a catalyst support in contrast to GO. Since fluorinated carbons have demonstrated catalytic abilities, they may serve as better catalytic supports than GO.